# Carbon Nanotube Quantum Dots

*En çok sevdiğim iki kadın için:*
*Eşim ve annem.*

# Carbon nanotube quantum dots

**Proefschrift**

ter verkrijging van de graad van doctor
aan de Technische Universiteit Delft,
op gezag van de Rector Magnificus prof.dr.ir. J.T. Fokkema,
voorzitter van het College voor Promoties,
in het openbaar te verdedigen op dinsdag 20 juni 2006 om 15.00 uur

door

## Sami SAPMAZ

natuurkundig ingenieur
geboren te Dordrecht.

Dit proefschrift is goedgekeurd door de promotor:
  Prof. dr. ir. L. P. Kouwenhoven

Samenstelling van de promotiecommissie:

| | |
|---|---|
| Rector Magnificus, | voorzitter |
| Prof. dr. ir. L. P. Kouwenhoven | Technische Universiteit Delft, promotor |
| Dr. ir. H. S. J. van der Zant | Technische Universiteit Delft, toegevoegd promotor |
| Prof. dr. C. Dekker | Technische Universiteit Delft |
| Prof. dr. J. W. M. Frenken | Universiteit Leiden |
| Prof. dr. A. Yacoby | Weizmann Institute of Science, Israël |
| Prof. dr. D. Loss | University of Basel, Zwitserland |
| Dr. Ya. M. Blanter | Technische Universiteit Delft |
| Prof. dr. ir. J. E. Mooij | Technische Universiteit Delft, reservelid |

Printed in the Netherlands

# Preface

In some sense I could be classified as 'made in Delft'. Back in 1997, just a few days after Lady Diana's tragic car accident, I started in Delft. I didn't have any idea about nanoscience or about nanotubes, even though the 'Golden years' in nanotube research had just started.

Towards the end of my applied physics study I started to look around for my 'afstudeer' project. A very colorful and nice looking advertisement of the possible projects in the Quantum Transport group caught my attention. One of these projects was about nanoelectromechanics and images of the nanoguitar and the quantum bell were depicted on the advertisement. This is were I first met Herre van der Zant who was considering to start projects in this direction. From that time on Herre has been more than just a supervisor: he has been always a good support and above all a very good friend. I thank you for all your guidance and wish all the best with the new MED group.

The work in QT has definitely played a major role in my interest for quantum dots and especially nanotube quantum dots. I think this is the best place to thank my promotor, Mister quantum dot himself, Leo Kouwenhoven. Your thorough understanding of many areas in physics and your quick way in recognizing the interesting 'stuff' has always impressed me enormously. I would like to thank you for being my promotor and always showing interest in the work I did. Furthermore, I just want to say, with focussing on the nanowires and nanotubes you are on the right track. Forget about GaAs ;-) Also many thanks to all the staff members Hans, Kees, Ad, Val, and Lieven for creating a group with many possibilities and a nice atmosphere. Thanks to the technical staff (Bram, Mascha, Remco, Raymond, Arno, Leo D, Leo L, Wim and Willem) is evertyhing running. Yuki and Ria, thanks for all the management work.

Let me continue with the person I have worked most with. Pablo, throughout my Ph.D. you have been an example and inspiring person to me. *Me has ayudado mucho!* Good luck in New York. The switch from HiPCO to CVD nanotube took place after the arrival of Jing Kong. She is a very nice, intelligent and hard-working lady. The last period of my Ph.D. I have worked with the always

friendly Carola. It was a big pleasure to work with you and wish you success with your research in nanotubes filled with fullerenes. I would like to thank Piotr for the nice discussions and wish him good luck in his new career. Recently, the nanotube subgroup has grown with two new members: Georg and Gary ('uhmm interesting'). I am sure the nanotube community will here much from you guys! Good luck with the nanotube spin qubits. I would also like to mention Henk Postma and Leonid Gurevich here. You guys have taught me the basics of nanofabrication and gave me impuls at the very beginning of my QT time. I had the pleasure of supervising Samir (good luck with your Ph.D. at MED), Jan, Arjan, Edoardo, and Thomas with whom I should finish around the same time.

One of the highlights, from an entertainment point of view, was the 'skiing' conference in Mauterndorf where I went together with off-piste Hubert, Jorden, and Silvano. Hubert, I will never forget your trick on me, when I was for the first time on skies: "Sami, blauw kun je makkelijk hebben". Still I would like to thank you and Silvano for teaching me the basics of skiing. Jorden, I wish you all the best with your upcoming defense. And, Silvano, I am looking forward in doing a Postdoc with you.

One of my tasks in QT was to _lure_ students to QT. This work I did together with other 'PR'-members; from the old school these were Alexander, Jero, and Ronnie and the newer members are $F^3$ (Floris, Floor, and Franck). I have to regretfully mention that the new PR-members have successfully changed the old success formula: At least mention in a presentation Marco van Basten, that Einstein was wrong and the Nobel prize.

Here I would like to seize the oppurtunity to thank some people from the 'oude garde': Wilfred, your 'heilige schrift' was always in my close proximity, Jeroen (a very short time member of the nanotube subgroup), Ronald, Hannes, Patrice, Günther, and Adrian.

Almost during my entire Ph.D., my office was in room 'B(ond) 007'. The atmosphere was always extremely pleasant. I would like to thank therefore my office mates Yong-joo, Jonathan, Eugen, Katja and Juriaan. Eugen, after you have left the noise level in our room (and in the group as well) went really down. I wish the new members, Katja and Juriaan, good luck with their Ph.D..

I experienced jet-lag for the first time when I flew to Japan. I would like to thank Abdou Hassanien and Madoka Tokumoto-san from AIST for their hospitality and for inviting me there for a seminar. Abdou, your wife's pasta was the best remedy I have had against jet-lag. Thanks for all your help. _Shukran gazilan._ At NEC in Tsukuba, Yasunubu gave me the possibility to give a talk and arranged a tour through NEC in which I could see the TEM in which the nanotubes were first discovered. From Regensburg I would like to thank Milena

and Leo for their hospitality. I am sorry that I have no Luttinger liquid physics in my thesis.

From the 'higher' levels of the physics building I would like to thank (the always funny and laughing) Oleg, Alex, Omar, Wouter, Siggi, Yuli, and Yaroslav. I enjoyed the short conversations with Yuli at the smoker's corner, before I quit smoking a few years ago. I hope you will follow my example and also quit at some point. Yaroslav, I thank you for everything. You could always explain me the physics in simple ways. I also noticed, in Göteborg, that you could explain art just as effective.

From the MED group, I like to thank Murat, Oscar, Khashayar, Kevin, Edgar, Peter, Alberto, Menno, Andreas, and Benoit. The last three guys I wish good luck with the measurement of the zero-point motion of nanotubes. And Benoit, your old measurement program is still my standard. Peter, thank you for sharing your single electronics knowledge.

Many thanks to Cees Dekker for his interest in our research and the usage of MB facilies. From the MB group I like to mention Koen, Iddo and Derek.

Floor and Floris' efforts in trying to make QT a more sportive group are of great value. I enjoy very much on monday evening to play for the Real RKC. In Dordrecht I play soccer with AmNeDo *spor* and DMC. I like to thank all my friends in these two teams.

Before finishing I would like to thank my family and friends for all their love and support. And finally, I want to thank my wife, Zehra. Thank you for all your help, patience and love. *Seni çok seviyorum!*

<div align="right">

Sami Sapmaz
Dordrecht, May 2006

</div>

# Contents

# Chapter 1

# Introduction

Carbon is remarkable element which has many different stable forms ranging from 3D diamond to 2D graphite to 1D nanotubes and 0D fullerenes. In figure 1.1 these forms are shown. It is expected that new forms of carbon can be discovered anytime since much of the carbon phase diagram remains largely unexplored.

Carbon research was already considered a mature field at the time of the discovery of fullerenes in 1985 by the Nobel laureates Kroto, Smalley, Curl, and co-workers [1] and at the discovery of nanotubes in 1991 by Iijima [2]. These discoveries have given the field a boost.

The predicted remarkable one dimensionality and the quantum effects for the electronic properties has stimulated many scientist to enter the carbon research field. This last decade many intriguing effects with nanotubes have been observed by research groups all over the world. Delft University has contributed in many (especially low temperature) areas to this field as well. At low temperatures nanotubes exhibit most of their quantum effects such as single electron charging [3], Luttinger liquid behavior [4], electron interference [5], Kondo effect [6], and superconductivity [7] just to name a few. In this thesis we have focussed mainly on the single electron charging and the quantum dot properties in nanotubes.

The recent progress by different groups [10] on extending nanotube quantum dots to double quantum dots and defining them by tunable tunnelbarriers opens up new possibilities for nanotubes. The measurement of the orbital and spin relaxation times is one of them and will be very interesting. The orbital relaxation has been measured to be of the order of nanoseconds [13] in semiconductors quantum dots. This was mainly limited by phonon emission. The spin-relaxation time is much longer ($\sim 100\mu$s) [13] and is limited by the spin-orbit interaction in GaAs. For nanotubes there is hope that these time scales will be *much* longer, because the relaxation rate due to phonon emission is expected to be low, since most of the nanotube phonon modes have high energies and the spin-orbit in-
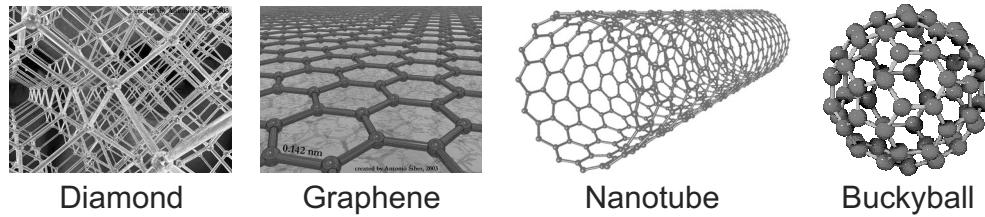
| Diamond | Graphene | Nanotube | Buckyball |

**Figure 1.1:** A few examples of the stable forms of carbon. Note the different dimensionalities of the various forms. They range from 3D diamond to 2D graphene to 1D nanotube and 0D buckyball ($C_{60}$). Images are taken from ref [16].

teraction is weak as carbon is a light element. Furthermore, carbon nanotubes should not suffer from reduced decoherence time due to the interaction between electrons and nuclear spins as in GaAs [15], because most of the carbon atoms is $^{12}C$ with zero nuclear spin magnetic moment. The research presented in the last chapter are the first steps in our efforts towards measuring the relaxation times.

# References

[1] H. W. Kroto, J. R. Heath, S. C. O'Brien, R. F. Curl, and R. E. Smalley, *$C_{60}$: Buckminsterfullerene.* Nature (London) **318**, 162 (1985)

[2] S. Iijima, *Helical Microtubules of Graphitic Carbon.* Nature (London) **354**, 56 (1991).

[3] S. J. Tans *et al.*, *Individual single-wall carbon nanotubes as quantum wires.* Nature (London) **386**, 474 (1997).

[4] M. Bockrath *et al.*, *Single-Electron Transport in Ropes of Carbon Nanotubes.* Science **275**, 1922 (1997).

[5] W. Liang *et al.*, *Fabry-Perot interference in a nanotube electron waveguide.* Nature (London) **411**, 665 (2001).

[6] J. Nygård, D. H. Cobden, and P. E. Lindelof, *Kondo physics in carbon nanotubes.* Nature (London) **408**, 342 (2000).

[7] A. Yu. Kasumov *et al.*, *Supercurrents through single-walled carbon nanotubes.* Science **284**, 1508 (1999).

[8] A. F. Morpurgo, J. Kong, C. M. Marcus, and H. Dai, *Gate-Controlled Superconducting Proximity Effect in Carbon Nanotubes.* Science **286**, 263 (1999).

[9] P. Jarillo-Herrero, J. A. van Dam, and L. P. Kouwenhoven, *Quantum supercurrent transistors in carbon nanotubes.* Nature (London) **439**, 953 (2006).

[10] M. J. Biercuk, S. Garaj, N. Mason, J. M. Chow, and C. M. Marcus, *Gate-defined quantum dots on carbon nanotubes.* Nano Lett. **5**, 1267 (2005).

[11] M. R. Gräber *et al.*, *Molecular states in carbon nanotube double quantum dots .* Cond-mat/0603367.

[12] S. Sapmaz, C. Meyer, P. Beliczynski, P. Jarillo-Herrero, L. P. Kouwenhoven, *Excited state spectroscopy in carbon nanotube double quantum dots.* to be published in Nano Letters.

[13] T. Fujisawa, D. G. Austing, Y. Tokura, Y. Hirayama, and S. Tarucha, *Allowed and forbidden transitions in artificial hydrogen and helium atoms.* Nature (London) **419**, 278 (2002).

[14] A. C. Johnson *et al.*, *Triplet-singlet spin relaxation via nuclei in a double quantum dot.* Nature (London) **435**, 925 (2005).

[15] F. H. L. Koppens *et al.*, *Control and detection of singlet-triplet mixing in a random nuclear field.* Science **309**, 1346 (2005).

[16] Diamond and Graphene: courtesy of Antinio Šiber.

# Chapter 2

# Theoretical background on carbon nanotubes and quantum dots

## 2.1  Carbon Nanotubes

Carbon nanotubes can be generally divided into two classes: single and multi walled carbon nanotubes (Fig. 2.1). The basic geometric structure of a single walled carbon nanotube can be simply expressed in one line: A single walled carbon nanotube is a hollow cylinder made entirely out of carbon atoms, which are positioned on a hexagonal lattice, has a typical diameter of 1 – 2 nm and can be centimeters long. Another way of saying roughly the same is: A single walled carbon nanotube can be viewed as a single sheet of graphene rolled up into a seamless hollow cylinder (Fig. 2.2). A multi walled carbon nanotube consists of concentric cylinders with an interlayer spacing of 3.4 Å and a diameter of typically 10 – 20 nm. In Fig. 2.1 examples of single and multi walled (3 walls) carbon nanotubes are shown.

This basic and simple structure of a single walled carbon nanotube (in the remaining of this chapter we will denote a single walled carbon nanotube just by nanotube) has many fascinating properties one can't express in a single sentence or even in a single chapter. However, in this section we will try to give a brief introduction to carbon nanotubes with the emphasis on electronic properties.

In 1991 the Japanese scientist S. Iijima discovered the first carbon nanotubes. There are many types of single wall carbon nanotubes since there are many ways to roll a graphene sheet to form a nanotube. A graphene sheet consists of a hexagonal lattice of $sp^2$ $\sigma$-bonds which are in the same plane with angles of 120°.

---

Much of the material presented in this section are adapted from L. C. Venema *et al.* [1] and P. Jarillo-Herrero *et al.* [2].
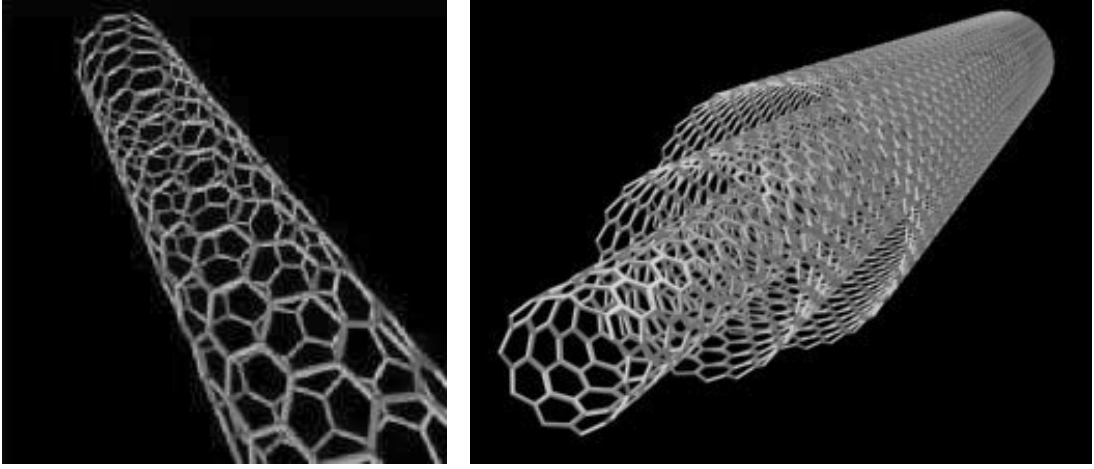
**Figure 2.1:** (left) A Single wall carbon nanotube (SWNT) and (right) multi wall carbon nanotube (MWNT). SWNTs are hollow cylinders with a typical diameter of 1–2 nm and are made entirely out of carbon atoms. MWNT consist of concentric cylinders. Here we show a MWNT with 3 walls. (image MWNT: Courtesy of Tsukasa Akasaka)

The fourth electron is in a $\pi$-orbital which has its lobes perpendicular to the plane of the sheet. The electronic properties of both graphene and carbon nanotubes can be well described by only taking into account the energy dispersion of the $\pi$-electrons [3, 4, 5].

One way to construct a nanotube is shown in figure 2.2. It is sufficient to uniquely define a nanotube by the chiral vector $\vec{C} = n\vec{a_1} + m\vec{a_2}$, where $n$ and $m$ are integers and $\vec{a_1}$ and $\vec{a_2}$ are the unit vectors of the hexagonal lattice. Each $(n, m)$ pair corresponds to a specific chiral angle, $\phi$, and diameter, $d$:

$$\phi = \arccos\left(\frac{\sqrt{3}(n+m)}{2\sqrt{n^2 + m^2 + nm}}\right) \tag{2.1}$$

$$d = \frac{a}{\pi}\sqrt{n^2 + m^2 + nm} \tag{2.2}$$

where $a = |\vec{a_i}| = 2.46$ Å is the lattice constant. In the example of figure 2.2 the $(n, m)$ indices are (12,4), which corresponds to a nanotube with a diameter $d$ of 1.13 nm and a chiral angle $\phi$ of 16.1°. Vector $\vec{T}$ is perpendicular to $\vec{C}$ and it points from (0,0) to the first lattice site through which the dashed line passes exactly. The area defined by $|\vec{T} \times \vec{C}|$ is the primitive unit cell from which a nanotube can be constructed.

Special symmetry directions in the graphene lattice are $(n, 0)$ and $(n, n)$, which are respectively called the zigzag and armchair directions and they differ by an
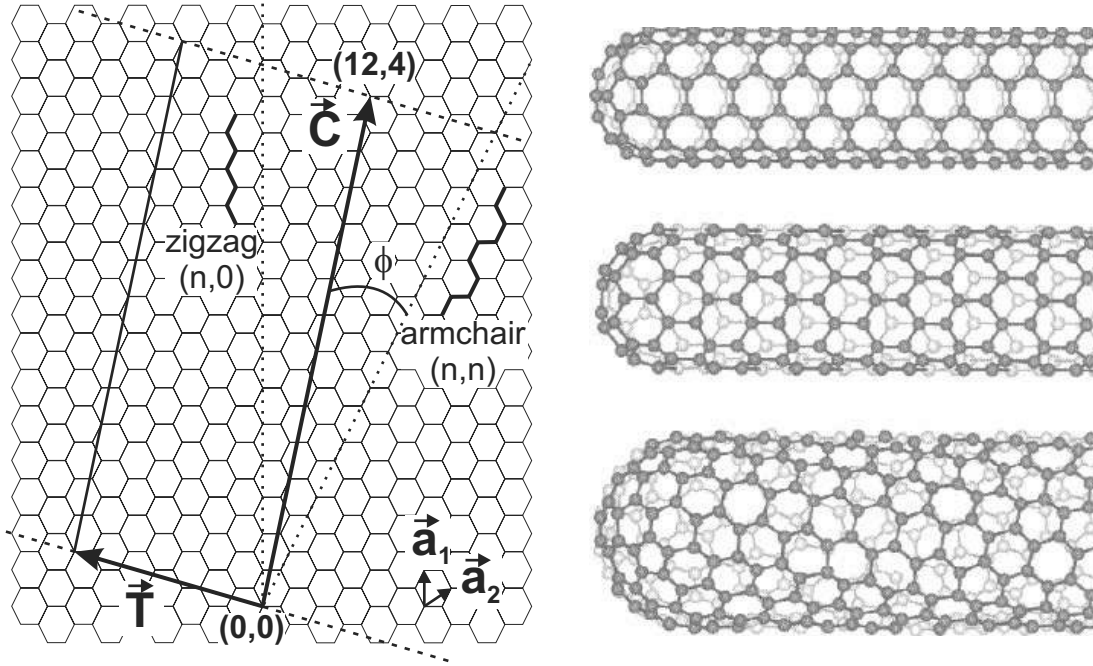
**Figure 2.2:** (left) A graphene sheet that can be folded into a seamless cylinder by cutting out the sheet along the dashed lines and rolling it up along vector $\vec{C}$. $\vec{a_1}$ and $\vec{a_2}$ are the unit vectors of the hexagonal graphene sheet. The zigzag and armchair lines (dotted) are special symmetry directions. The corresponding patterns along the nanotube circumference are drawn near the dotted lines. (right) Carbon nanotubes with different geometries. From top to bottom, an armchair (5,5), a zigzag (9,0) and a chiral (10,5) are shown.

angle of 30°. Rolling up a sheet along one of these directions results in a non-chiral nanotube. Fig. 2.2 shows examples of an armchair, a zigzag and chiral tube. The names armchair and zigzag refer to the pattern of carbon bonds along the circumference (see Fig. 2.2). These electronic properties are found to be critically dependent on the chirality and diameter. A (12,4) nanotube for example is semiconducting, however, a (12,3) nanotube, which has only a slightly different vector $\vec{C}$, is metallic.

In figure 2.3a, the real space geometry of graphene (a triangular Bravais lattice with a two atom basis) is shown. There are two inequivalent sites in the hexagonal carbon lattice, labelled A and B. All other lattice sites can be mapped onto these two by a suitable translation using vectors $\vec{a_1}$ and $\vec{a_2}$. The real space unit cell contains the two carbon atoms at A and B. Figure 2.3b shows the reciprocal space lattice, with the corresponding reciprocal space vectors and Brillouin zone. In a tight binding approximation, the energy dispersion for the $\pi$-electrons forming a
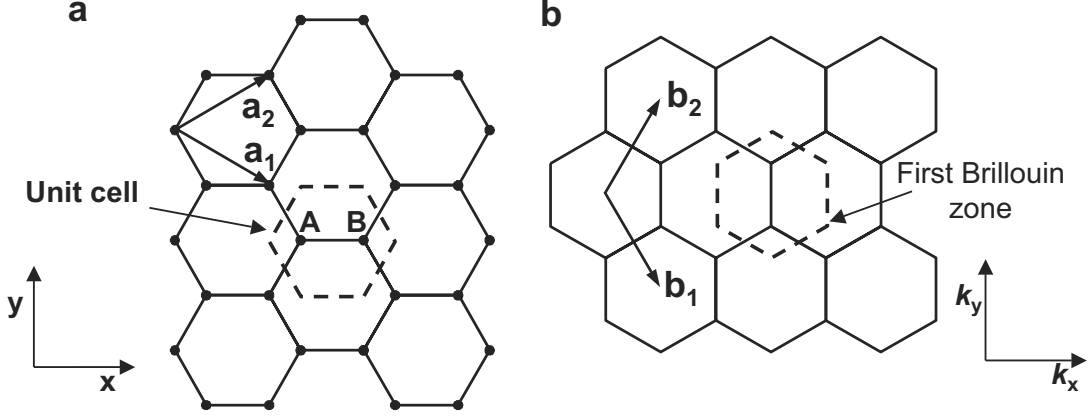
**Figure 2.3: (a)** Real space atomic lattice of graphene. **(b)** Reciprocal space lattice. The unit cells are the area within the dashed borders. The unit vectors are $\vec{a_1} = (\frac{\sqrt{3}a}{2}, \frac{a}{2})$, $\vec{a_2} = (\frac{\sqrt{3}a}{2}, -\frac{a}{2})$ and $\vec{b_1} = (\frac{2\pi}{\sqrt{3}a}, \frac{2\pi}{a})$, $\vec{b_2} = (\frac{2\pi}{\sqrt{3}a}, -\frac{2\pi}{a})$.

bonding (-) and antibonding (+) band can be found to be [6]:

$$E(k_x, k_y) = \pm\gamma_0\sqrt{1 + 4\cos(\frac{\sqrt{3}k_x a}{2})\cos(\frac{k_y a}{2}) + 4\cos^2(\frac{k_x a}{2})}, \tag{2.3}$$

where $\gamma_0 \sim 2.7$ eV is the energy overlap integral between nearest neighbors.

The energy dispersion relation for graphene, $E(k_x, k_y)$, is plotted in Fig. 2.4a. Valence and conduction bands 'touch' each other at six points, which coincide with the corners of the hexagonal Brillouin zone. The Fermi surface reduces thus just to these six points. Due to this, graphene is called a semimetal, or zero band gap semiconductor. These special points, where conduction and valence bands meet, are called 'K-points'. The dispersion relation near these points is conical. Figure 2.4b shows a contour plot of the energy of the valence band states. The circular contours around the K-points reflects the conical shape of the dispersion relation around them. Only two of the six K-points are inequivalent (resulting from the two inequivalent atom sites of the graphene lattice), labelled $\vec{K}_1$ and $\vec{K}_2 = -\vec{K}_1$. In Fig. 2.4b, the lower two K-points on the hexagon sides can be reached from $\vec{K}_1$ by a suitable reciprocal lattice vector translation, so they are equivalent to $\vec{K}_1$. Similarly, the two upper K-points are equivalent to $\vec{K}_2$.

The electronic properties of a conductor are determined by the electrons near the Fermi energy. Therefore the shape and position of the dispersion cones near the K-points is of fundamental importance in understanding electronic transport in graphene, and therefore in nanotubes. The two K-points, $\vec{K}_1$ and $\vec{K}_2$ in Fig. 2.4b have coordinates $(k_x, k_y) = (0, \pm 4\pi/3a)$. The slope of the cones is $(\sqrt{3}/2)\gamma_o a$.
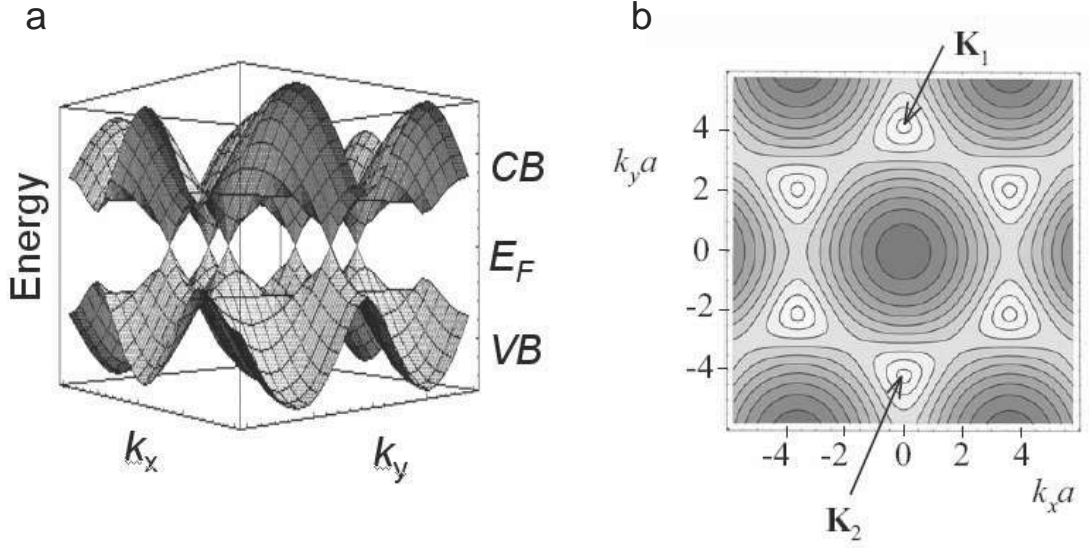
**Figure 2.4:** Graphene band structure. **(a)** Energy dispersion relation for graphene. The valence (VB) and conduction (CB) bands meet at six points at the Fermi energy, $E_F$. **(b)** Contour-plot of the valence band states energies in **(a)** (darker indicates lower energy). The hexagon formed by the six K-points (white contour points) defines the first Brillouin zone of the graphene band structure. Outside this unit cell, the band structure repeats itself. The two inequivalent points, $\vec{K}_1$ and $\vec{K}_2$ are indicated by arrows (adapted from ref. [7]).

A nanotube is a graphene sheet folded into a cylinder. From the bandstructure of graphene we can obtain the nanotube's bandstructure by imposing appropriate boundary conditions along the circumference. Typically, the diameters of carbon nanotubes ($\sim$ few nm) are much smaller than their lengths (anywhere from hundreds of nm to several cm). As a result, there is a very large difference in the spacing between the quantized values of the wavevectors in the directions perpendicular, $k_\perp$, and parallel, $k_{||}$, to the tube axis. In this section, we will regard $k_{||}$ to be effectively continuous (infinitely long NTs) and consider only the quantization effects due to the small diameter of NTs (section 2.3 will cover the quantum effects associated to finite length CNTs, which constitute the actual subject of this thesis).

By imposing periodic boundary conditions around the NT circumference we obtain the allowed values of $k_\perp$:

$$\vec{C} \cdot \vec{k} = \pi d k_\perp = 2\pi j, \tag{2.4}$$

where $d$ is the NT diameter and $j$ is an integer number. The small diameter of CNTs makes the spacing in $k_\perp$ to be rather large ($\Delta k_\perp = 2/d$), resulting in strong
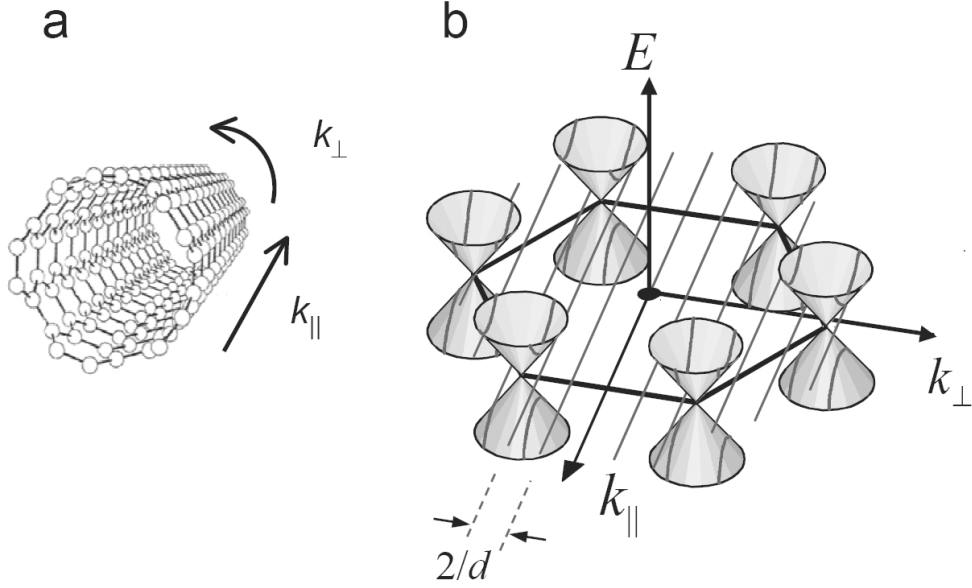
**Figure 2.5:** Quantized one-dimensional (1D) subbands. **(a)** CNT and direction of $k$-axis. **(b)** Low-energy band structure of graphene (near $E_F$), showing the one-dimensional subbands of CNTs obtained by imposing periodic boundary conditions along the NT circumference (adapted from [7]).

observable effects even at room temperature. The quantization of $k_\perp$ leads to a set of 1-dimensional subbands in the longitudinal direction (intersection of vertical planes parallel to $k_\parallel$ with the band structure of graphene). These are shown in Fig. 2.5b. The electronic states closest to the Fermi energy lie in the subbands closest to the K-points. One of the most remarkable properties of CNTs becomes apparent now: if a subband passes exactly through the middle of a dispersion cone, then the nanotube will be metallic. If not, then there will be an energy gap between valence and conduction bands and the nanotube will be a semiconductor. To first approximation, all nanotubes fall into one of these categories: either they are metallic or semiconductors. In fact, for a given $(n, m)$ nanotube, we can calculate $n - m = 3q + p$, where $q$ is an integer and $p$ is -1, 0 or +1 [8]. If $p = 0$, then there is an allowed value of $k_\perp$ that intercepts the K-points, and the nanotube is metallic. The Fermi velocity in metallic nanotubes determines the slope of the dispersion cones: $dE/dk = \hbar v_F$, with $v_F \sim 8 \cdot 10^5$ m/s [9]. For $p = \pm 1$, there is no allowed value of $k_\perp$ intercepting the K-points, resulting then in a semiconducting nanotube (see Fig. 2.6). The closest $k_\perp$ to the K-points misses them by $\Delta k_\perp = \pm 2/3d$, for $p = \pm 1$, respectively. This means that the value of the band gap is: $E_g = 2(dE/dk)\Delta k_\perp = 2\gamma_o a/(\sqrt{3}d) \sim 0.8$ eV/$d$[nm],
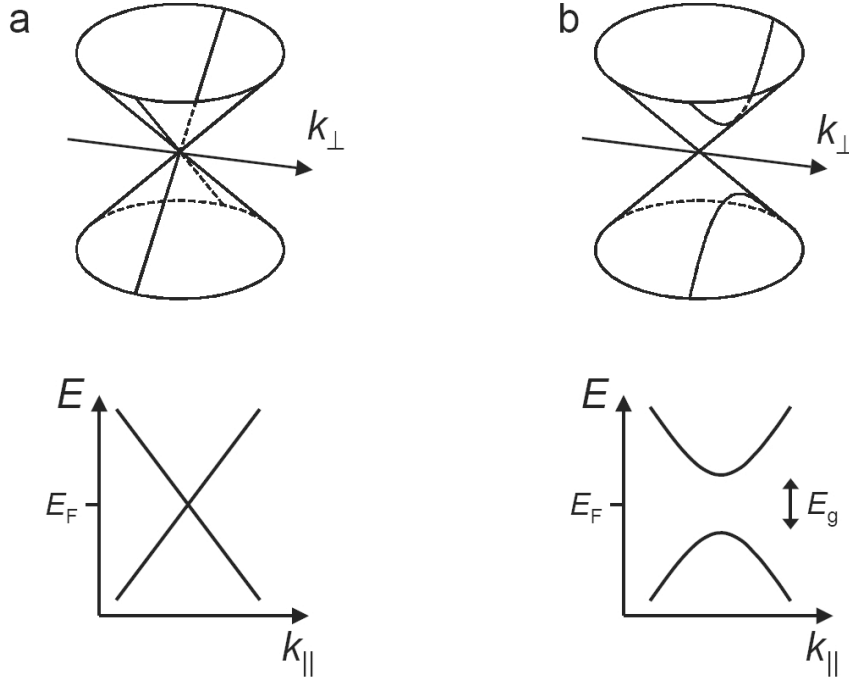
**Figure 2.6:** Low energy band diagrams for carbon nanotubes around the $\vec{K}_1$ point. **(a)** For $p = 0$, there is an allowed value of $k_\perp$ whose subband passes through $\vec{K}_1$, resulting in a metallic nanotube and band structure. **(b)** For $p = 1$, the closest subband to $\vec{K}_1$ misses it by $\Delta k_\perp = 2/3d$, resulting in a semiconducting nanotube with band gap $E_g$. In both figures, $E_F$ refers to the value of the Fermi energy in graphene.

independent of the chiral angle. Of all carbon nanotubes, approximately 1/3 are metallic and 2/3 are semiconducting.

It is quite remarkable that carbon nanotubes can be metallic or semiconducting depending on chirality and diameter, despite the fact that there is no difference in the local chemical bonding between the carbon atoms in the different tubes. This fact results from an elegant combination of quantum mechanics and the peculiar band structure of graphene.

The low energy band structure of carbon nanotubes is doubly degenerate (at zero magnetic field). By this we mean that at a given energy there are two different orbital electronic states that can contribute to transport (there is also an additional two-fold degeneracy due to spin). This degeneracy has been interpreted in a semiclassical fashion as the degeneracy between clockwise (CW) and counter-clockwise (CCW) propagating electrons along the nanotube circumference [10]. Within this picture, CW and CCW electrons in CNTs have opposite classical magnetic moments associated with them, which, in the absence of a magnetic field, are degenerate (also opposite spin states are degenerate at

single molecule   self-assembled QD   lateral QD   nanotube
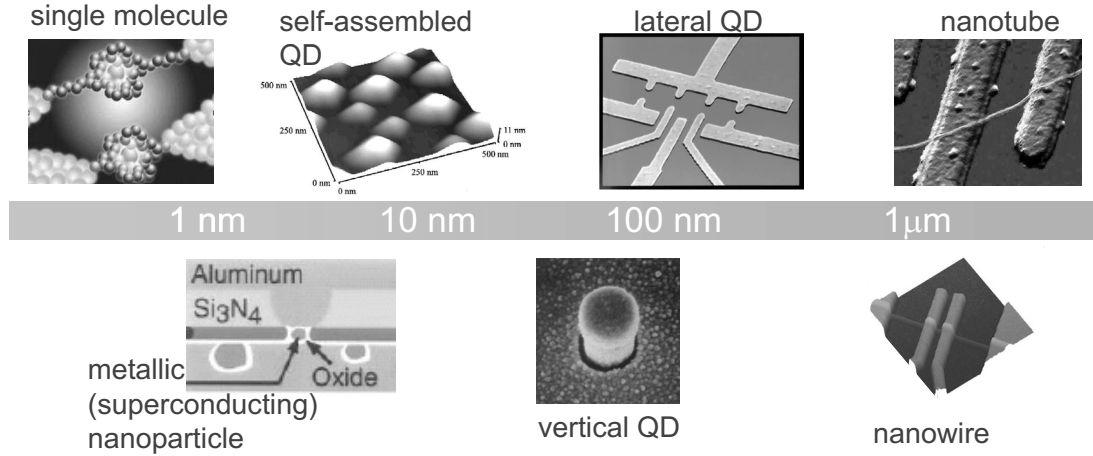
1 nm   10 nm   100 nm   1μm

metallic (superconducting) nanoparticle   vertical QD   nanowire

**Figure 2.7:** Examples of different systems with a variety of sizes and aspect ratios behaving as quantum dots. Images are taken from Ref. [12].

zero magnetic field). This orbital degeneracy plays a fundamental role in the transport properties of carbon nanotubes.

## 2.2   Quantum Dots

A quantum dot is simply a 'small' box with a discrete set of energy states that can be filled with electrons. Quantum mechanics tells us that electrons in a finite size object have a discrete energy spectrum, so, in an experiment, a small structure behaves like a quantum dot (QD) if the separation between the energy levels is observable at the temperature we are working at. For most nanostructures this involves working at temperatures below a few Kelvin. The lifetime of the energy levels must be long enough to be able to observe them, and this means that the electrons must be (at least partially) confined. Because a quantum dot is such a general kind of system, there exist QDs of many different sizes and materials: for instance single molecules, metallic nanoparticles, semiconductor self-assembled quantum dots and nanocrystals, lateral or vertical dots in semiconductor heterostructures, semiconducting nanowires or carbon nanotubes (see for example Fig. 2.7). Quantum dots are mostly studied by means of optical spectroscopy or electronic transport techniques. In this thesis we have used the latter to study quantum dots defined in short segments of carbon nanotubes. But before discussing CNT QDs, we present here a general description of electronic

---

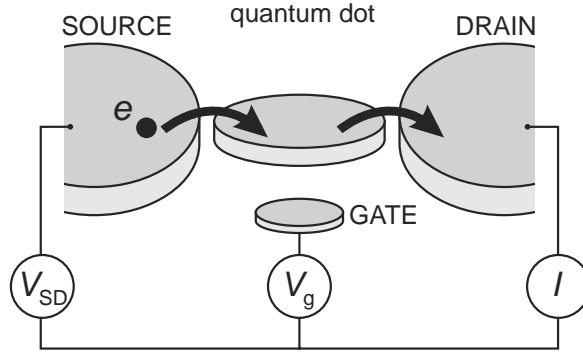This section is adapted from J.M. Elzerman *et al.* [11].

**Figure 2.8:** Schematic picture of a quantum dot. The quantum dot (represented by a disk) is connected to source and drain contacts via tunnel barriers, allowing the current through the device, $I$, to be measured in response to a bias voltage, $V_{SD}$ and a gate voltage, $V_g$.

transport through quantum dots.

In order to measure electronic transport through a quantum dot, this must be attached to a source and drain reservoirs, with which particles can be exchanged. (see Fig. 2.8). By attaching current and voltage probes to these reservoirs, we can measure the electronic properties of the dot. The QD is also coupled capacitively to one or more 'gate' electrodes, which can be used to tune the electrostatic potential of the dot with respect to the reservoirs.

Electronic properties of quantum dots are conveniently understood using the constant interaction (CI) model [13]. This model makes two important assumptions. First, the Coulomb interactions among electrons in the dot are captured by a single constant capacitance, $C$. This is the total capacitance to the outside world, i.e. $C = C_S + C_D + C_g$, where $C_S$ is the capacitance to the source, $C_D$ that to the drain, and $C_g$ to the gate. Second, the discrete energy spectrum is independent of the number of electrons on the dot. Under these assumptions the total energy of a $N$-electron dot with the source-drain voltage, $V_{SD}$, applied to the source (and the drain grounded), is given by

$$U(N) = \frac{[-|e|(N - N_0) + C_S V_{SD} + C_g V_g]^2}{2C} + \sum_{n=1}^{N} E_n(B) \tag{2.5}$$

where $-|e|$ is the electron charge and $N_0$ the number of electrons in the dot at zero gate voltage. The terms $C_S V_{SD}$ and $C_g V_g$ can change continuously and represent the charge on the dot that is induced by the bias voltage (through the capacitance $C_S$) and by the gate voltage $V_g$ (through the capacitance $C_g$), respectively. The last term of Eq. 2.5 is a sum over the occupied single-particle energy levels $E_n(B)$, which are separated by an energy $\Delta E_n = E_n - E_{n-1}$. These
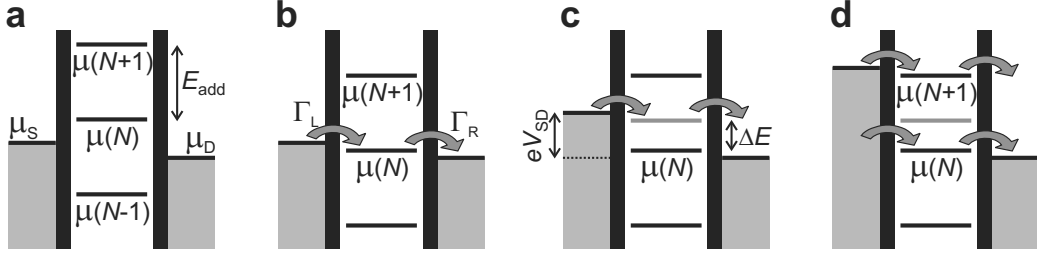
**Figure 2.9:** Schematic diagrams of the electrochemical potential of the quantum dot for different electron numbers. **(a)** No level falls within the bias window between $\mu_S$ and $\mu_D$, so the electron number is fixed at $N-1$ due to Coulomb blockade. **(b)** The $\mu(N)$ level is aligned, so the number of electrons can alternate between $N$ and $N-1$, resulting in a single-electron tunneling current. The magnitude of the current depends on the tunnel rate between the dot and the reservoir on the left, $\Gamma_L$, and on the right, $\Gamma_R$. **(c)** Both the ground-state transition between $N-1$ and $N$ electrons (black line), as well as the transition to an $N$-electron excited state (gray line) fall within the bias window and can thus be used for transport (though not at the same time, due to Coulomb blockade). This results in a current that is different from the situation in **(b)**. **(d)** The bias window is so large that the number of electrons can alternate between $N-1$, $N$ and $N+1$, i.e. two electrons can tunnel onto the dot at the same time.

energy levels depend on the characteristics of the confinement potential. Note that, within the CI model, only these single-particle states depend on magnetic field, $B$.

To describe transport experiments, it is often more convenient to use the electrochemical potential, $\mu$. This is defined as the minimum energy required to add an electron to the quantum dot:

$$\mu(N) \equiv U(N) - U(N-1) =$$
$$= (N - N_0 - \frac{1}{2})E_C - \frac{E_C}{|e|}(C_S V_{SD} + C_g V_g) + E_N \tag{2.6}$$

where $E_C = e^2/C$ is the charging energy. The electrochemical potential for different electron numbers $N$ is shown in Fig. 2.9a. The discrete levels are spaced by the so-called addition energy, $E_{add}(N)$:

$$E_{add}(N) = \mu(N+1) - \mu(N) = E_C + \Delta E. \tag{2.7}$$

The addition energy consists of a purely electrostatic part, the charging energy $E_C$, plus the energy spacing between two discrete quantum levels, $\Delta E$. Note that $\Delta E$ can be zero, when two consecutive electrons are added to the same spin-degenerate level or if there are additional degeneracies present.

For transport to occur, energy conservation needs to be satisfied. This is the case when an electrochemical potential level lies within the 'bias window' between the electrochemical potential (Fermi energy) of the source ($\mu_S$) and the drain ($\mu_D$), i.e. $\mu_S \geq \mu \geq \mu_D$ with $-|e|V_{SD} = \mu_S - \mu_D$. Only then can an electron tunnel from the source onto the dot, and then tunnel off to the drain without losing or gaining energy. The important point to realize is that since the dot is very small, it has a very small capacitance and therefore a large charging energy – for typical dots $E_C \approx$ a few meV. If the electrochemical potential levels are as shown in Fig. 2.9a, this energy is not available (at low temperatures and small bias voltage). So, the number of electrons on the dot remains fixed and no current flows through the dot. This is known as Coulomb blockade.

The charging energy becomes important when it exceeds the thermal energy, $k_B T$, and when the barriers are sufficiently opaque such that the electrons are located either in the reservoirs or in the dot. The latter condition implies that quantum fluctuations in the number of electrons on the dot must be sufficiently small. A lower bound for the tunnel resistances $R_t$ of the barriers can be found from the Heisenberg uncertainty principle. The typical time $\Delta t$ to charge or discharge the dot is given by the $RC$-time. This yields $\Delta E \Delta t = (e^2/C) R_t C > h$. Hence, $R_t$ should be much larger than the quantum resistance $h/e^2$ to sufficiently reduce the uncertainty in the energy.

The Coulomb blockade can be lifted by changing the voltage applied to the gate electrode and thus shifting the whole 'ladder' of electrochemical potential levels up or down. When a level falls within the bias window, the current through the device is switched on. In Fig. 2.9b $\mu(N)$ is aligned, so the electron number alternates between $N - 1$ and $N$. This means that the $N$th electron can tunnel onto the dot from the source, but only after it tunnels off to the drain can another electron come onto the dot again from the source. This cycle is known as single-electron tunneling.

By sweeping the gate voltage and measuring the current, we obtain a trace as shown in Fig. 2.10a. At the positions of the peaks, an electrochemical potential level is aligned with the source and drain and a single-electron tunneling current flows. In the valleys between the peaks, the number of electrons on the dot is fixed due to Coulomb blockade. By tuning the gate voltage from one valley to the next one, the number of electrons on the dot can be precisely controlled. The distance between the peaks corresponds to $E_C + \Delta E$, and can therefore give information about the energy spectrum of the dot.

A second way to lift Coulomb blockade is by changing the source-drain voltage, $V_{SD}$ (see Fig. 2.9c). (In general, we keep the drain potential fixed, and change only the source potential.) This increases the bias window and also 'drags' the
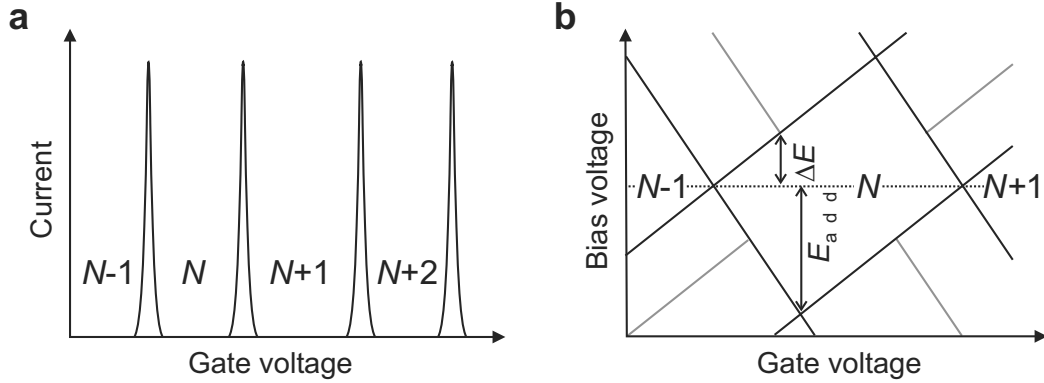
**Figure 2.10:** Transport through a quantum dot. **(a)** Coulomb peaks in current versus gate voltage in the linear-response regime. **(b)** Coulomb diamonds in differential conductance, $dI/dV_{SD}$, versus $V_{SD}$ and $V_g$, up to large bias. The edges of the diamond-shaped regions (black) correspond to the onset of current. Diagonal lines emanating from the diamonds (gray) indicate the onset of transport through excited states.

electrochemical potential of the dot along, due to the capacitive coupling to the source. Again, a current can flow only when an electrochemical potential level falls within the bias window. By increasing $V_{SD}$ until both the ground state as well as an excited state transition fall within the bias window, an electron can choose to tunnel not only through the ground state, but also through an excited state of the $N$-electron dot. This is visible as a change in the total current. In this way, we can perform excited-state spectroscopy.

Usually, we measure the current or differential conductance (the derivative of the current with respect to the source-drain bias) while sweeping the bias voltage, for a series of different values of the gate voltage. Such a measurement is shown schematically in Fig. 2.10b. Inside the diamond-shaped region, the number of electrons is fixed due to Coulomb blockade, and no current flows. Outside the diamonds, Coulomb blockade is lifted and single-electron tunneling can take place (or for larger bias voltages even double-electron tunneling is possible, see Fig. 2.9d). Excited states are revealed as changes in the current, i.e. as peaks or dips in the differential conductance. From such a 'Coulomb diamond' the excited-state energy as well as the charging energy can be read off directly.

The simple model described above explains successfully how quantization of charge and energy leads to effects like Coulomb blockade and Coulomb oscillations. Nevertheless, it is too simplified in many respects. For instance, the model considers only first-order tunneling processes, in which an electron tunnels first from one reservoir onto the dot, and then from the dot to the other reservoir. But when the tunnel rate between the dot and the leads, $\Gamma$, is increased, higher-order

tunneling via virtual intermediate states becomes important. Such processes, which are known as 'cotunneling' [14], can be very useful in performing detailed spectroscopy. Furthermore, the simple model does not take into account the spin of the electrons, thereby excluding for instance exchange effects.

## 2.3   Nanotube Quantum Dots
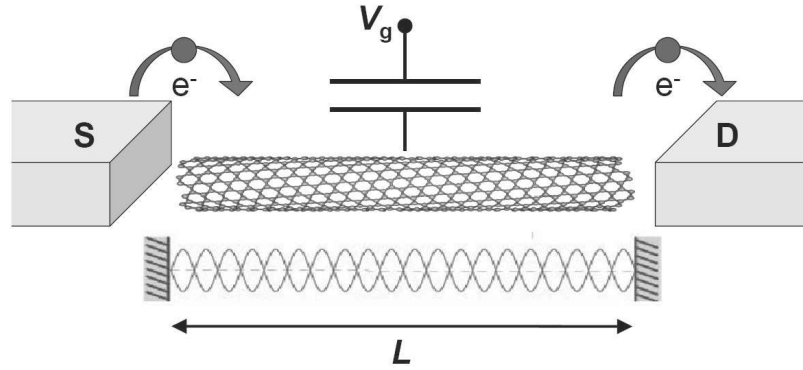


**Figure 2.11:** Schematic picture of a carbon nanotube quantum dot. Two metal electrodes, source (S) and drain (D), separated by a distance $L$ are deposited on top of the tube. The QD is formed in the segment of nanotube in between the electrodes, leading to a quantized energy spectrum in the longitudinal direction. The NT is capacitively coupled to a gate electrode (usually the back gate plane of the silicon substrate).

In section 2.1 we described the basic electronic properties of infinitely long nanotubes. Due to the quantization of momentum in the traversal direction, nanotubes are usually treated as one-dimensional objects. In an actual experiment we measure NTs of finite length and expect therefore that quantum effects associated with this finite length will be observable if we measure NTs with short lengths and at low temperatures. under these conditions, the discrete levels originating from the zero-dimensional nature of the nanotubes electronic states will manifest itself and NTs will behave as quantum dots.

When two metallic electrodes are deposited on top of a CNT, tunnel barriers develop naturally at the NT-metal interfaces. The separation between the electrodes, $L$, determines then the QD length (see Fig. 2.11). A finite $L$ results in quantized energy levels in the longitudinal direction, with an energy level separation $\Delta$. The strength of the NT-metal tunnel barriers determines the degree of

---

Parts of this section are adapted from P. Jarillo-Herrero *et al.* [2].

confinement of electrons in the NT QD. For very opaque barriers, the tunnel rate between the QD and the reservoirs, $\Gamma$, is very small, resulting in a large lifetime of the electrons in the QD (or small energy broadening). If the barriers become more transparent (i.e., more transmissive), the energy levels get '$\Gamma$-broadened'. In order to be able to observe clearly the discreteness of the energy spectrum for any QD it is required that $h\Gamma < \Delta$. Depending on the ratio between the lifetime broadening and the charging energy, we can distinguish three different QD regimes (with different typical phenomena associated with them):

1. $h\Gamma \ll E_C$ (Closed QD regime)$\longrightarrow$ Charging effects dominate transport (Coulomb blockade).

2. $h\Gamma \leq E_C$ (Intermediate transparency regime) $\longrightarrow$ Charging effects important, but higher-order tunneling processes significant too (cotunneling and Kondo effect).

3. $h\Gamma \gg E_C$ (Open QD regime)$\longrightarrow$ Quantum interference of non-interacting electrons (Fabry-Perot like interference).

The experiments described in this thesis explore mainly the first regime. Only in chapter 8 we demonstrate the tunability of the tunnelbarriers by showing Fabry-Perot like interference (i.e. operate in regime 3).

The coupling between the NT and the metal leads depends on the contact material, NT diameter and metallic/semiconducting character of the NT. Certain materials, such as Ti or Au, make (generally) good contact to nanotubes (especially metallic ones). Others, like Al make pretty bad contact. It has recently been shown that Pd and Rh are very good materials to contact NTs [15, 16, 17]. The larger the diameter, the lower the contact resistance is (on average). It is also easier to contact metallic NTs than semiconducting ones because the latter typically develop a Schottky barrier at the NT-metal interface. Despite these guidelines, it is still not possible to obtain a desired contact resistance when depositing metal on top of a CNT.

If we assume hard wall boundary conditions, then the quantized values of the wavevector in the longitudinal direction, $k_{||}$, are separated by $\Delta k_{||} = \pi/L$. In the case of metallic nanotubes this leads to an energy level spacing, $\Delta$, given by

$$\Delta = \frac{dE}{dK_{||}}\Delta k_{||} = \frac{hv_F}{2L} \tag{2.8}$$

It turns out that due to the high Fermi velocity in metallic CNTs, $\Delta$ is actually quite large ($\Delta \sim 1.7$ meV/$L[\mu$m]), and, for typical $L$ ($\sim$ few hundreds

of nm), the quantum behaviour of CNTs can be observed even at temperatures of a few K. Another interesting consequence of Eq. 2.8 is that the energy level spacing in CNT QDs is constant, i.e., independent of the number of electrons, $N$. This doesn't occur in other types of QDs, such as those defined in 2-dimensional electron gases in semiconductor heterostructures, where the energy level spacing becomes very small as the QDs are filled with more and more e$^-$, and also the spectrum becomes more complicated as $N$ increases. A NT QD can contain thousands of e$^-$ and still have a relatively simple spectrum. Because of their small size, nanotubes in the closed QD regime have also rather large charging energies (typically $\sim$5-20 meV). These large charging energies, large energy level spacings and the simplicity of the spectrum make metallic NTs a very suitable system to study QD physics.

The constant interaction model together with Eq. 2.8 for the energy spectrum is a good starting point to analyze measurements on NT QDs in the Coulomb blockade regime [18, 19]. However, more complete models are necessary to explain the spectrum of NT QDs, and especially the excitation spectrum energies. The CI model doesn't take into account exchange effects, for example, and Eq. 2.8 doesn't take into account the double orbital degeneracy of the NT band structure. Below we will explain a model proposed by Oreg *et al.* [20], which incorporates these effects into the constant interaction model. In chapter 5 we use this model to analyze our data and find remarkable agreement between theory and experiment.

In the Oreg-*et al.* model the Hamiltonian of the nanotube quantum dot can be written in terms of 5 parameters: Mean level spacing $\Delta$, the energy mismatch $\delta$ which lifts the orbital degeneracy (Fig. 2.12), the charging energy $E_C$, the exchange energy $J$ that favors spin alignment, and the excess Coulomb energy d$U$ to put two electrons into a single level. Here, $\Delta$ is the mean level spacing the quantization of

$$H = \sum_{\mu,\sigma,l} \varepsilon_{l\mu} n_{l\mu\sigma} + \frac{1}{2} E_C \left( \frac{Q_{\text{dot}} - Q_{\text{ext}}}{e} \right)^2 + \text{d}U \sum_{\mu,l} n_{l\mu\uparrow} n_{l\mu\downarrow} + J \sum_{\mu,\mu`} N_{\mu\uparrow} N_{\mu'\downarrow}, \quad (2.9)$$

where $\epsilon_{l,\mu} = l\Delta + (\mu - 1)\delta$ is the energy of the $l$th quantum level originating from the $\mu$th subband ($\mu = 1, 2$), $Q_{\text{dot}}$ is the excess charge on the nanotube, $Q_{\text{ext}}$ is the gate-induced charge on the dot, $n_{l\mu\sigma}$ is the number operator for the $l$th level with spin $\sigma$ in the $\mu$th subband, and $N_{\mu\sigma}$ is the total number of electrons with spin $\sigma$ in the $\mu$th subband. Within this model the five parameters completely determine the energies of all the possible spin-electronic configurations.

The electrochemical potentials and the addition energies (Fig. 2.12) can be
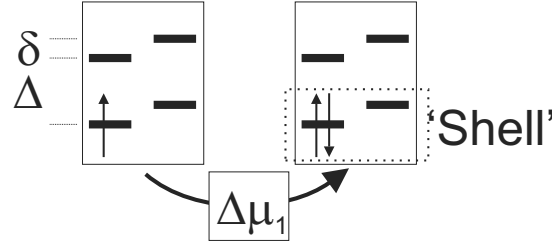
**Figure 2.12:** In the simplest picture of a nanotube quantum dot, the quantization of the subbands leads to two sets of spin-degenerate electronic levels with a mean spacing $\Delta$ within each set. The energy mismatch between the sets can be represented by $\delta$. The addition energy $\Delta\mu_1$ is defined such that it is the energy required to put one more electron in the nanotube quantum dot, which already contains one electron in the last occupied 'shell'.

easily calculated from Eq. 2.9. We find for the addition energies

$$
\begin{aligned}
\Delta\mu(1) &= E_C + \mathrm{d}U + J \\
\Delta\mu(2) &= E_C + \delta - \mathrm{d}U \\
\Delta\mu(3) &= E_C + \mathrm{d}U + J = \Delta\mu(1) \\
\Delta\mu(4) &= E_C + \Delta - \delta - \mathrm{d}U
\end{aligned}
\tag{2.10}
$$

for the situation that $\delta > J + \mathrm{d}U$. When $\delta < J + \mathrm{d}U$ the addition energies are

$$
\begin{aligned}
\Delta\mu(1) &= E_C + \delta \\
\Delta\mu(2) &= E_C - \delta + \mathrm{d}U + 2J \\
\Delta\mu(3) &= E_C + \delta = \Delta\mu(1) \\
\Delta\mu(4) &= E_C + \Delta - \delta - \mathrm{d}U.
\end{aligned}
\tag{2.11}
$$

## 2.4   Double Quantum Dots

The next logical step after studying individual quantum dots is to study systems of more than one dot. Where single quantum dots are regarded as 'artificial atoms', two quantum dots can be coupled to form an 'artificial molecule'. Depending on the strength of the interdot coupling, the two dots can form ionic-like (weak tunnel coupling) or covalent-like bonds (strong tunnel coupling). In the case of ionic bonding the electrons are localized on the individual dots. The binding occurs, because a static redistribution of electrons leads to an attractive Coulomb interaction. In the case of covalent bonding, two electron states

---

Much of the material presented in this section is adapted from van der Wiel *et al.* [21].
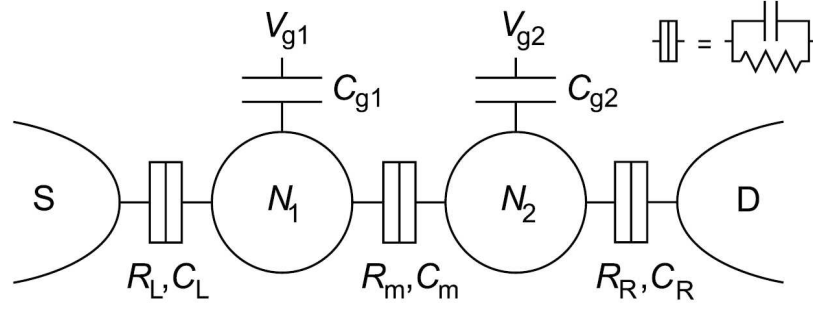
**Figure 2.13:** Network of resistors and capacitors representing two quantum dots coupled in series.

are quantum-mechanically coupled. The main requirement for covalent binding is that an electron can tunnel many times between the two dots in a phase-coherent way. Here the electron cannot be regarded as a particle that resides in one particular dot, but it must be thought of as a coherent wave that is delocalized over the two dots. The bonding state of a strongly coupled artificial molecule has a lower energy than the energies of the original states of the individual dots. This energy gain forms the binding force between the two dots.

The theoretical possibility to perform certain tasks in a much more efficient way using a 'quantum computer' instead of a 'classical computer', has stimulated the search for physical realizations of the basic building block of such a computer: the quantum bit. In principle, any quantum two-level system can be used as such a qubit. In particular, recent studies have put forward double quantum dots as interesting candidates for realizing qubits [22]. The possibility of using double quantum dots is an important motivation for the work presented in chapter 8.

As a first step to understanding double dot systems we introduce the stability diagram, or honeycomb diagram. Let's start with a purely classical description to keep things simple. The double dot is modeled as a network of resistors and capacitors (Fig. 2.13). The number of electrons on 1(2) is $N_{1(2)}$. Each dot is capacitively coupled to a gate voltage $V_{g1(2)}$ through a capacitor $C_{g1(2)}$ and to the source (S) or drain (D) contact through a tunnel barrier represented by a resistor $R_{L(R)}$ and a capacitor $C_{L(R)}$ connected in parallel. The dots are coupled to each other by a tunnel barrier represented by a resistor $R_m$ and a capacitor $C_m$ in parallel. The bias voltage, $V$, is applied to the source contact with the drain contact grounded (asymmetric bias).

In the linear transport regime ($V \approx 0$) the electrochemical potential of the
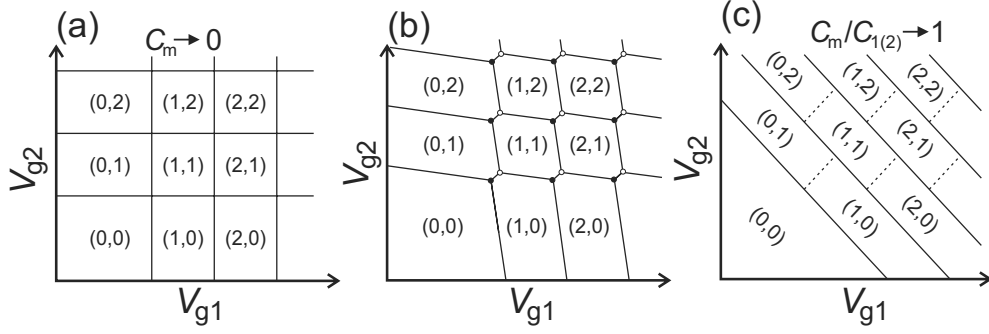
**Figure 2.14:** Schematic stability diagrams of the double quantum dot system for **(a)** small, **(b)** intermediate, and **(c)** large inter-dot coupling. The equilibrium charge state on each dot in each domain is denoted by $(N_1, N_2)$.

two dots are (for a full derivation see Ref. [21])

$$\mu_1(N_1, N_2) = (N_1 - \frac{1}{2})E_{C1} + N_2 E_{Cm} - \frac{1}{|e|}(C_{g1}V_{g1}E_{C1} + C_{g2}V_{g2}E_{Cm})$$

(2.12)

$$\mu_2(N_1, N_2) = (N_2 - \frac{1}{2})E_{C2} + N_1 E_{Cm} - \frac{1}{|e|}(C_{g1}V_{g1}E_{Cm} + C_{g2}V_{g2}E_{C2}).$$

(2.13)

From the electrochemical potentials in Eqs. 2.12 and 2.13 we construct a charge stability diagram, giving the equilibrium potentials $N_1$ and $N_2$ as a function of $V_{g1}$ and $V_{g2}$. We define the electrochemical potentials of the left and right leads to be zero if no bias voltage is applied, $\mu_L = \mu_R = 0$. Hence, the equilibrium charges on the dots are the largest values of $N_1$ and $N_2$ for which both $\mu_1(N_1, N_2)$ and $\mu_2(N_1, N_2)$ are less than zero. If either is larger than zero, electrons escape to the leads. This constraint, plus the fact that $N_1$ and $N_2$ must be integers, creates hexagonal domains in $(V_{g1}, V_{g2})$-phase space in which the charge configuration is stable.

For completely decoupled dots ($C_m = 0$) the diagram looks like as in Fig. 2.14a. The gate voltage $V_{g1(2)}$ changes the charge on dot 1(2), without affecting the charge on the other. If the coupling is increased, the domains become hexagonal (Fig. 2.14b). The vertices of the square domains have separated into 'triple-points'. When $C_m$ becomes the dominant capacitance ($C_m/C_{1(2)} \to 1$), the triple-point separation reaches its maximum (see Fig. 2.14c). The double dot behaves like one dot with charge $N_1 + N_2$.

In order to obtain a measurable current, the tunnel barriers need to be sufficiently transparent and at the same time the tunnelbarriers need to be sufficiently opaque to ensure a well defined electron number on each dot. For double dots
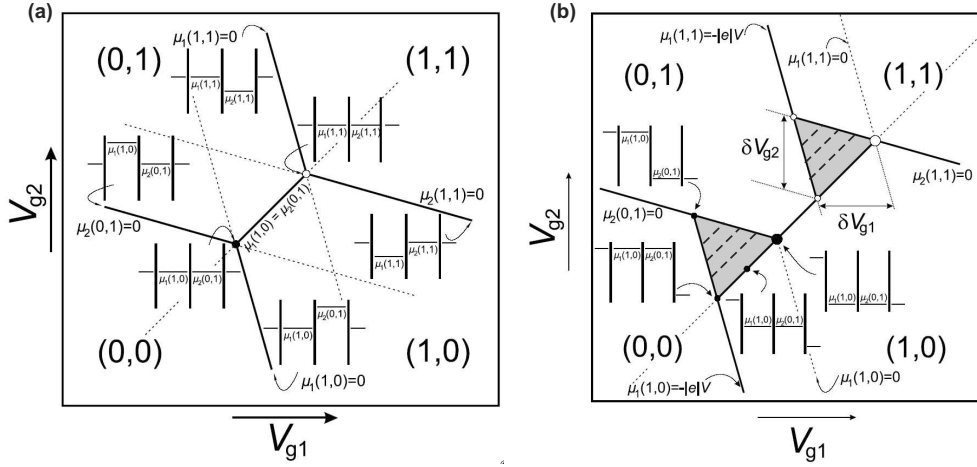
**Figure 2.15:** Zoom in of triple points in the linear **(a)** and **(b)** non-linear regime. In the non-linear regime the triple point become triangular regions whose boundaries are determined by the applied bias voltage. If the bias voltage is large enough, multiple discrete excited states can show up as lines inside the triangles.

coupled in series, a conductance resonance is found when electrons can tunnel through both dots. This condition is met whenever three charge states become degenerate, i.e. whenever three boundaries in the honeycomb diagram meet in one point (Fig. 2.15a).

In the non-linear regime the triple points develop into triangular regions. The conditions $-|e|V = \mu_L \geq \mu_1, \mu_1 \geq \mu_2$, and $\mu_2 \geq \mu_R = 0$ determine the boundaries of the triangles. In Fig. 2.15b the triple points in the non-linear transport regime are shown. For sufficiently large bias voltage, multiple discrete energy levels can enter the bias window. In this case, not only ground states, but also excited states contribute to the conductance. The discrete levels manifest themselves as resonance lines within the conductance triangles (Fig. 2.15b).

## 2.5 Franck-Condon Model

So far we have only considered excitations arising from the electronic structure and quantum confinement in quantum dot systems. In chapter 7 of this thesis we have performed measurements on suspended nanotubes and found that the vibrations of the nanotube quantum dot can give rise to excitations. In this section we would like to give a brief introduction about this observation by extending the Coulomb blockade theory to accommodate vibrational degrees of freedom of a quantum dot. In general, the current going through a single level of a quantum dot is simply $e\Gamma$, where $\Gamma$ is the total tunnelrate. When vibrations can play a

role, we have to take into account the vibrational part of the wavefunctions. Since the typical electronic velocities are much larger than those of the nuclei we can use the Born-Oppenheimer approximation to decouple the motion of the electrons and the nuclei. Due to the vibrations the tunnel rates will be modified to $\Gamma_{S(D)}|\langle\psi_f|\psi_i\rangle|^2$, where $\psi_i$ and $\psi_f$ are the vibrational wavefunctions of the quantum dot before and after the electron tunneling. When there is no vibrational degree of freedom the overlap is equal to one.

If we approximate the vibrating quantum dot as a harmonic oscillator (Fig. 2.16a) we can simply calculate the overlap between the ground and vibrationally excited state to yield [23] the Franck-Condon factors

$$P_{n0} = |\langle\psi_n(x - l)|\psi_0\rangle|^2 = \frac{g^n}{n!}e^{-g}, \tag{2.14}$$

where $g = \frac{1}{2}\left(\frac{l}{l_0}\right)^2$ is an important parameter which is proportional to the ratio between the classical and quantum displacement ($l_0 = 1/\sqrt{m_0\omega_0}$) of the harmonic oscillator. In Fig. 2.16b we show the effect of the Franck-Condon factors on the current through the quantum dot for different values of $g$.
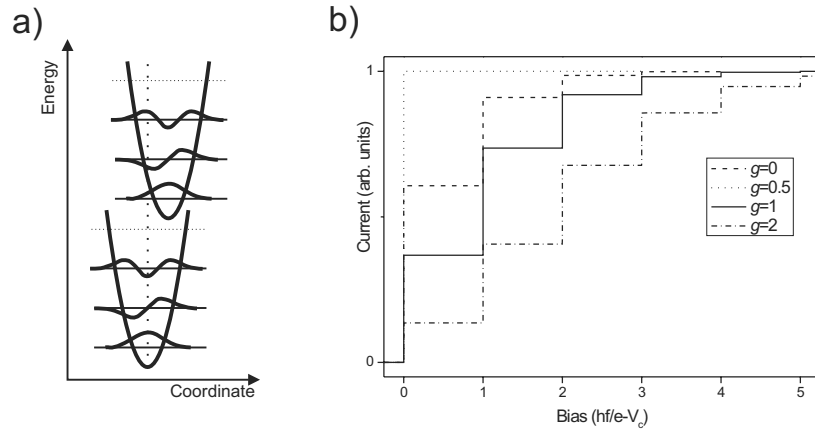


**Figure 2.16:** **(a)** Sketch of a harmonic potential together with the wavefunctions. The parabola are displaced when an electron tunnels on the dot. **(b)** Calculated $I - V$ curves at zero temperature for different values of the parameter $g$. The current increases in steps every time the bias is increased by $hf/e$. $V_c$ is the bias voltage required to overcome the Coulomb-blockade.

# References

[1] L.C. Venema, *Electronic structure of carbon nanotubes.* Ph.D. thesis, Delft University of Technology (1999).

[2] P. Jarillo-Herrero, *Quantum transport in carbon nanotubes.* Ph.D. thesis, Delft University of Technology (2005).

[3] J. W. Mintmire, B. I. Dunlap, and C. T. White, *Are Fullerene Tubules Metallic?* Phys. Rev. Lett. **68**, 631 (1992).

[4] N. Hamada, S. Sawada, and A. Oshiyama, *New One-Dimensional Conductors - Graphitic Microtubules.* Phys. Rev. Lett. **68**, 1579 (1992).

[5] R. Saito, M. Fujita, G. Dresselhaus, and M. S. Dresselhaus, *Electronic-Structure of Chiral Graphene Tubules.* Appl. Phys. Lett. **60**, 2204 (1992).

[6] P. R. Wallace, *The Band Theory of Graphite.* Phys. Rev. **71**, 622 (1947).

[7] E.D. Minot, *Tuning the bandstructure of carbon nanotubes.* Ph.D. thesis, Cornell University (2004).

[8] M. S. Dresselhaus, Dresselhaus, G., Avouris, Ph., *Carbon Nanotubes: Synthesis, Structure, Properties, and Applications* (Springer, New York, 2001).

[9] S. G. Lemay *et al.*, *Two-dimensional imaging of electronic wavefunctions in carbon nanotubes.* Nature (London) **412**, 617 (2001).

[10] E. D. Minot, Y. Yaish, V. Sazonova, and P. L. McEuen, *Determination of electron orbital magnetic moments in carbon nanotubes.* Nature (London) **428**, 536 (2004).

[11] J.M. Elzerman, *Electron spin and charge in semiconductor quantum dots.* Ph.D. thesis, Delft University of Technology (2004).

[12] Images are taken from: Single molecule: Cornell Center for Materials Research, Cornell University ; Metallic (superconducting) nanoparticle: M. M. Deshmukh, *et al.*, *Equilibrium and nonequilibrium electron tunneling via discrete quantum states.* Phys. Rev. B **65** (2002); Self-assembled QD; Vertical QD: Quantum Transport Group TU Delft; Lateral QD: L.P. Kouwenhoven *et al.*, Cover Physics Today January 1993; Nanowire: Kindly provided by J.A. van Dam; and Nanotube: image gallery Molecular Biophysics Group TU Delft.

[13] L.P. Kouwenhoven, C.M. Marcus, P.L. McEuen, S. Tarucha, R.M. Westervelt, & N.S. Wingreen, Electron transport in quantum dots, in *Mesoscopic Electron Transport*, edited by L.L. Sohn, L.P. Kouwenhoven, & G. Schön, (Kluwer, Series E **345**, 1997), p.105-214.

[14] D. V. Averin and Y. V. Nazarov, *Virtual Electron-Diffusion During Quantum Tunneling of the Electric Charge.* Phys. Rev. Lett. **65**, 2446 (1990).

[15] A. Javey, J. Guo, Q. Wang, M. Lundstrom, and H. Dai, *Ballistic carbon nanotube field-effect transistors.* Nature (London) **424**, 654 (2003).

[16] D. Mann, A. Javey, J. Kong, Q. Wang, and H. J. Dai, *Ballistic transport in metallic nanotubes with reliable Pd ohmic contacts.* Nano Lett. **3**, 1541 (2003).

[17] W. Kim *et al.*, *Electrical contacts to carbon nanotubes down to 1 nm in diameter.* Appl. Phys. Lett. **87**, 173101 (2005).

[18] S. J. Tans *et al.*, *Individual single-wall carbon nanotubes as quantum wires.* Nature (London) **386**, 474 (1997).

[19] M. Bockrath *et al.*, *Single-Electron Transport in Ropes of Carbon Nanotubes.* Science **275**, 1922 (1997).

[20] Y. Oreg, K. Byczuk, and B. I. Halperin, *Spin configurations of a carbon nanotube in a nonuniform external potential.* Phys. Rev. Lett. **85**, 365 (2000).

[21] W. G. van der Wiel *et al.*, *Electron transport through double quantum dots.* Rev. Mod. Phys. **75**, 1 (2003).

[22] D. Loss and D. P. DiVincenzo, *Quantum computation with quantum dots.* Phys. Rev. A **57**, 120 (1998).

[23] S. Braig and K. Flensberg, *Vibrational sidebands and dissipative tunneling in molecular transistors.* Phys. Rev. B **68**, 205324 (2003).

# Chapter 3

# Fabrication

The basis of a 'good' experiment in nanoscience is a 'good' sample. The fabrication of a 'good' sample is not always easy. Quite often the fabrication involves many steps. Some steps are easy and others are more difficult. However, all the steps are crucial. The steps involved for the fabrication process of nanotube devices can be divided into four or five main parts, depending on the required sample. These are: (i) fabrication of markers; (ii) nanotube deposition/growth; (iii) locate nanotubes with respect to markers and fabricate electrodes; (iv) if needed, fabricate Al gates and SETs, and (v) room temperature characterization and bonding. Below we will go into more detail for each fabrication part.

## *Fabrication of markers*

In all experiments the nanotubes are grown/deposited on top of oxidized silicon substrates. The Si-substrates are highly doped (p-doped in our case) so that they remain conductive at low temperatures and can serve as a backgate in our devices. The thickness of the thermally grown oxide is typically $\sim$250 nm, and isolates the devices from the back gate. A set of markers is necessary to later locate the position of the nanotubes and for the fabrication of the electrodes. These include a set of electron beam lithography alignment markers (e-beam markers) and atomic force microscopy (AFM) markers. The patterning of these markers requires one e-beam lithography 'cycle' (Fig. 3.1), which consists of spinning a double layer of e-beam resist, e-beam lithography, development, metal evaporation and lift-off. The bottom layer of resist (poly-methyl methacrylate (PMMA) 350K 3% in chlorobencene) is thicker and more sensitive to e-beam radiation, serves as a spacer and ensures a proper lift-off. The top resist layer (PMMA 950K 2% in chlorobencene) is less sensitive and serves as the actual mask for metal evaporation. Once the resist is spun, a pattern is 'written' by irradiating
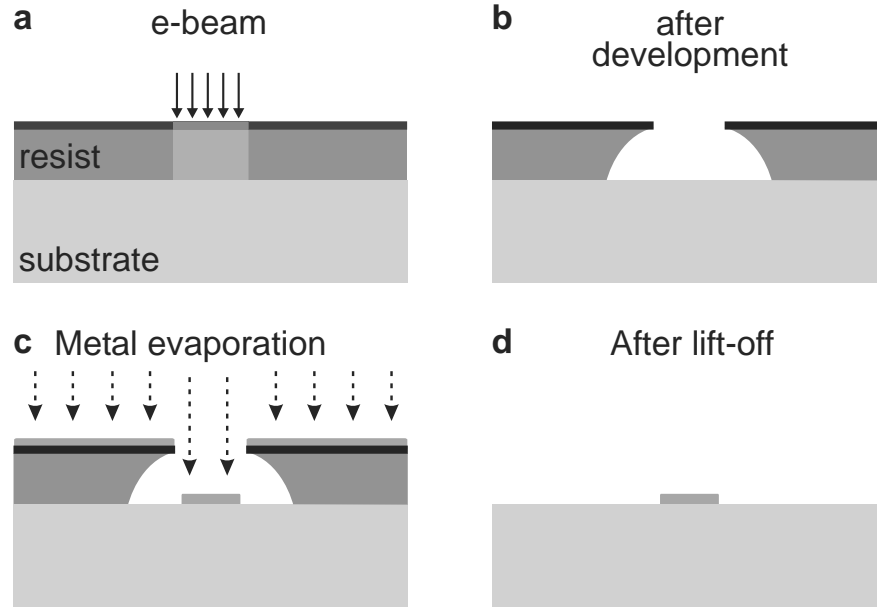
**Figure 3.1:** Schematic electron beam lithography cycle. **a**, Double layer of organic resist is spun on a substrate and a predesigned pattern is irradiated with a beam of electrons. **b**, After development, an opening is left in the resist. **c**, Metal is evaporated on top of the substrate + remaining resist. **d**, The remaining resist is removed and the metal is left at the predesigned positions.

the PMMA with a beam of electrons, which breaks the bonds in the polymer. The 'exposed' resist is removed from the substrate by immersing the sample in a developer (a 1:3 solution of methyl isobutyl ketone (MIBK) and iso-propyl alcohol (IPA)). Then the substrate is placed in an e-beam evaporator, where (Cr or Ti)/Pt (5/70 nm) is evaporated. Chromium or titanium are used as sticking layers for the platinum. We use Pt for the markers because they can withstand, without severe deformation, the high temperatures ($\sim$ 900 °C) during nanotube growth. After metal evaporation, the unexposed resist and excess metal is removed by immersing the sample in hot acetone ($\sim$ 55 °C). We have observed that further immersing the sample for $\sim$ 10 minutes in dichloroethane (DCE) helps removing small amounts of PMMA residue left during the lift-off process. After lift-off, we are left with a substrate which contains e-beam markers, AFM markers, as well as a series of optical and numerical markers to help handling and tagging of samples.

### Carbon nanotube deposition/growth

We have used two methods to place nanotubes on the substrates: direct de-

position from a solution, and chemical vapour deposition (CVD) growth. For the first one we put a small amount of carbon nanotube material in a bottle containing DCE and sonicate until the nanotube material has disentangled into separate nanotubes (typically $\sim 30$ min to 1 hour). Then a few droplets of solution are placed on a substrate and blown-dried with nitrogen. This process leaves nanotubes all over the substrate. It is easy and fast, but it has certain disadvantages, such as tuning the concentration of nanotubes, the fact that many times the nanotubes appear in ropes and not individually, and the random location in the deposition. Besides we have also noticed that it is harder to make good contact to deposited NTs than to CVD-grown tubes. For these reasons, most of our last experiments have been performed with carbon nanotubes grown by CVD. For the catalyst, 40 mg of $Fe(NO_3)_3 \cdot 9H_2O$, 2 mg of $MoO_2(acac)_2$ (Sigma Aldrich), and 30 mg of Alumina nanoparticles (Degussa Aluminum Oxide C) are mixed in 30 ml of methanol and sonicated for $\sim 1$ hr. The resulting liquid catalyst is deposited onto the substrate with 0.5 $\mu m^2$ openings in the PMMA resist (patterned on specific known locations by e-beam lithography) and blown dry. After lift-off in acetone, the substrate with patterned catalyst is placed in a 1-inch quartz tube furnace and the CVD is carried out at 900°C with 700 sccm $H_2$, 520 sccm $CH_4$ for 10 min. Argon is flown during heating up and cooling down. The methane and hydrogen flows have been optimized to obtain long and clean nanotubes ($\sim 10$ $\mu m$) without amorphous carbon deposition. After growth, typically a few tubes have grown from each catalyst site and, since the catalyst particles are patterned in known locations, the location of the nanotubes on the substrate is also known.

### Nanotube location and electrode fabrication

After the nanotube deposition/growth, the substrates are inspected by atomic force microscopy. All our devices have 'customized electrodes', i.e., we design electrodes individually for each nanotube device. While this requires a considerable amount of AFM time and design compared to, for example, depositing random grids of electrodes on the substrate, we find it very convenient in order to contact 'nice looking' individual nanotubes with a given diameter and length in between electrodes. We also typically choose straight segments of nanotubes (to prevent multiple quantum dot formation) located on 'residue-free' areas, to minimize switching behaviour. The AFM pictures determine the precise location of the nanotubes with respect to the predefined AFM markers. We design the electrodes on top of the desired NTs. A subsequent e-beam lithography step is carried out to write the electrodes and evaporate the metal. The contact metal
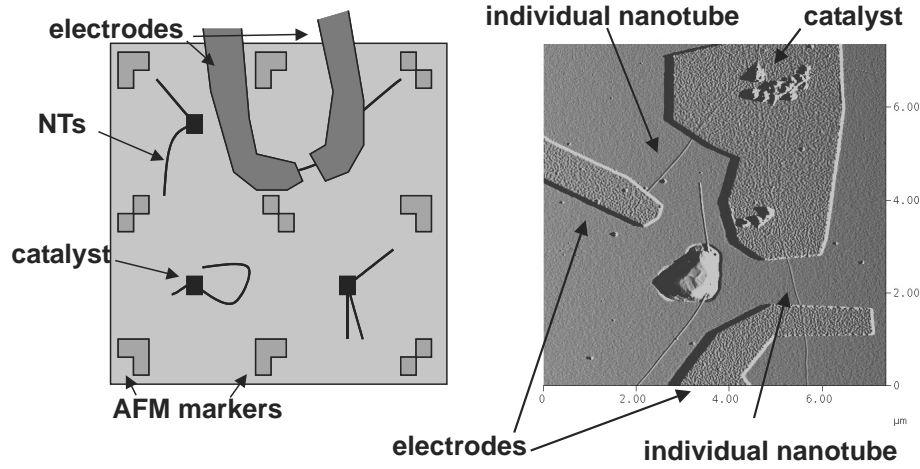
**Figure 3.2:** Fabrication process. Left: scheme of a substrate with the AFM markers, catalyst particles at predefined positions, grown nanotubes and designed electrodes. The separation between AFM markers is 6 $\mu$m. Right: Actual AFM picture of one of our devices.

can be Cr/Au, Ti/Au, Pd, Ti/Al, etc... depending on the type of experiment. After lift-off, the sample is ready for optical inspection and room temperature characterization. In some cases we etch part of the $SiO_2$ in order to suspend the nanotubes. This is done by immersing the samples in buffered HF for $\sim$ 1–2 min, transfer to water and followed by a gentle drying in hot IPA (to prevent the collapse of the nanotube due to surface tension effects).

### *Fabrication of gates and SETs*

So far we have only described the fabrication process for the 'standard' three terminal nanotube devices. For making more complex device architectures additional e-beam steps are required. In the following we describe the extra fabrication steps to make nanotube double quantum dots with tunable tunnel barriers defined by aluminium top-gates (see Fig. 3.3). The tunable tunnel barriers are the very narrow Al top-gates. The advantage of a narrow top-gate is that it controls the tunneling barrier on a local scale and only a small portion of the tube is covered with oxide. To fabricate nanotube double dot devices we first make Pd contacts to the tubes the same way as described above. Pd is used, because it introduces little or no barrier at the nanotube-metal contact [1, 2, 3]. In a subsequent electron beam lithography step we make the gate structures. First, we evaporate a 2 nm thin layer of Al and then this layer is completely oxidized for 10 min at 1 bar pure oxygen atmosphere. This step can be repeated to obtain
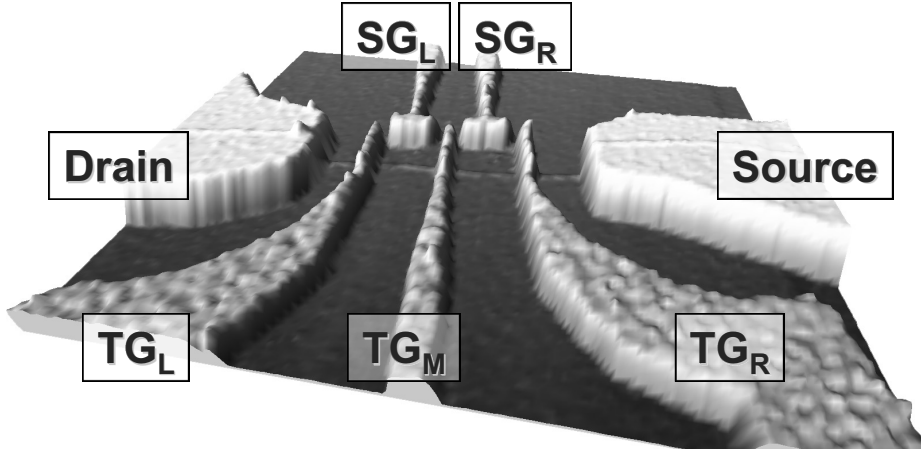
**Figure 3.3:** AFM picture of a carbon nanotube double quantum dot device. The contacts (source and drain) are made of Pd and the gate structures of Al. The top-gates (TG$_L$, TG$_M$, and TG$_R$) create tunable tunnelbarriers and the side-gates are used to change the electrochemical potential of the separate dots individually.

a thicker oxide. After oxidation the fabrication is continued with the evaporation of 35 nm of Al and followed by 15 nm of AuPd.

Recently, we have started to work on placing SETs close to NT devices. This work was inspired by the success with charge detection of our group members working on conventional 2-DEG QDs [4, 5]. They have used a quantum point contact (QPC) as a charge sensor [6] to measure the charge change of their dots when the transport currents are immeasurably small. We have chosen for a SET since it is one of the most sensitive electrometer capable of reaching sensitivities of the order of $10^{-5}$ $e/\sqrt{\text{Hz}}$ [7] and can be $\sim$ easily fabricated on the substrates (Si on SiO$_2$) we use with the equipment we have at our disposal (evaporator with a rotatable stage and controlled oxidation possibility).

We fabricate the junctions, which connect the SET island with the leads using a method called shadow evaporation [8]. We spin two layer resist onto the substrate. First layer is PMMA 350K with a thickness of 160 nm and the second layer is PMMA 950K with 90 nm thickness. After exposure (Fig.3.4a) and development (Fig.3.4b) in a 1:3 mixture of MIBK and IPA for 2.5 min (Fig.3.4b) a larger area of the first layer than the second layer is removed due to the back-scattered electrons and the different electron sensitivity of the materials. This leads to a undercut and at certain places to a free hanging bridge which is needed for the shadow evaporation. After defining the mask, the sample is mounted on a rotatable sample holder. Under an angle of 15° we evaporate a 30 nm layer of Al (Fig.3.4c). By exposing the Al to a controlled pressure of pure oxygen a thin layer
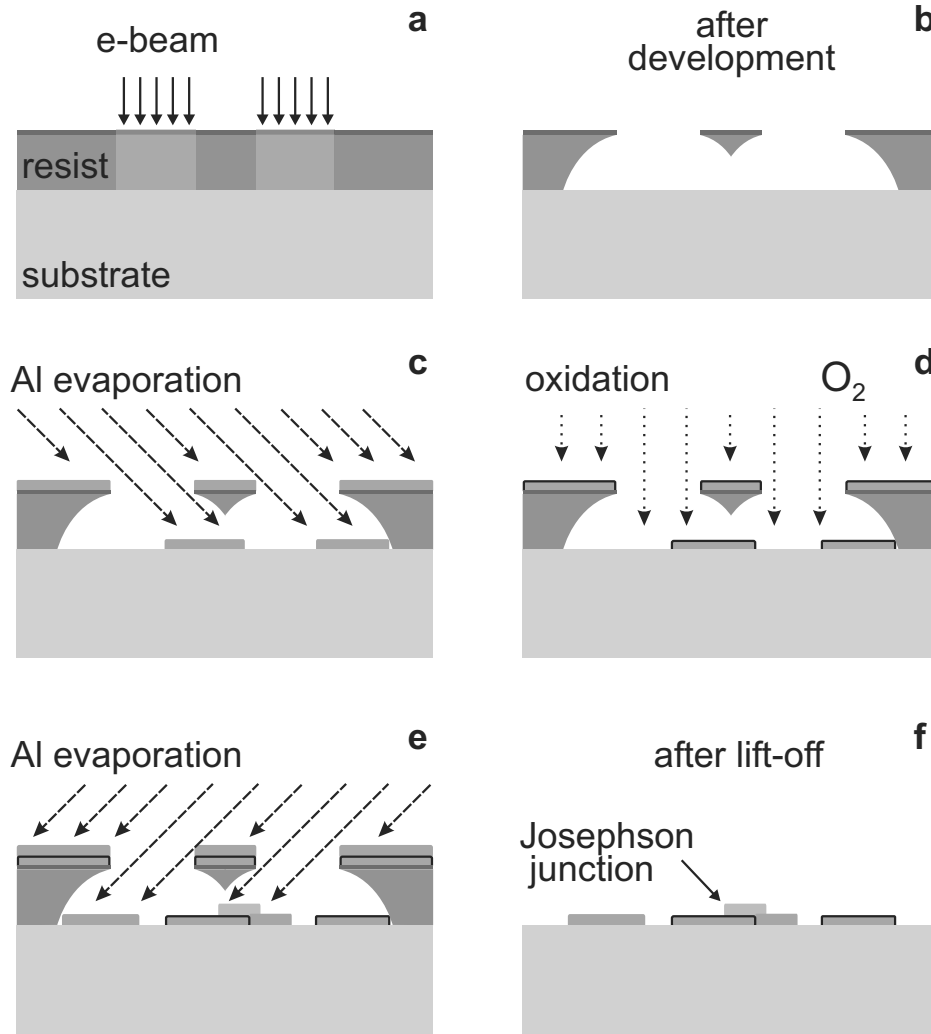
**Figure 3.4:** Schematic overview for the fabrication of a SET. Reproduced from ref.[9]

of Al$_2$O$_3$ is formed (Fig.3.4d). In a subsequent evaporation step 45 nm of Al is evaporated under an angle of -15°. We remove the remaining resist layers and the Al on top by immersing the sample in Acetone (Fig.3.4f). We are left with a small overlap area of the Al layers with a very thin Al$_2$O$_3$ layer in between which should act as the tunnel barrier. In Fig. 3.5 we show measurements performed on a SET.

### Room temperature test and sample bonding

The devices are characterized electrically in a room temperature probe station, where the conductance is measured versus gate voltage to determine if the tubes are semiconducting or metallic and also how good is the contact to the

**Figure 3.5:** Stability diagrams ($\mathrm{d}I/\mathrm{d}V$) of a SET in the **(a)** superconducting state and **(b)** normal state ($B = 1$ T). In **(a)** clear features of quasi-particle tunneling [10] are seen. By applying a magnetic field, we destroy superconductivity and are left with regular coulomb diamonds in **(b)**.

nanotubes. After that, the chip is glued on a chip carrier and some selected devices are bonded. The sample is ready to be connected to the low temperature measurement setup.
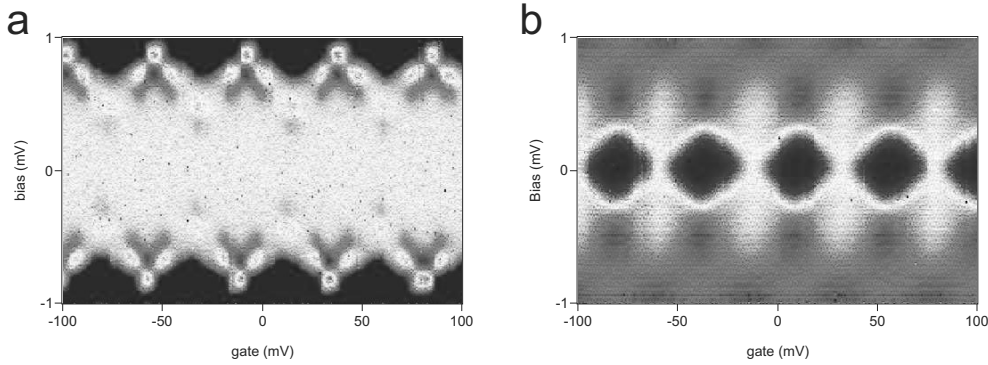
# References

[1] A. Javey, J. Guo, Q. Wang, M. Lundstrom, and H. Dai, *Ballistic carbon nanotube field-effect transistors.* Nature (London) **424**, 654 (2003).

[2] D. Mann, A. Javey, J. Kong, Q. Wang, and H. J. Dai, *Ballistic transport in metallic nanotubes with reliable Pd ohmic contacts.* Nano Lett. **3**, 1541 (2003).

[3] W. Kim *et al.*, *Electrical contacts to carbon nanotubes down to 1 nm in diameter.* Appl. Phys. Lett. **87**, 173101 (2005).

[4] J. M. Elzerman *et al.*, *Single-shot read-out of an individual electron spin in a quantum dot.* Nature (London) **430**, 431 (2004).

[5] R. Hanson *et al.*, *Single-shot readout of electron spin states in a quantum dot using spin-dependent tunnel rates.* Phys. Rev. Lett. **94**, 196802 (2005).

[6] J. M. Elzerman *et al.*, *Few-electron quantum dot circuit with integrated charge read out.* Phys. Rev. B **67**, 161308 (2003).

[7] M. H. Devoret and R. J. Schoelkopf, *Amplifying quantum signals with the single-electron transistor.* Nature (London) **406**, 1039 (2000).

[8] G. J. Dolan, *Offset masks for lift-off photoprocessing.* Appl. Phys. Lett. **31**, 337 (1977).

[9] G. E. Onac, *High frequency noise detection in mesoscopic devices.* Ph.D. thesis, Delft University of Technology (2005).

[10] P. Hadley, E. Delvigne, E. H. Visscher, S. Lahteenmaki, and J. E. Mooij, *3e tunneling processes in a superconducting single-electron tunneling transistor.* Phys. Rev. B **58**, 15317 (1998).

# Chapter 4

# Electron-hole symmetry in a semiconducting carbon nanotube quantum dot

P. Jarillo-Herrero, S. Sapmaz,
C. Dekker, L. P. Kouwenhoven, and H. S. J. van der Zant

Optical and electronic phenomena in solids arise from the behaviour of electrons and holes (unoccupied states in a filled electron sea). Electron-hole symmetry can often be invoked as a simplifying description, which states that electrons with energy above the Fermi sea behave the same as holes below the Fermi energy. In semiconductors, however, electron-hole symmetry is generally absent since the energy band structure of the conduction band differs from the valence band [1]. Here we report on measurements of the discrete, quantized-energy spectrum of electrons and holes in a semiconducting carbon nanotube [2]. Through a gate, an individual nanotube is filled controllably with a precise number of either electrons or holes, starting from one. The discrete excitation spectrum for a nanotube with $N$ holes is strikingly similar to the corresponding spectrum for $N$ electrons. This observation of near perfect electron-hole symmetry [3] demonstrates for the first time that a semiconducting nanotube can be free of charged impurities, even in the limit of few-electrons or holes. We furthermore find an anomalously small Zeeman spin splitting and an excitation spectrum indicating strong electron-electron interactions.

---

## 4.1   Introduction

Carbon nanotubes can be metallic or semiconducting depending on their chirality. Electron transport through individual nanotubes has been studied for both classes [2]. Nanotubes of finite length have a discrete energy spectrum. Analogous to studies on semiconducting quantum dots, these discrete states can be filled with electrons, one by one, by means of a voltage applied to a nearby gate electrode [4]. Whereas metallic nanotubes have shown clean quantum dot (QD) behaviour [5, 6, 7], this has not been achieved in semiconducting single wall nanotubes (SWNTs). Theory indicates that semiconducting tubes are more susceptible to disorder than metallic ones [8, 9]. Disorder typically divides a semiconducting nanotube into multiple islands preventing the formation of a single, well-defined QD. Consequently, the electronic spectrum of semiconducting SWNTs has not been resolved before.

We report here on clean semiconducting tubes and focus on the regime of a few charge carriers (electrons or holes). We use high-purity carbon nanotubes (HiPco [10]), which are deposited with low density on a doped Si substrate (serving as a backgate) that has an insulating $SiO_2$ top layer [11, 12]. Individual nanotubes are electrically contacted with source and drain electrodes (50 nm Au on 5 nm Cr). We then suspend the nanotubes by etching away part of the $SiO_2$ surface [12]. We generally find that removing the nearby oxide reduces the amount of potential fluctuations (i.e. disorder) in the nanotubes, as deduced from transport characteristics.

## 4.2   A few electron-hole quantum dot

In this paper we focus on one particular semiconducting device that shows regular single QD behaviour for both few-hole and few-electron doping. The distance between the electrodes in this device is 270 nm (Fig. 4.1a). The dependence of the linear conductance on gate voltage shown in Fig. 4.1c is typical for semiconducting p and n-type behaviour [13, 14]. A low-temperature measurement around zero gate voltage (Fig. 4.1d) shows a large zero-current gap of about 300 meV in bias voltage, reflecting the semiconducting character of this nanotube. The zigzag pattern outside the semiconducting gap is due to Coulomb blockade [4]. These Coulomb blockade features are more evident in Fig. 4.1e, where a high-resolution measurement of the differential conductance shows the semiconducting gap with the first two adjacent Coulomb blockade diamonds.

The identification of the Coulomb diamonds for the first electron and first hole allows for an unambiguous determination of the particle number as we continue
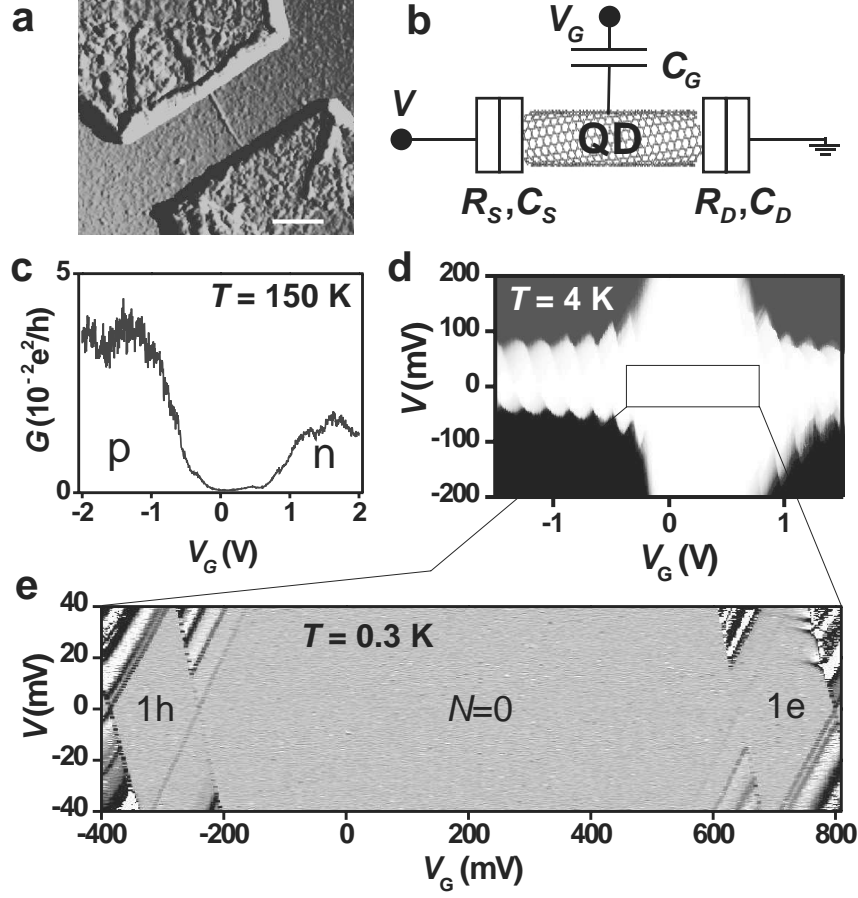
**Figure 4.1:** Sample and characterization. **(a)** Atomic force microscope image of the device before suspension (scale bar, 200 nm). **(b)** Device scheme: The nanotube QD is connected to source and drain electrodes via tunnel barriers characterized by resistances $R_S$, $R_D$ and capacitances $C_S$, $C_D$. The backgate is represented by a capacitor $C_G$. The dc source-drain current, $I$, is recorded in the measurements as a function of source-drain voltage $V$ and gate voltage $V_G$. Current-voltage ($I-V$) characteristics are numerically differentiated to obtain the differential conductance, $dI/dV$. **(c)** Linear conductance, $G$, as a function of gate voltage, $V_G$, at a temperature, $T \sim 150$ K showing the p and n conducting regions separated by the semiconducting gap. **(d)** Large-scale plot of the current (white is zero and dark is finite current) versus both $V$ and $V_G$ at $T = 4$ K. **(e)** High-resolution measurement of the differential conductance as a function of $V$ and $V_G$ in the central region of **(d)** at 0.3 K. Between $V_G \sim$ -250 and 650 mV, the nanotube QD is depleted entirely from mobile charge carriers. As $V_G$ increases (decreases), one electron (hole) enters the dot as indicated in the right (left) Coulomb diamond.

to fill the QD by further changing the gate voltage. Figure 4.2a shows the filling of holes, one by one, up to 20 holes. The region for the first 2 holes is enlarged
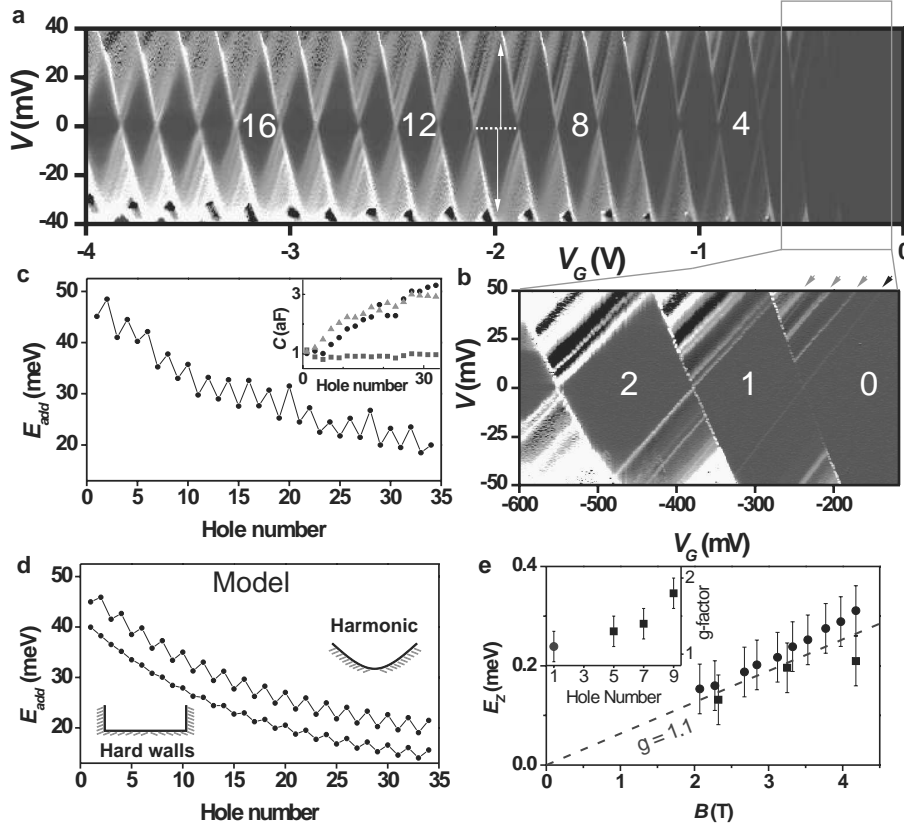
**Figure 4.2:** Few-hole semiconducting nanotube. **(a)** Two-dimensional colour plot of $dI/dV$, vs. $V$ and $V_G$ at $T = 4$ K (black is zero, white is $3\mu$S). In the black diamond-shaped regions the number of holes, $N$, is fixed by Coulomb blockade. **(b)** Zoom in taken at 0.3 K of the region with 0, 1, and 2 holes (white represents $dI/dV > 10$ nS). Lines outside the diamonds running parallel to the edges correspond to discrete energy excitations. **(c)** Addition energy, $E_{add}$, vs. $N$. $E_{add}$ is deduced from the diamond size for positive and negative $V$ (i.e. half the sum of the arrows in **(a)**). Inset, the capacitances $C_S$, $C_D$ and $C_G$ vs. $N$. **(d)** Calculation of the addition energy spectrum for a semiconducting nanotube (as an example we have taken a zigzag (35,0), with $E_{gap} \sim 259$ meV, $m_{eff} = 0.037m_e$ [3]) for a harmonic potential (top) and a hard-wall potential (bottom). The parameters for the harmonic potential are: $V(x = \pm 135 \text{ nm}) = E_{gap}/2$ (see appendix). **(e)** Zeeman splitting energy, $E_Z$, vs. magnetic field, $B$, for the one hole orbital states. The data result from two different types of measurements: (i) individual gate voltage traces at fixed bias (circles) and (ii) stability diagrams (squares, see also appendix). Inset: $g$-factor as a function of $N$. The point for $N = 1$ is the average of the data in Fig.4.2e. The points for N = 5, 7 and 9 are obtained from co-tunneling (see appendix).

in Fig 4.2b. The regularity in the Coulomb diamonds indicates a nanotube that is free of disorder. A closer inspection shows that the size of the Coulomb diamonds varies periodically on a smooth background as the hole number increases (Fig. 4.2c). The alternating, even-odd pattern in this addition energy, $E_{add}$, reflects the subsequent filling of discrete orbital states with two holes of opposite spin [4].

## 4.3 Electron-hole symmetry

We first focus on the additional discrete lines outside the Coulomb diamonds running parallel to its edges, as for instance indicated by arrows in Fig. 4.2b. Whereas the upper-left edge of the $N$-hole diamond reflects the ground state energy of the $(N+1)$-hole, the extra lines located at higher voltages, $V$, represent the discrete excitation spectrum for $(N+1)$-holes [4]. The spacing in $V$ directly measures the energy separation between the excitations. Such discrete spectra were not obtained before for semiconducting nanotubes.

We now compare the excitation spectra for a particular hole (h) number with the same electron (e) number. The left and right columns in Fig. 4.3 show the spectra for, respectively, holes and electrons. The upper row compares the spectra for 1h and 1e. The arrows in Fig. 4.3a point at the first 3 excited states for a single hole. (Note that only lines with positive slopes are observed because of asymmetric tunnel barriers [4].) Arrows in Fig. 4.3b indicate the corresponding first 3 excitations for a single electron. (Figure 4.4 explains this correspondence.) Remarkably, we have simply mirror-imaged the arrows from the hole to the electron side without any adjustment of their spacing. We thus find that the 1h and 1e excitations occur at the same energy. Since one-particle systems are free from particle-particle interactions, this symmetry implies that the confinement potential for electrons is the same as for holes.

Electron-hole symmetry also survives interactions as demonstrated in the lower rows in Fig. 4.3. Again the arrows pointing at the hole excitations have simply been mirror-imaged to the electron side. Thus, we indeed find that the spectra for 2h and 2e and for 3h and 3e show virtually perfect electron-hole symmetry in the excitation spectra. From a closer look one can see that also the relative intensities of the excitation lines display electron-hole symmetry.

The quality of our data allows for a quantitative analysis. The addition energy is defined as the change in electrochemical potential when adding the $(N+1)$ charge to a QD containing already $N$ charges. The constant-interaction (CI) model [4] gives $E_{add} = U + \Delta E$, where $U = e^2/C$ is the charging energy ($C =$
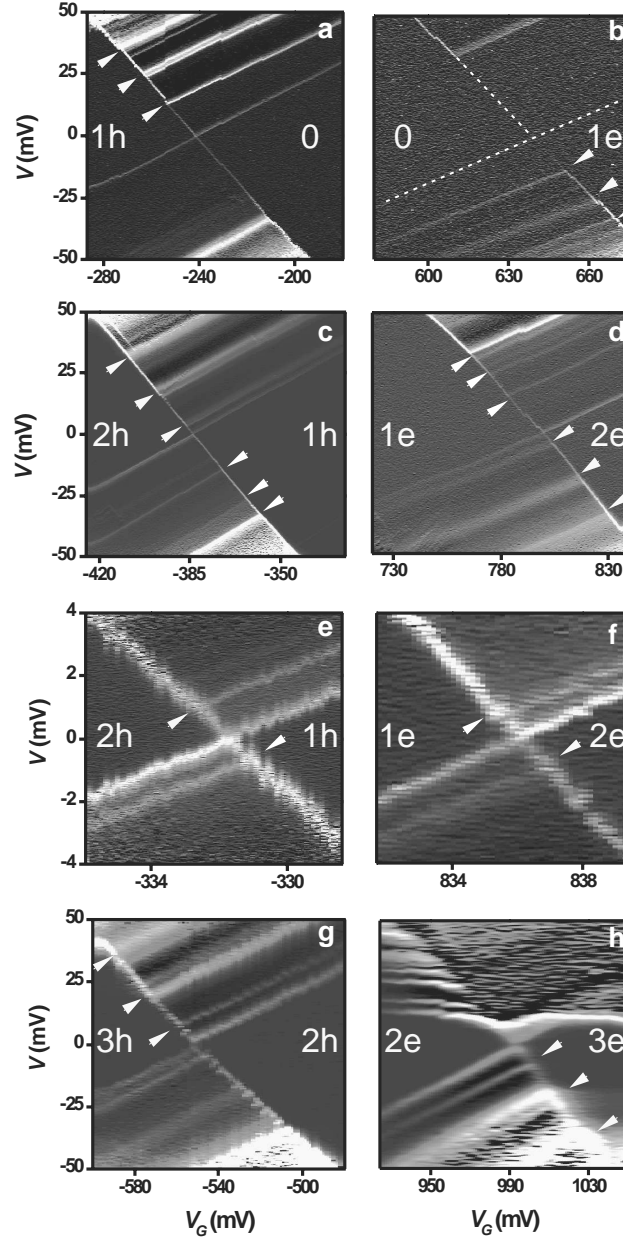
**Figure 4.3:** Excitation spectra for different electron and hole numbers demonstrating electron-hole symmetry. $dI/dV$ is plotted versus $(V, V_G)$ at $T = 0.3$ K. **(a)**, The transition from the 0 to 1h Coulomb diamonds. **(b)**, Corresponding transition from 0 to 1e. The white dotted lines in b are guides to the eye to indicate the diamond edge (not visible for this choice of contrast). **(c)** and **(d)**, same for 1-2h and 1-2e. **(e)** and **(f)**, Low-bias zoom in of the 1-2h and 1-2e crossings. **(g)** and **(h)**, Crossings corresponding to the 2-3h and 2-3e regions. (In **(h)**, the current switched between two stable positions for positive bias, with corresponding noise in $dI/dV$.)

$C_S + C_D + C_G$) and $\Delta E$ is the orbital energy difference between $N+1$ and $N$ particles on the QD. In the case of a semiconductor QD the addition energy for adding the first electron to the conduction band equals $U + E_{gap}$. From the observed gap size of 300 meV and $U \sim 50$ meV, we determine the semiconducting gap $E_{gap} \sim 250$ meV, which corresponds to a nanotube diameter of 2.7 nm [3]. AFM measurements, that usually underestimate the real height [15], indicate an apparent tube height of 1.70.5 nm.

Since two electrons with opposite spin can occupy a single orbital state, the CI model predicts an alternating value for $E_{add}$, where $E_{add} = U$ for $N =$ odd, and $E_{add} = U + \Delta E$ for $N =$ even. We indeed observe such an even-odd alternation in Fig. 4.2c with average $\Delta E \sim 4.3$ meV throughout the entire range of $N = 1$ to $N = 30$. Measurements of the Zeeman spin-splitting in a magnetic field (see appendix) confirm our assignment of even-odd particle number: Lines corresponding to ground states for odd $N$ split (i.e. total spin $=$ ), whereas even-$N$ lines do not split (i.e. total spin $= 0$). Figure 4.2e shows the value of the Zeeman energy for the one hole orbital states as a function of magnetic field. The data yield a reduced $g$-factor, $g \sim 1.1$, which is significantly lower than the value $g = 2$ reported on metallic nanotubes [5, 7]. (Some experiments on metallic nanotubes report deviations [16].) The reduction in $g$-factor disappears when adding holes. The inset shows that already for 9 holes the normal value is almost recovered. Lower $g$-factors are generally due to spin-orbit coupling, but this effect is small for carbon. It may hint at strong electron-electron interactions in the 1D-QD (see discussion below).

The addition energy spectrum indicates $\Delta E \sim 4.3$ meV for consecutive states as we fill the QD with holes. Previous spectra from metallic nanotubes have been analysed by considering a hard-wall potential in the nanotube, with an effective mass determined by the band structure. Our data show that this approach is not justified for semiconducting nanotubes. Lack of effective screening in 1D and the low number of mobile charges yield a gradual potential decay from the contacts [17]. We have computed the addition energy spectrum for a semiconducting nanotube whose gap is $\sim 250$ meV for two situations (Fig. 4.2d): hard-wall and harmonic potential of height $E_{gap}/2$ at the contacts [17]. For hard walls the level spacing increases slowly up to $\sim 1.9$ meV for $N = 34$. In the case of a harmonic potential, the level spacing is constant, as in the experiment, and equals 2.7 meV, in reasonable agreement with the experimental value $\sim 4.3$ meV (see also appendix ).

On top of the predicted even-odd pattern, there is a monotonic decrease of the average charging energy with $N$, implying that the total capacitance is changing. We have performed a detailed analysis of the QD electrostatics following ref. [18].

The result is given in the inset to Fig. 4.2c. It shows that the change in $C$ is mainly due to an increase in $C_S$ and $C_D$. This increase can be assigned to a decrease of the tunnel barrier widths as $|V_G|$ increases, consistent with the simultaneous increase of $dI/dV$ in Fig. 4.2a,b. Indeed, $dI/dV$ varies from $(5G\Omega)^{-1}$ in the first Coulomb peak to $(400k\Omega)^{-1}$ at large negative $V_G$.

The observation of electron-hole symmetry poses severe restrictions on the QD system: the effective masses for holes and electrons should be equal and the QD should be free of disorder. Scattering by negatively charged impurities, for example, is repulsive for electrons but attractive for holes, so it would break electron-hole symmetry. A symmetric band structure has been theoretically predicted for graphite materials and carbon nanotubes [3]. In contrast, the absence of scattering has come as a positive surprise.

Figure 4.4 clarifies the correspondence between the electron and hole excitation spectra. On the right side of Fig. 4.4b the situation for electrons is drawn (for $V_G > 0$) and on the left side for holes (for $V_G < 0$). The resulting excitations in transport characteristics as a function of $V$ and $V_G$ then lead to spectra as sketched in Fig. 4.4c and as measured in Fig. 4.3.

A detailed analysis of the excitation spectrum requires calculations that are beyond the scope of this paper. The constant-interaction model provides the parameter range for more exact models. The change in orbital energy when adding a charge is given by $\Delta E \sim 4.3$ meV, independent of $N$. $\Delta E$ is the scale for the energy difference between single-particle states. Excitations of a smaller energy scale have to be related to interactions. The likely interactions in semiconducting nanotubes are (1) Exchange interaction between spins (e.g. spin = 1 triplet states gain energy from the exchange interaction). Note that we observe an even-odd pattern, which seems to exclude ground states with spins $> 1/2$. Excited states, however, can have spins $> 1/2$. (2) Electron-phonon interactions. The vibrational modes in a suspended nanotube also have a discrete spectrum, which can show up in the excitation spectra [19]. Note that vibrational modes do not affect the addition energy spectrum of the ground states. (3) Electron-electron interactions. The value for the interaction strength parameter $U/\Delta E \sim 10$. Such a large $U/\Delta E$ ratio points to the presence of phenomena that are not captured by the CI model. Luttinger liquid models developed for finite length metallic nanotubes are not applicable to our few particle nanotubes. A more appropriate starting point are the exact calculations for 1D QDs. In the few particle regime the charge carriers tend to localize and maximize their separation, thereby forming a Wigner crystal [20]. In such a Wigner state, the spectrum consists both of high-energy single particle excitations and collective excitations at low energy [21], similar as in our experiment. Detailed calculations beyond
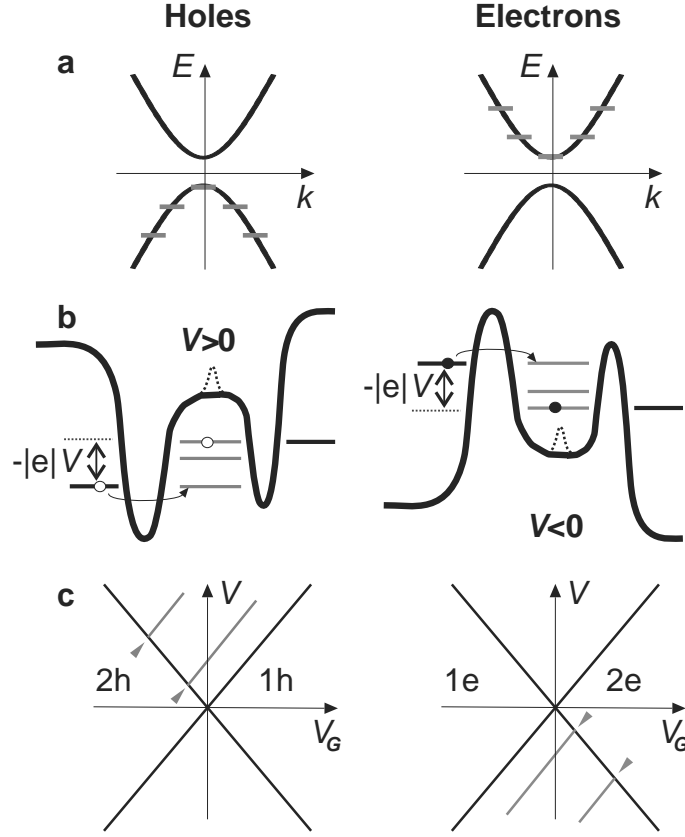
**Figure 4.4:** Electron-hole symmetry in semiconducting SWNTs. **(a)** Band structure (energy $E$ versus wave vector $k$) of a semiconducting nanotube illustrating symmetric valence and conduction bands. Due to quantum confinement, the carriers occupy a set of discrete energy states, shown on the left for hole doping and on the right for electron doping. **(b)** Schematic energy diagrams showing transport of holes (left) and electrons (right) across a QD. The levels for the ground state and two excited states for $N = 2$ are drawn. The distance between equivalent levels on the right and left is the same due to equal effective electron and hole masses. The top hole level is accessed from the left for $V > 0$, whereas the top electron level aligns with the left lead Fermi energy for $V < 0$. The dotted line in the potentials shows the effect of a negatively charged scatterer, which breaks electron-hole symmetry. **(c)**, Excitation spectra resulting from the energy diagrams in **(b)**. New levels entering the bias window due to excited states lead to lines in the $dI/dV$ plots that run parallel to the diamond edges. (Note that due to asymmetric barriers, only excitation lines with positive slope become visible.) These diagrams can be compared to the experiment in sec. 4.3.

the CI model and a comparison with the experimental results are necessary to establish the precise effect on transport from these interactions.

We thank R. E. Smalley and coworkers for providing the high-quality HiPco

# References

[1] N. W. Ashcroft and N. D. Mermin, *Solid State Physics.* (Saunders College, Orlando, 1976).

[2] C. Dekker, *Carbon nanotubes as molecular quantum wires.* Physics Today **52**, 22 (1999).

[3] M. S. Dresselhaus, Dresselhaus, G., Eklund, P. C., *Science of Fullerenes and Carbon Nanotubes.* (Academic Press, San Diego, 1996).

[4] L. P. Kouwenhoven, D. G. Austing, and S. Tarucha, *Few-electron quantum dots.* Rep. Prog. Phys. **64**, 701 (2001).

[5] S. J. Tans *et al.*, *Individual single-wall carbon nanotubes as quantum wires.* Nature (London) **386**, 474 (1997).

[6] M. Bockrath *et al.*, *Single-Electron Transport in Ropes of Carbon Nanotubes.* Science **275**, 1922 (1997).

[7] D. H. Cobden and J. Nygard, *Shell filling in closed single-wall carbon nanotube quantum dots.* Phys. Rev. Lett. **89**, 046803 (2002).

[8] T. Ando and T. Nakanishi, *Impurity scattering in carbon nanotubes - Absence of back scattering.* J. Phys. Soc. Jpn. **67**, 1704 (1998).

[9] P. L. McEuen, M. Bockrath, D. H. Cobden, Y. G. Yoon, and S. G. Louie, *Disorder, pseudospins, and backscattering in carbon nanotubes.* Phys. Rev. Lett. **83**, 5098 (1999).

[10] M. J. Bronikowski, P. A. Willis, D. T. Colbert, K. A. Smith, and R. E. Smalley, *Gas-phase production of carbon single-walled nanotubes from carbon monoxide via the HiPco process: A parametric study.* J. Vac. Sci. Technol. A **19**, 1800 (2001).

[11] M. S. Fuhrer *et al.*, *Crossed nanotube junctions.* Science **288**, 494 (2000).

[12] J. Nygård and D. H. Cobden, *Quantum dots in suspended single-wall carbon nanotubes.* Appl. Phys. Lett. **79**, 4216 (2001).

[13] A. Bachtold, P. Hadley, T. Nakanishi, and C. Dekker, *Logic circuits with carbon nanotube transistors.* Science **294**, 1317 (2001).

[14] J. Park and P. L. McEuen, *Formation of a p-type quantum dot at the end of an n-type carbon nanotube.* Appl. Phys. Lett. **79**, 1363 (2001).

[15] H. W. C. Postma, A. Sellmeijer, and C. Dekker, *Manipulation and imaging of individual single-walled carbon nanotubes with an atomic force microscope.* Adv. Mater. **12**, 1299 (2000).

[16] H. W. C. Postma, Z. Yao, and C. Dekker, *Electron addition and excitation spectra of individual single-wall carbon nanotubes.* J. Low Temp. Phys. **118**, 495 (2000).

[17] S. Heinze *et al.*, *Carbon nanotubes as Schottky barrier transistors.* Phys. Rev. Lett. **89**, 106801 (2002).

[18] H. Grabert and M. H. Devoret, *Single Charge Tunneling.* (eds. H. Grabert, and M. H. Devoret) (Plenum, New York, 1992).

[19] H. Park *et al.*, *Nanomechanical oscillations in a single-C-60 transistor.* Nature (London) **407**, 57 (2000).

[20] E. Wigner, *On the Interaction of Electrons in Metals.* Phys. Rev. **46**, 1002 (1934).

[21] W. Häusler and B. Kramer, *Interacting Electrons in a One-Dimensional Quantum-Dot.* Phys. Rev. B **47**, 16353 (1993).

[22] C. T. White and T. N. Todorov, *Carbon nanotubes as long ballistic conductors.* Nature (London) **393**, 240 (1998).

[23] A. Kogan *et al.*, *Measurements of Kondo and spin splitting in single-electron transistors.* Phys. Rev. Lett. **93**, 166602 (2004).

## 4.4   Appendix

This appendix contains additional discussion and data, and was published as Supplementary Information to the main text in the corresponding publication (see Chapter title's page).

### *Model calculations*

In the main text we show model calculations of the addition energy, $E_{add}$, for two types of electrostatic potential in the nanotube: hard-wall versus a parabolic
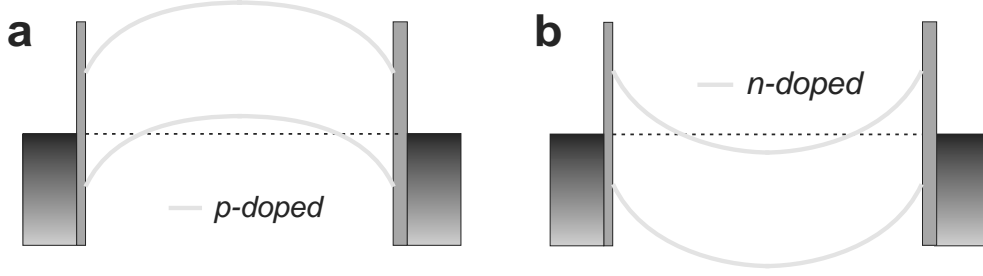
**Figure 4.5:** Band diagram scheme in the nanotube for negative **(a)** and positive **(b)** gate voltage.

potential (Fig. 4.2d). In both cases, we assume a zigzag $(n, m) = (0,35)$ nanotube (taken such that the theoretical band gap, $E_{gap} \sim 259$ meV, is close to the experimental value $E_{gap} \sim 250$ mV). From the band structure of this nanotube we obtain $m_{eff} \sim 0.037 m_e$ (ref. [3] main text). The effective mass, $m_{eff}$, is an important parameter for the value of the level spacing. We note that $m_{eff}$ is the same for a given semiconducting gap and approximately independent of chirality. In the case of a hard-wall potential, the level spacing is given by $\Delta E_n = E_n - E_{n-1} = h^2 \pi^2 (2n - 1)/2m_{eff}L^2$, where $L$ is the length of the nanotube. This value of $\Delta E_n$ increases with $n$, which is not observed in the data. In contrast, for a harmonic potential, the level spacing is constant, and equal to $\hbar \omega_o$. We determine $\hbar \omega_o$ by requiring the potential height at the nanotube edges to be equal to half the band gap, $E_{gap}/2 = 1/2 m_{eff} \omega_o^2 (L/2)^2$. The important point is that the potential is gradually decaying into the nanotube (ref. [17] main text, see Fig. 4.5 for a scheme of the band diagram in the nanotube for both negative and positive gate voltages). We find that only experimentally determined parameters ($E_{gap}$ and $L$) enter the model calculations. To simulate the monotonic decrease of the charging energy with $N$, we have fitted the odd values of the addition energy $[E_{add}(N_{odd}) = U]$. Then $E_{add}(N + 1) = U(N + 1) + \Delta E_n$, with $(N + 1) =$ even. We note that we keep the harmonic potential constant as we fill the QD with holes. Screening will start to play a role as we add more and more charges to the nanotube and will gradually change the harmonic potential into a hard-wall potential. Moreover, in the calculations we have included spin degeneracy for each orbital state and an extra factor of 2 to account for the two 1D modes in the nanotube.

### Scattering and disorder

Here we show additional data from another semiconducting device which

shows regular quantum dot behaviour and where the discrete spectrum can be discerned. We discuss also the importance of disorder. The symmetry in the electron-hole excitation spectrum (Fig. 4.3) shows that there is absence of significant charged scatterers in the device as discussed in the main text. This is especially important since semiconducting nanotubes are much more sensitive to disorder than metallic ones. It should also be noted that the diameter of the nanotube described in the main text is rather large. It is known that large diameter nanotubes are less sensitive to disorder than small diameter ones [22]. For comparison, we show additional data corresponding to a CVD-grown, non-suspended semiconducting nanotube. The estimated band gap is $\sim 800$ meV (corresponding to $\sim 1$ nm diameter). Fig. 4.6a shows the few-hole Coulomb diamonds (the current is plotted in log-color scale) in the $p$-doped region at $T = 4$ K, next to the semiconducting gap. The number of holes could not be exactly determined. For $N \geq 6 - 8$ the nanotube exhibits single quantum dot behaviour. However, the pattern becomes irregular as the quantum dot is near full depletion. This is a general feature of most of the studied semiconducting devices. We believe that as the QD is depleted, the holes or electrons tend to localize due to a lack of screening of the disorder potential, consequently forming multiple islands. Fig. 4.6, b and c, show Coulomb diamonds (differential conductance) deep in the $p$-side ($N_h \sim 100$) and in the $n$-side ($N_e \sim 40$) at $T = 300$ mK for the same device
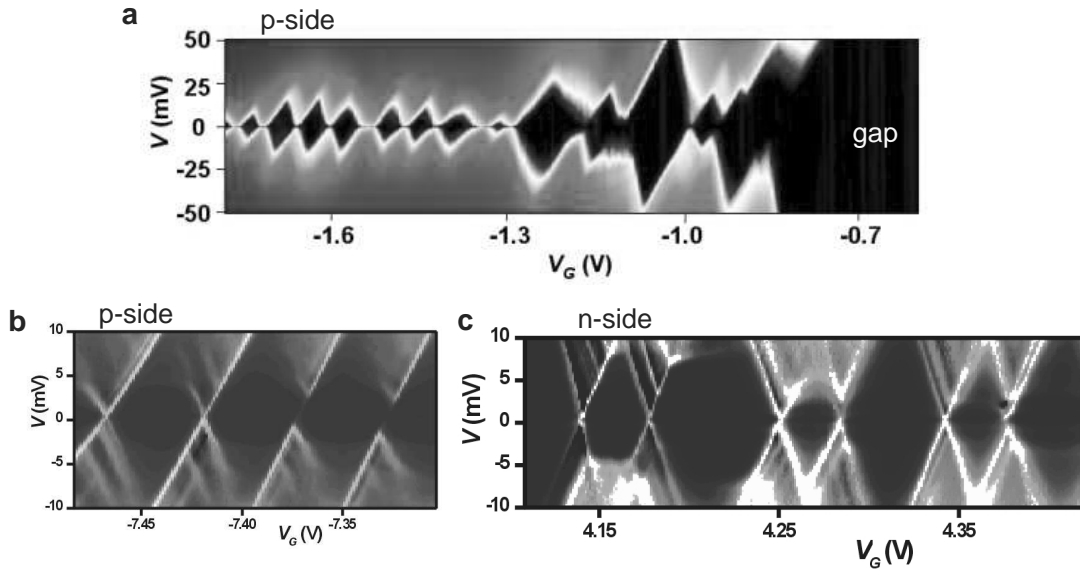


**Figure 4.6:** Differential conductance plot for a different semiconducting nanotube device. **(a)** Few hole regime. **(b)** Large hole number regime. **(c)** High electron number regime.
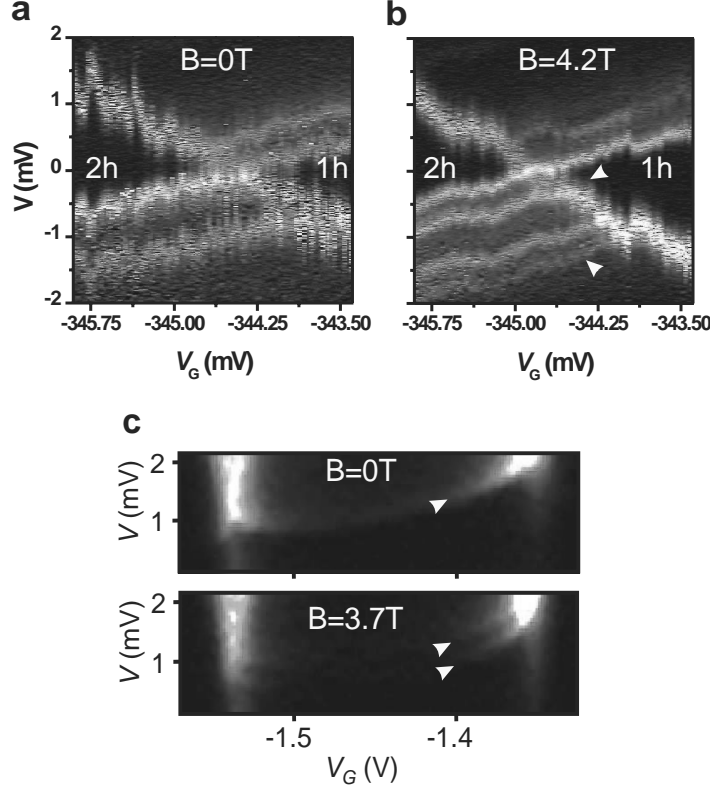
**Figure 4.7:** Zeeman splitting in a magnetic field $B$. **(a)** Color-scale differential con-
ductance plot in the 1-2 electron region at zero field. **(b)** Same as **(a)** but at $B = 4.2$
T. **(c)** Zeeman splitting in the inelastic cotunneling regime.

in a different cool down. The discrete spectrum is very clearly visible. We can
conclude, then, that single QD behaviour can be observed in semiconducting nan-
otubes both in the few-charge carrier regime (main text) and in the regime with
many particles (Fig. 4.6, b and c). In order to study clean nanotubes in the few
charge-carriers regime, it may be important to select large diameter nanotubes.
We have observed in other (metallic) samples that also suspending the nanotubes
yields in general more stable devices. This seems to be an advantage also in the
case of semiconducting nanotubes.

### Zeeman splitting

We show here $dI/dV$ versus $(V, V_G)$ at low energies in the 1-2 holes region

at zero (Fig. 4.7a) and finite (Fig. 4.7b) magnetic field, showing the Zeeman splitting for $N = 1$. For $N = 2$ no Zeeman splitting is observed, as expected. We have performed an analysis of the inelastic cotunneling data (raw data shown in Fig. 4.7c) in a magnetic field [23], from which we obtain the $g$-factor as we increase the number of holes. (Note that the Zeeman splitting can be observed only for $N_h$ = odd.) We have data for $N = 5, 7$ and 9, where the onset of inelastic-cotunneling is clearly observable. These are plotted in the inset to Fig. 4.2e.

# Chapter 5

# Electronic excitation spectrum of metallic carbon nanotubes

S. Sapmaz, P. Jarillo-Herrero, J. Kong,
C. Dekker, L. P. Kouwenhoven, and H. S. J. van der Zant

We have studied the discrete electronic spectrum of closed metallic nanotube quantum dots. At low temperatures, the stability diagrams show a very regular four-fold pattern that allows for the determination of the electron addition and excitation energies. The measured nanotube spectra are in excellent agreement with theoretical predictions based on the nanotube band structure. Our results permit the complete identification of the electron quantum states in nanotube quantum dots.

## 5.1  Introduction

Since their discovery [1] carbon nanotubes (NTs) have emerged as prototypical one-dimensional conductors [2]. At low temperatures, NT devices form quantum dots (QDs) where single-electron charging and level quantization effects dominate [3, 4]. A continuous improvement in device fabrication and NT quality has enabled the recent observation of two-electron periodicity in 'closed' QDs [5] and four-electron periodicity in 'open' single- and multi-wall NT QDs [6, 7]. Theoretically, the low-energy spectrum of single wall nanotube (SWNT) QDs has been modeled by Oreg *et al.*, [8]. Experiments on open NT QDs are compatible with this model, but the presence of the Kondo effect and broadening of the energy levels prevents the observation of the full spectrum [9]. An analysis of the electronic excitations is therefore still lacking.

The two-fold degenerate, low-energy band structure of a metallic SWNT is schematically shown in Fig. 5.1a. Quantization along the nanotube axis leads to a set of single particle states that are equally spaced because of the linear dispersion relation [10]. The combination of the two bands and the spin yields a four-fold periodicity in the electron addition energy. The simplest model to describe QDs is the Constant Interaction (CI) model [11], which assumes that the charging energy is constant and independent of the occupied single particle states. To describe NT QDs the CI-model has been extended [8] to include five independent parameters: the charging energy $E_C$, the quantum energy level separation $\Delta$, the subband mismatch $\delta$ (see Fig. 5.1a), the exchange energy $J$ and the excess Coulomb energy $dU$. Fig. 5.1c illustrates the meaning of the last two parameters. An independent verification of the Oreg model [8] requires the observation of the ground state addition energies and of, at least, two excited states. Such a study has not been reported.

Here we investigate the excitation spectrum of closed SWNT QDs. Not only the ground but also the complete excited state spectrum of these QDs has been measured by transport-spectroscopy experiments, enabling us to determine all five parameters independently. With these, the remaining measured excitation energies are well predicted leading to a complete understanding of the spectrum, without adjustable parameters.

## 5.2  Four-fold shell filling

HiPco [12] and CVD [13] grown NTs were used for the fabrication of the devices. HiPco tubes were dispersed from a dichloroethane solution on an oxidized, *p*-doped Si substrate. The CVD nanotubes were grown from catalyst particles on
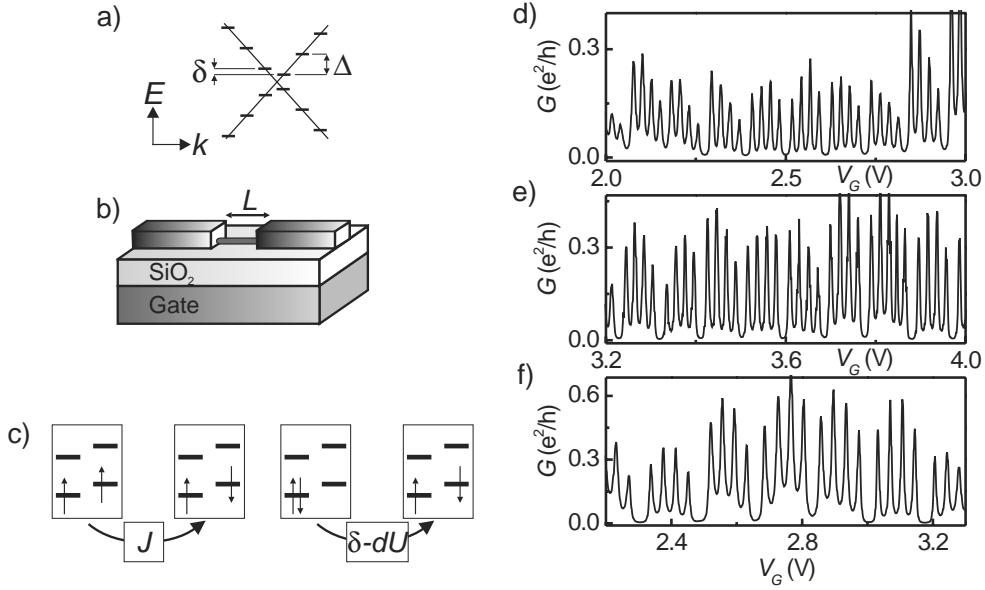
**Figure 5.1:** **(a)** Low-energy band structure of a metallic SWNT. In a finite length SWNT, the wave vector $k$ is quantized along the tube axis which leads to a set of quantized energy levels separated by $\Delta$ in each band. $\delta$ is the mismatch between the two bands. **(b)** Schematic diagram of the device geometry. **(c)** Meaning of $J$ (left) and $dU$ (right). The exchange energy favors spin alignment and $dU$ is the extra charging energy associated with placing two electrons in the same energy level. **(d)**, **(e)**, and **(f)** Conductance as a function of gate voltage in the linear response regime at 4 K for three different CVD grown samples. The NT lengths are 500, 680 and 760 nm, respectively.

predefined positions. Individual NTs were located by atomic force microscopy (AFM) with respect to predefined marker positions and electrodes were designed on top of straight segments of NTs. The highly doped silicon is used as a backgate to change the electrostatic potential of the NT QD (see Fig. 5.1b). We have fabricated NT devices with lengths in between contacts, $L$, varying from 100 nm to 1 $\mu$m.

Four-electron shell filling has been observed in over 15 samples. In some cases the four-fold pattern extended over more than 60 electrons added to the QD. Figs. 5.1d-f show representative examples of Coulomb Blockade (CB) oscillations [14] in the linear response regime. Clearly, the Coulomb peaks are grouped in sets of four reflecting the two-fold character of the NT bandstructure.

In the following, we focus on three different devices exhibiting similar four-fold periodicity in CB oscillations. These samples (A, B and C) had high enough contact resistances so that not only the electron ground states but also their excited states could be resolved. Together they provide enough information to

determine all the parameters in the model. We discuss the results of these three samples separately.

## 5.3   HiPCO nanotubes

*Sample A-* This device is made from a HiPco NT [12] with $L = 180$ nm and a diameter of 1.1 nm as determined by AFM. It is contacted by evaporating Cr/Au (5/75 nm) electrodes. Fig. 5.2a shows the current, $I$, as a function of source-drain bias voltage, $V$, and gate voltage, $V_G$. In the light-colored diamond-shaped regions, the current is blocked due to CB and the number of electrons is fixed. The clear four-fold periodicity makes it possible to assign the number of electrons in the last occupied shell. The sizes of the diamonds form an interesting pattern, namely a repetition of small/medium/small/big. This pattern is a consequence of the large subband mismatch compared to the exchange energy, as we show below.

The addition energy is defined as the change in electrochemical potential ($\Delta \mu_N$) when adding the $(N + 1)$ charge to a quantum dot already containing $N$ charges [11]. The addition energy is obtained by multiplying the diamond width, $\Delta V_G$, by a conversion factor, $\alpha$ ($\approx 0.017$), which relates the gate voltage scale to the electrochemical potential [14].

The Oreg-model yields the following equations for the addition energy of the $N$-th electron added [15]:

$$\Delta \mu_1 = \Delta \mu_3 = E_C + dU + J \tag{5.1}$$

$$\Delta \mu_2 = E_C + \delta - dU \tag{5.2}$$

$$\Delta \mu_4 = E_C + \Delta - \delta - dU. \tag{5.3}$$

To extract all five parameters, two more equations are needed. These are provided by the excitation spectrum. In Fig. 5.2c we show the numerical derivative of Fig. 5.2a (i.e., the differential conductance) for the first group of four. Excited states of the electrons are visible for all diamonds. The value of a particular excitation energy equals the bias voltage at the intersection between the excitation line and the Coulomb diamond edge (see Fig. 5.2c). The dotted arrows in diamond one and two in Fig. 5.2c correspond to the first excitation for one and two electrons extra on the NT QD respectively. The theoretical values of these two energies are

$$\Delta \mu_1^{\text{ex}} = \delta, \Delta \mu_2^{\text{ex}} = \delta - J - dU. \tag{5.4}$$
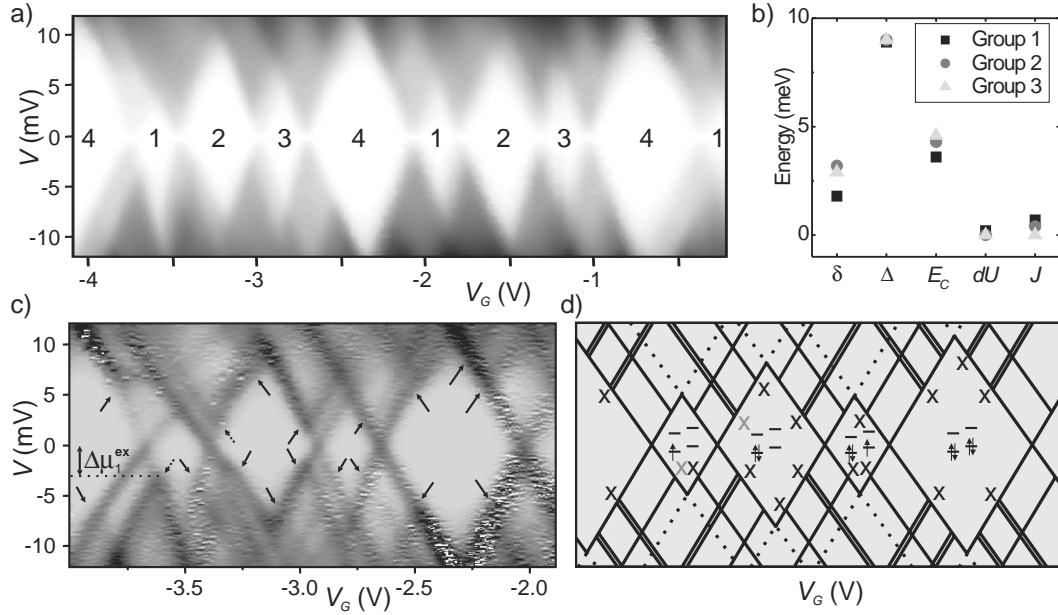
**Figure 5.2:** Sample A **(a)** Current as a function of $V$ and $V_G$ at $T = 300$ mK. Current goes from $-40$ nA to $+40$ nA. **(b)** Values of the parameters for three different groups of four (see text). **(c)** The differential conductance $(dI/dV)$ for the first group from **(a)**. Black is zero and bright is $>12$ $\mu$S. Lines running parallel to the diamond edges correspond to discrete energy excitations. The excitation energies corresponding to the dotted arrows have been used to deduce the model parameters. The predicted excitations are indicated by normal arrows. **(d)** Calculated spectrum for sample A. The black X's correspond to the normal arrows in **(c)** and grey X's corresponds to the dotted arrow. The diagrams indicate the ground state spin filling.

Equations (5.1)-(5.4) allow us to uniquely determine the five unknown parameters from the experimental data alone. We find $E_C = 4.3$ meV, $\Delta = 9.0$ meV, $\delta = 3.2$ meV, $J = 0.4$ meV and $dU \approx 0$ meV. The values of the parameters do not vary significantly between the different groups, as shown in Fig. 5.2b. The theoretically expected value for the level spacing is $\Delta = hv_F/2L$ [3]. With $v_F = 8.1 \cdot 10^5$ m/s [16] and $L = 180$ nm, we find 9.3 meV in excellent agreement with the experimental value.

Figure 5.2d shows the calculated spectrum of the NT QD using the parameters deduced from the experiment. Some excitations are split by the exchange energy. The stars in the calculated spectrum correspond to the arrows in the experimental data. The excitations denoted with gray X's were used for obtaining the parameters and correspond to the dotted arrows in Fig. 5.2c . The calculated spectrum resembles the measured one strikingly well.

## 5.4   CVD nanotubes

*Sample B-* This sample is CVD grown [13] with a diameter of 1.3 nm and $L = 500$ nm defined by Cr/Au contacts (5/40 nm). After contacting, the entire NT segment in between electrodes is suspended by etching away part of the $SiO_2$ [17]. We have measured the differential conductance, $dI/dV$, as a function of $V$ and $V_G$ at 300 mK (Fig. 5.3a). Again regular four-fold patterns are visible in the Coulomb diamonds.

The evolution of the Coulomb peaks as a function of the magnetic field (not shown here) gives information about the spin filling of the states [18]. We find that the filling is the same as sample A. Excited states of the QD are visible in all groups of four. The model parameters have been extracted using the same analysis as described above. The result is shown in Fig. 5.2b. The average values
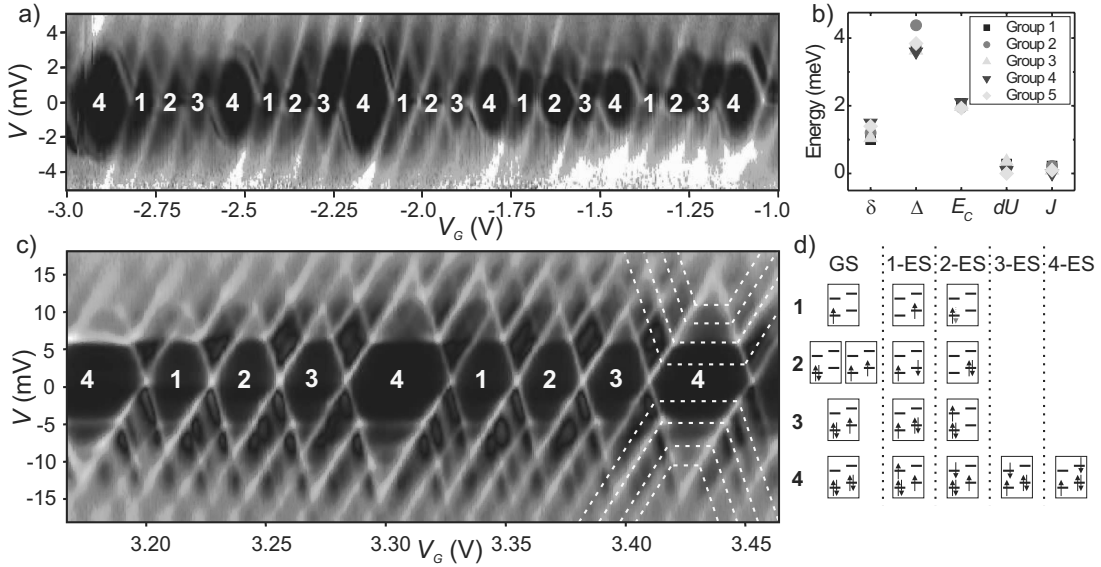


**Figure 5.3:** Differential Conductance of sample B **(a)** and C **(c)** as a function of $V$ and $V_G$ measured at 300 mK. Black represents $dI/dV \sim 0$, while lighter tones correspond to a higher conductance. Dashed lines in **(c)** indicate the excited states together with inelastic cotunneling. **(b)** Obtained parameters for sample B. **(d)** Electron quantum states of the NT QD. The numbers on the left denote the ground state (GS) number of electrons in the last occupied shell. The left column indicates the GS electron configuration (note that the two-electron GS is degenerate). Columns on the right denote the excited state (ES) configuration. Up to four ES are visible in the large Coulomb diamonds [22]. The dotted arrow in the second ES for one electron corresponds to an electron excited from the lower shell.

are $E_C = 2.0$ meV, $\delta = 1.2$ meV, $J = 0.1$ meV, $dU = 0.2$ meV and $\Delta = 3.0$ meV. The value of $\Delta$ corresponds to a length of 440 nm [3], in good agreement with the NT length between contacts. Furthermore, in all groups of four at least one more excitation remains for a comparison between theory and experiment. In all cases we find good agreement [19].

*Sample C-* This NT is CVD grown [13] with a diameter of 2.7 nm and $L = 750$ nm. The contacts are made by evaporating Ti/Au (20/40 nm). Fig. 5.3c shows $dI/dV$ as a function of $V$ and $V_G$. A very regular pattern of Coulomb diamonds with four-fold periodicity is displayed together with the excited states. In addition, up to three inelastic co-tunneling lines [20] are visible (horizontal lines inside the Coulomb diamonds in Fig. 5.3c).

The observation of three equally sized small diamonds and the fact that the excitations have the same energy for all four charge states indicate that $\delta \approx J + 2dU$. We find $E_C = 6.6$ meV, $\Delta = 8.7$ meV, $\delta \approx J = 2.9$ meV, and $dU \approx 0$ meV. Theoretically a level separation of 8.7 meV indicates a NT QD length of $\sim 200$ nm, while the distance between contacts is 750 nm. This may suggest that sample C consists of a QD with NT leads connecting it to the contacts. This is consistent with the large value for $E_C$. Remarkably, all the predicted excitation lines are present in the spectrum [21]. Therefore all the electron states can be assigned (Fig. 5.3d).

In summary, we have presented a complete analysis of the electronic spectrum in closed NT QDs. Samples with different lengths, production process (CVD and HiPco) and contact material all exhibit four-fold periodicity in the electron addition energy. The very regular Coulomb traces and stability diagrams enable the determination of the ground and excited state electron energies. Knowing precisely the spectrum of nanotube quantum dots is of fundamental importance in experiments involving the application of high frequency radiation such as photon-assisted tunneling and coherent control of the electron quantum states.

# References

[1] S. Iijima, *Helical Microtubules of Graphitic Carbon.* Nature (London) **354**, 56 (1991).

[2] For reviews, see C. Dekker, *Carbon nanotubes as molecular quantum wires.*

Physics Today **52**, No. 5, 22 (1999).; P. L. McEuen, *Single-wall carbon nanotubes.* Phys. World, June, 31 (2000).

[3] S. J. Tans *et al.*, *Individual single-wall carbon nanotubes as quantum wires.* Nature (London) **386**, 474 (1997).

[4] M. Bockrath *et al.*, *Single-Electron Transport in Ropes of Carbon Nanotubes.* Science **275**, 1922 (1997).

[5] D. H. Cobden and J. Nygård, *Shell filling in closed single-wall carbon nanotube quantum dots.* Phys. Rev. Lett. **89**, 046803 (2002).

[6] W. Liang, M. Bockrath, and H. Park, *Shell filling and exchange coupling in metallic single-walled carbon nanotubes.* Phys. Rev. Lett. **88**, 126801 (2002).

[7] M. R. Buitelaar, A. Bachtold, T. Nussbaumer, M. Iqbal, and C. Schönenberger, *Multiwall carbon nanotubes as quantum dots.* Phys. Rev. Lett. **88**, 156801 (2002).

[8] Y. Oreg, K. Byczuk, and B. I. Halperin, *Spin configurations of a carbon nanotube in a nonuniform external potential.* Phys. Rev. Lett. **85**, 365 (2000).

[9] The Kondo effect shifts the position of the Coulomb peaks towards each other. The level broadening smears out the excitation spectrum.

[10] M.S. Dresselhaus, G. Dresselhaus, P.C. Eklund, *Science of Fullerenes and Carbon Nanotubes* (Academic Press, San Diego, 1996).

[11] L. P. Kouwenhoven, D. G. Austing, and S. Tarucha, *Few-electron quantum dots.* Rep. Prog. Phys. **64**, 701 (2001).

[12] M. J. Bronikowski, P. A. Willis, D. T. Colbert, K. A. Smith, and R. E. Smalley, *Gas-phase production of carbon single-walled nanotubes from carbon monoxide via the HiPco process: A parametric study.* J. Vac. Sci. Technol. A **19**, 1800 (2001).

[13] J. Kong, H. T. Soh, A. M. Cassell, C. F. Quate, and H. J. Dai, *Synthesis of individual single-walled carbon nanotubes on patterned silicon wafers.* Nature (London) **395**, 878 (1998).

[14] H. Grabert and M.H. Devoret, *Single Charge Tunneling* (Plenum, New York, 1992).

[15] This set of equations corresponds to singlet ground state for $N = 2$. The triplet case is incompatible with experimental data.

[16] S. G. Lemay *et al.*, *Two-dimensional imaging of electronic wavefunctions in carbon nanotubes.* Nature (London) **412**, 617 (2001).

[17] J. Nygard and D. H. Cobden, *Quantum dots in suspended single-wall carbon nanotubes.* Appl. Phys. Lett. **79**, 4216 (2001).

[18] R. M. Potok *et al.*, *Spin and polarized current from Coulomb blockaded quantum dots.* Phys. Rev. Lett. **91**, 016802 (2003).

[19] The data show a very weak excitation around 200 $\mu$eV. The origin of this excitation might be vibrational [H. Park *et al.*, *Nanomechanical oscillations in a single-C-60 transistor.* Nature (London) **407**, 57 (2000).] corresponding to the first longitudinal mode in this suspended NT.

[20] S. De Franceschi *et al.*, *Electron cotunneling in a semiconductor quantum dot.* Phys. Rev. Lett. **86**, 878 (2001).

[21] The experimental value of $\Delta\mu$ for the large Coulomb diamond is $\sim$15% larger than deduced from the spectrum. The small Coulomb diamonds and the complete excitation spectrum is in perfect agreement with theory.

[22] There is more than one degenerate configuration for some of the excited states. For simplicity we only show one of them.

# Chapter 6

# Carbon nanotubes as nanoelectromechanical systems

S. Sapmaz, Ya. M. Blanter, L. Gurevich, and H.S.J. van der Zant

We theoretically study the interplay between electrical and mechanical properties of suspended, doubly clamped carbon nanotubes in which charging effects dominate. In this geometry, the capacitance between the nanotube and the gate(s) depends on the distance between them. This dependence modifies the usual Coulomb models and we show that it needs to be incorporated to capture the physics of the problem correctly. We find that the tube position changes in discrete steps every time an electron tunnels onto it. Edges of Coulomb diamonds acquire a (small) curvature. We also show that bistability in the tube position occurs and that tunneling of an electron onto the tube drastically modifies the quantized eigenmodes of the tube. Experimental verification of these predictions is possible in suspended tubes of sub-micron length.

## 6.1    Introduction

Nanoelectromechanical systems (NEMS) convert electrical current into mechanical motion on a nanoscale and vice versa. They can be viewed as the successors [1] of microelectromechanical-devices (MEMS) which operate at a micron scale and which are found in commercial applications. Improved performance is expected from NEM-devices due to their small sizes, and higher eigenfrequencies. M(N)EMS have already been used for high-precision measurements of force [2], electric charge [3], the thermal conductance quantum [4], and the Casimir force [5]. ¿From a fundamental point of view, NEM-physics is an unexplored field in which new phenomena are likely to be found. Examples include tunneling through moving barriers [6], additional sources of noise [7], and shuttling mechanism for transport [8, 9, 10].

Studies with NEMS have mostly been performed in devices made with silicon technology. Carbon nanotubes provide an interesting alternative because of their superior mechanical properties. They have already been implemented as
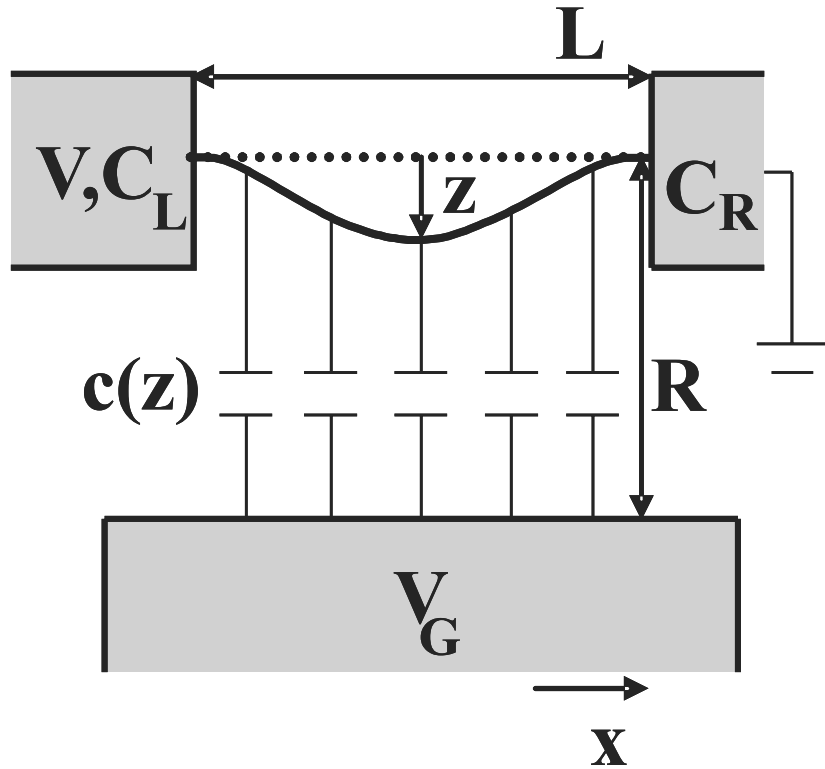


**Figure 6.1:** A schematic drawing of a suspended nanotube capacitively coupled to a gate and clamped on both sides to metal pads that serve as tunnel contacts. A voltage $V$ is applied to the left pad.

nanotweezers [11, 12], as switches in a random access memory device [13], or as nanoscale actuators [14]. In addition, recent theoretical calculations show that carbon nanotubes can also be used as nanoelectromechanical switches [15, 16] or as gigahertz oscillators [17].

In this chapter, we study theoretically nanoelectromechanical effects in doubly-clamped suspended carbon nanotubes. Doubly-clamped suspended single- and multi-wall carbon nanotubes have been previously fabricated, and their transport [18, 19, 20, 21], acoustoelectric [22], thermal [23], and elastic [24] properties have been measured. We consider a single-wall carbon nanotube (SWNT) in which Coulomb-blockade effects dominate transport, and demonstrate that a gate manipulates the tube in an effective way. The applied gate voltage bends the tube, changes the stress and thus influences the electric and mechanical properties.

This chapter is organized as follows: The next Section describes the model with inclusion of the influence of initial stress and thermal fluctuations. We concentrate on the case where the junction capacitances are zero so that analytical expressions are obtained. Section 6.3 describes the influence of nanoelectromechanical effects on Coulomb blockade and shows that intrinsic bistability occurs when the tube is strained. Section 6.4 discusses the eigenmodes and the influence on the initial strain on them. In Section 6.5 junction capacitances are no longer neglected and we also show the effect of a non-uniform charge distribution. We end with some remarks on the limitations of our model.

## 6.2 Displacement, stress, and energy

### 6.2.1 Equilibrium position

We consider a SWNT (modeled as a rod of length $L$ along the $x$-axis), freely suspended between source and drain electrodes, in the vicinity of a gate (see Fig. 1). The nanotube is attached to the electrodes via tunneling contacts. An electrostatic force (gate voltage) bends the tube; the deviation from a straight line is denoted by $z(x)$ with $0 < x < L$. The elastic energy of the bent tube is [25]

$$W_{el}[z(x)] = \int_0^L dx \left\{ \frac{EI}{2} z''^2 + \left[ \frac{T_0}{2} + \frac{ES}{8L} \int_0^L z'^2 dx \right] z'^2 \right\}, \quad (6.1)$$

where $E$, $I = \pi r^4/4$, and $S = \pi r^2$ are the elastic modulus, the inertia moment and the cross-section, respectively. Here, $r$ is the (external) radius of the tube. The first term in Eq. (6.1) is the energy of an unstressed bent rod; the two other

terms describe the effect of the stress force $\tilde{T} = T_0 + T$. Here $T_0$ is the residual stress which may result *e.g.* from the fabrication, and the induced stress $T$ is due to the elongation of the tube caused by the gate voltage,

$$T = \frac{ES}{2L} \int_0^L z'^2 dx. \tag{6.2}$$

To write down the electrostatic energy, we denote the capacitances of the barriers connecting the nanotube with the source and drain as $C_L$ and $C_R$, respectively (see Fig. 1). The capacitance to the gate per unit length is $c(z)$. Approximating the gate by an infinite plane at a distance $R$ from the nanotube, we obtain

$$c(z) = \frac{1}{2 \ln \frac{2(R-z)}{r}} \approx \frac{1}{2 \ln \frac{2R}{r}} + \frac{z(x)}{2R \ln^2 \frac{2R}{r}}, \tag{6.3}$$

where the Taylor expansion restricts validity to $z \ll R$. In this limit van der Waals forces between the nanotube and the substrate can be neglected. The electrostatic energy of the system reads

$$\begin{aligned} W_{est}[z(x)] = & \frac{(ne)^2 - 2ne(C_L V + C_G V_G)}{2(C_L + C_R + C_G)} \\ & - \frac{C_L(C_R + C_G)V^2 + C_G(C_L + C_R)V_G^2 - 2C_L C_G V V_G}{2(C_L + C_R + C_G)}, \end{aligned} \tag{6.4}$$

where $V$ and $V_G$ are the potentials of the source and the gate respectively (the drain potential is set to zero), $ne$ is the (quantized) excess charge on the nanotube, and for a uniform charge distribution the capacitance to the gate equals

$$C_G = \int_0^L c[z(x)]dx.$$

Note, that the last term in Eq. (6.4) depends on the tube displacement and thus on the number of electrons. Therefore, it can not be omitted as in the standard Coulomb blockade treatment that replaces this term by a constant making $W_{est}$ a periodic function of gate voltage.

In the following, we concentrate on the analytically tractable case $C_L, C_R = 0$. The general case is considered in Section 6.5. For a moment, we also assume $T_0 = 0$. In this situation, the expression for the electrostatic energy simplifies,

$$\begin{aligned} W_{est}[z(x)] &= \frac{(ne)^2}{2C_G[z]} - neV_G \\ &\approx \frac{(ne)^2 \ln \frac{2R}{r}}{L} - \frac{(ne)^2}{L^2 R} \int_0^L z(x)dx - neV_G. \end{aligned} \tag{6.5}$$

Minimizing the energy,

$$W_n[z(x)] = W_{el}[z(x)] + W_{est}[z(x)],$$

with respect to $z$, one finds the equation determining the tube position [25],

$$IEz'''' - Tz'' = K_0 \equiv \frac{(ne)^2}{L^2 R}, \tag{6.6}$$

where $K_0$ is the electrostatic force per unit length, which we approximate by a constant. Higher-order terms are small for $z \ll R$. To solve Eq. (6.6) we have to assume that the stress force $T$ is constant, and find it later from the self-consistent condition (Eq. (6.2)).

The solution of Eq. (6.6) with the appropriate boundary conditions (for the doubly-clamped rod $z(0) = z(L) = z'(0) = z'(L) = 0$) has the form

$$\begin{aligned} z_n(x) &= \frac{K_0 L}{2T\xi} \left[ \frac{\sinh \xi L}{\cosh \xi L - 1} (\cosh \xi x - 1) - \sinh \xi x \right. \\ &+ \left. \xi x - \xi \frac{x^2}{L} \right], \qquad \xi = \sqrt{\frac{T}{EI}}. \end{aligned} \tag{6.7}$$

Substituting this into Eq. (6.2), a relation between the stress $T$ and the external force $K_0$ is obtained. In the limiting cases, it reads

$$T = \begin{cases} K_0^2 L^6 S/(60480 EI^2), & T \ll EI/L^2, \\ (ES/24)^{1/3}(K_0 L)^{2/3}, & T \gg EI/L^2. \end{cases} \tag{6.8}$$

The first line corresponds to weak bending of the tube: The energy associated with the bending exceeds the energy of the stress. Generally, it is realized for $z \lesssim r$. The second line describes strong bending, when the tube displacement is large ($r < z \ll R, L$).

For the displacement of the tube center $z_n^{max} = z_n(L/2)$ we find

$$\begin{aligned} z_n^{max} &= 0.003 \frac{(ne)^2 L^2}{E r^4 R}, & T \ll \frac{EI}{L^2} & \left( n \ll \frac{E r^5 R}{e^2 L^2} \right); \\ z_n^{max} &= 0.24 \frac{(ne)^{2/3} L^{2/3}}{E^{1/3} r^{2/3} R^{1/3}}, & T \gg \frac{EI}{L^2} & \left( n \gg \frac{E r^5 R}{e^2 L^2} \right). \end{aligned} \tag{6.9}$$

For a SWNT with $r = 0.65$ nm, $E = 1.25$ TPa, $L = 500$ nm and $R = 100$ nm (to be referred to as the E-nanotube) the crossover from weak to strong bending, $T \sim EI/L^2$, occurs already at $n \sim 5 \div 10$. In the strong-bending regime, the displacement of the E-nanotube is (in nanometers) $z_n^{max} = 0.24 n^{2/3}$. Note that this regime is not accessible with state-of the art silicon submicron devices, which are always in the weak-bending limit.
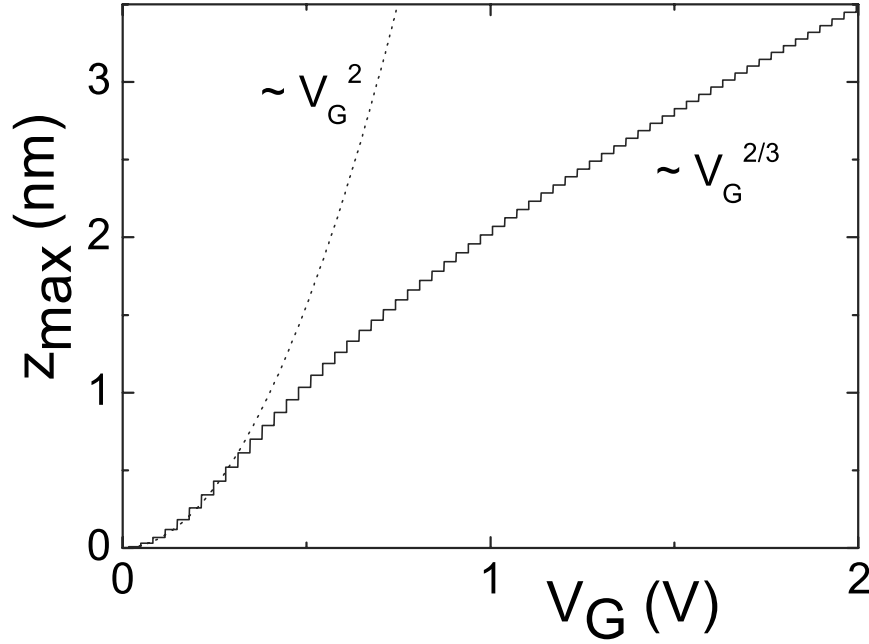
**Figure 6.2:** Calculated displacement as a function of gate voltage for the E-nanotube: $r = 0.65$ TPa, $E = 1.25$ TPa, $L = 500$ nm and $R = 100$ nm. At $V_G \approx 0.5V$, there is a crossover from weak bending with a $V_G^2$-dependence to strong bending with a $V_G^{2/3}$ dependence.

## 6.2.2   Charge and energy

For comparison with experiments, we have to relate the charge $ne$ to the gate voltage by minimizing the energy. The expression for the energy (elastic plus electrostatic) of the tube at equilibrium in the limiting cases reads

$$
\begin{aligned}
W_n^{eq} \;\equiv\; W_{st} - \delta W &= \frac{(ne)^2}{L} \ln \frac{2R}{r} - neV_G \\
&- \begin{cases} 0.0009(ne)^4 L/(Er^4R^2), & T \ll EI/L^2; \\ 0.08(ne)^{8/3}/(Er^2R^4L)^{1/3}, & T \gg EI/L^2. \end{cases}
\end{aligned}
\tag{6.10}
$$

The first two terms represent the electrostatic energy of a straight tube, and the third one is due to the elastic degrees of freedom (stress, bending, and change of $C_G$ due to displacement). This nonlinear, *nanomechanical term* is typically a small correction: For the E-nanotube it becomes of the same order as $W_{st}$ if $n \sim 3000$ in which case Eq. (6.3) is not valid anymore. The negative sign of the nanomechanical contribution is easily understood: As the gate voltage changes, the movable tube adjusts not only its charge, but also its position, which leads to a lower energy as compared to the fixed-position system.

The value of $n$ which minimizes the energy is

$$n = Int\left(\frac{V_G L}{2e\ln(2R/r)} + \frac{1}{2} + \delta n\right),$$

with $Int$ denoting the integer part of the expression. The small correction $\delta n$ in the strong-bending regime is proportional to $V_G^{5/3}$. Thus, the tube displacement $z_{max}$ changes in discrete steps when $V_G$ is varied as shown in Fig. 2. The envelope is proportional to $V_G^2$ (weak bending) or $V_G^{2/3}$ (strong bending). In the absence of charging effects and tension, the displacement is given by the dashed line as previously found in simulations of Ref. [15].

### 6.2.3 Thermal fluctuations

The preceding considerations are restricted to the case of zero temperature. To understand the role of the temperature, we now evaluate the effect of thermal fluctuations on the equilibrium position of the tube.

The variance of the position of the tube center at a given charge $n$ can be generally represented as a functional integral,

$$\begin{aligned}
\text{var } z_n &\equiv \left\langle [z(L/2) - z_n(L/2)]^2 \right\rangle \\
&= \left.\frac{\partial^2}{\partial J^2} \int Dz(x) \exp\left[-W_n[z]/k_B\Theta + Jz(L/2)\right]\right|_{J=0} \\
&\times \left[\int Dz(x)\exp\left(-W_n[z]/k_B\Theta\right)\right]^{-1},
\end{aligned}$$
(6.11)

where $\Theta$ is the temperature. Except for $n = 0$, the functional integral in Eq. (6.11) is not Gaussian and has to be linearized around the equilibrium solution $z_n(x)$, Eq. (6.7). The remaining Gaussian integral can be calculated, and we arrive at

$$\text{var } z_n = k_B\Theta\zeta(L/2),$$
(6.12)

where $\zeta(x)$ solves the equation

$$EI\zeta'''' - \frac{ES}{2L}\int z_n'^2 dx\,\zeta'' - \frac{ES}{L}z_n''\int \zeta' z_n' dx = \delta(x - L/2).$$
(6.13)

In the two limiting cases of weak and strong bending, the solution of Eq. (6.13) yields

$$\text{var } z_n = \begin{cases} k_B\Theta L^3/192EI, & n = 0 \\ k_B\Theta L/8T, & n \gg Er^5 R/e^2 L^2 \end{cases},$$
(6.14)

where the stress $T$ is still given by the lower line of Eq. (6.8). Thus, the fluctuations in the tube position are expected to grow linearly with temperature. However, their magnitude is small. For the E-nanotube, at 100K the fluctuations in the $n = 0$ state are of the order of 0.1 nanometer, and at least an order of magnitude less in the strong-bending regime.

In the calculations, we have assumed that the charge $ne$ is a fixed quantity. Close to the degeneracy points $W_n^{eq} = W_{n+1}^{eq}$ thermal fluctuations may induce switching between the states with charges $ne$ and $(n + 1)e$, in which case Eq. (6.14) is no longer valid. However, the range of voltages where switching is important, is narrow.

## 6.3   Coulomb effects and bistability

### 6.3.1   Coulomb blockade

Since the nanotube is attached to the electrodes by tunneling contacts, it is in the Coulomb blockade regime. We define the energy to add the $n$th electron to the tube as $S_n = W_n - W_{n-1}$. Then, if the nanotube contains $n > 0$ electrons, the conditions that current can not flow (is Coulomb blocked) are $S_n < 0, eV < S_{n+1}$. In quantum dots, $S_n$ depends linearly on the bias $V$ and gate $V_g$ voltages. Thus, in the $V_G - V$ plane regions with zero current are confined within Coulomb diamonds, that are identical diamond-shape structures repeating along the $V_G$–axis.

In a suspended carbon nanotube, in addition to the purely Coulomb energy, we also have the nanomechanical corrections. Generally, these corrections make the relations between $V$ and $V_G$, which describe the boundaries of Coulomb blockade regions, non-linear. Consequently, the Coulomb "diamonds" in suspended nanotubes are not diamonds any more, but instead have a curvilinear shape (with the exception of the case $C_L = C_R = 0$). Their size is also not the same and decreases with $|V_G|$. Thus, the mechanical degrees of freedom *affect* the Coulomb blockade diamonds. However, since these effects originate from the nanomechanical term which is typically a small correction, its influence on Coulomb diamonds is small as well. For the E-nanotube, these effects do not exceed several percents for typical gate voltages.

### 6.3.2   Two-gate setup and bistability

To demonstrate that the nanomechanical effects can not generally be omitted, we consider a suspended tube symmetrically placed in between two gates and show below that bistability in the tube position occurs [26].

Fig. 1 again presents the schematic setup, but the suspended tube is placed between two gates, labeled up (U) and down (D). Since up and down capacitances are connected in parallel, their sum $C_G = C_U + C_D$ matters. Assuming that the distance of the straight tube to both gates is the same, we write

$$C_{U,D} = \int_0^L \frac{dx}{2 \ln \frac{2(R \mp z)}{r}}, \tag{6.15}$$

Expanding this for $z \ll R$ and calculating the electrostatic force, we arrive at an equation similar to Eq. (6.6), with a constant force $K_0$ that is replaced by $\gamma z$, where

$$\gamma = \frac{(ne)^2(\ln 2R/r + 2)}{2L^2 R^2 \ln 2R/r}.$$

We now solve this equation in the strong-bending regime. For this purpose [25] we disregard the term $IEz''''$, and use the boundary conditions $z(0) = z(L) = 0$. Multiple solutions emerge; the ones with the lowest energy are

$$z = \pm \frac{2L^2}{\pi^2} \sqrt{\frac{\gamma}{ES}} \sin \frac{\pi x}{L}. \tag{6.16}$$

Thus, the tube in the strong-bending regime can oscillate between the two symmetric positions. This creates a basis for observation of quantum effects, as discussed in Ref. [26]. We emphasize once again, that within this model, the multi-stability is due to the charging of the tube in combination with the non-linearity.

## 6.4 Eigenmodes

The eigenfrequency of a particular eigenmode is an important directly measurable [22] property. In future experiments on suspended tubes we expect that the eigenmodes influence tunneling ("phonon-assisted tunneling") in a similar way as observed for a single $C_{60}$ molecule [10]. Below, we demonstrate that the effect of the electrostatic interactions on the elastic properties (specifically, eigenfrequencies) is strong and changes the behavior qualitatively.

To find the eigenmodes, we apply a gate voltage with a large dc (single gate) and a small ac component. The displacement $z(x,t)$ is time-dependent, which provides an external force $-\rho S \ddot{z}$ to Eq. (6.6), where $\rho$ equals 1.35 g/cm$^3$. Eq. (6.6) must be solved first with a constant stress, and then the stress is found self-consistently. The tube displacement has a small ac component $\delta z$ on top of a

large static one. The self-consistency procedure is essentially the same and again leads to Eq. (6.8). Thus, the dc component of the gate voltage determines the stress $T$ and it therefore controls the eigenmodes.

The frequencies of the (transverse) eigenmodes are found from the requirement that the equation

$$IE\delta z'''' - T\delta z'' - \rho S\omega^2 \delta z = 0 \tag{6.17}$$

with the boundary condition $\delta z(0) = \delta z(L) = \delta z'(0) = \delta z'(L) = 0$ has a non-zero solution. This yields the following equation for the frequency $\omega$,

$$\cosh y_1 \cos y_2 - \frac{1}{2}\frac{y_1^2 - y_2^2}{y_1 y_2}\sinh y_1 \sin y_2 = 1, \tag{6.18}$$

$$y_{1,2} = \frac{L}{\sqrt{2}}\left(\sqrt{\xi^4 + 4\lambda^2} \pm \xi^2\right)^{1/2}, \quad \lambda = \sqrt{\frac{\rho S}{EI}}\omega.$$

In the following, we restrict ourselves to the fundamental (lowest frequency) eigenmode $\omega_0$. In the limiting cases, the solutions of Eq. (6.18) are

$$\omega_0 = \sqrt{\frac{EI}{\rho S}}\begin{cases} 22.38L^{-2} + 0.28\xi^2, & \xi L \ll 1; \\ \pi\xi L^{-1} + 2\pi L^{-2}, & \xi L \gg 1. \end{cases} \tag{6.19}$$

The second terms on the rhs represent small corrections to the first ones.

The frequency dependence $\omega_0 \propto L^{-2}$ is associated with a loose string, while $\omega_0 \propto L^{-1}$ means that the string is tied like in a guitar. Our results show that the behavior of the tube crosses over from "loose" to "tied" as $V_G$ increases. For the fundamental mode, the crossover occurs at $\xi L \sim 1$, corresponding to the crossover from weak to strong bending. The middle curve in Fig. 3 shows the frequency of the fundamental mode as a function of gate voltage (zero residual stress). The arrow denotes the cross-over from weak to strong bending.

The gate voltage dependence of the frequency is a stepwise function, as shown in the inset of Fig. 3. Steps occur whenever an additional electron tunnels onto the tube. For the E-nanotube, their height is $\sim 5$ MHz, which is measurable. Note, that the present submicron silicon devices are always in the weak-bending regime so that corrections due to the second term in Eq. (6.19) are too small to be measured. Furthermore, one should realize that frequency quantization is only observable if the frequency itself is greater than the inverse tunneling time for electrons.

We now consider the effect of a residual stress ($T_0 \neq 0$). First, we obtain the stress by solving Eqs. (6.2), (6.6) (in the latter, $T$ is replaced by $T + T_0$). In particular, for a negative stress $T + T_0 < 0$, $T_0 \sim -EI/L^2$, Eq. (6.2) acquires
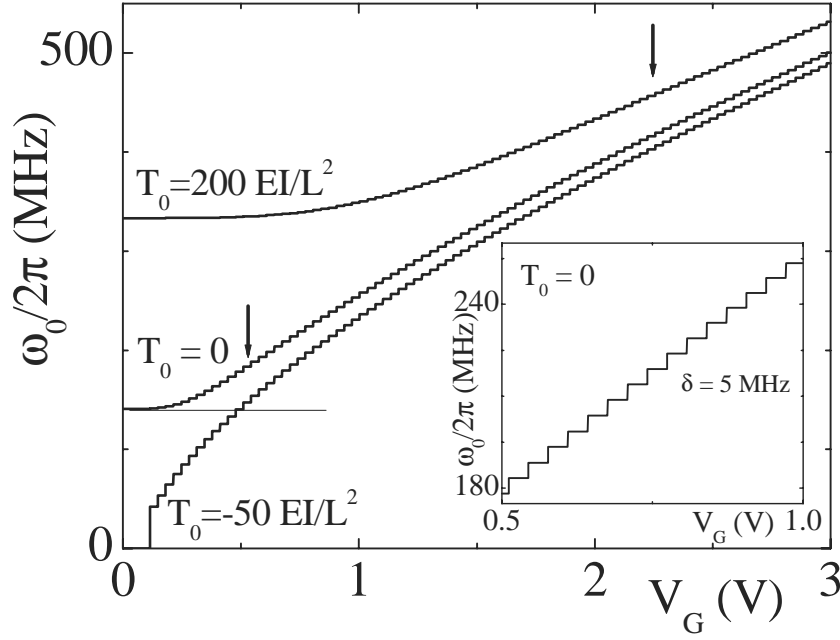
**Figure 6.3:** Gate voltage dependence of the frequency $\omega_0$ of the fundamental mode for three different values of the residual stress. Numbers are taken for the E-nanotube (see Fig. 2). The fundamental mode of an unstressed tube is 140 MHz (thin horizontal line). The inset is an enlargement of the $T_0 = 0$ curve of the main figure showing step-wise increases of $\omega_0$ whenever an additional electron tunnels onto the tube.

several solutions. This signals *Euler instability*: the tube bends in the absence of an external force.

If the residual stress is large, $T_0 \gg EI/L^2$, the tube always acts like a tied string (upper curve in Fig. 3). The frequency depends weakly on $V_G$ for low voltages, and above $T \sim T_0$ (denoted with the arrow) grows with an envelope $\propto V_G^{2/3}$. For negative $T_0$ the picture is qualitatively different (lower curve in Fig. 3). Whereas for large gate voltages the envelope is still proportional to $V_G^{2/3}$, the frequency dives below the value for an unstressed tube ($22.38(EI/\rho S)^{1/2}L^{-2}$, represented by the thin solid line in Fig. 3), when the overall stress becomes negative. It further drops to zero at the Euler instability threshold.

The qualitative difference between the various regimes means that by measuring the gate voltage dependence of $\omega_0$ one can determine the sign of $T_0$ and get a quantitative estimate. On the other side, the gate effect can be used to tune the eigenfrequencies. We also mention that in the absence of charging effects, the steps vanish but the overall shape of the curves in Fig. 3 remains the same.

## 6.5   Relaxing the approximations

While considering equilibrium displacement and eigenmodes of the nanotube, we made a number of simplifying approximations. In this Section, we consider two of them — disregarding the capacitances $C_{L,R}$ and uniform distribution of the charge — and show that relaxing these approximations affects the above results quantitatively, but not qualitatively.

In this Section, we consider the case of zero residual stress $T_0 = 0$.

### 6.5.1   Finite capacitances to the leads

We now relax the limitation $C_L, C_R = 0$. For the general case, Eq. (6.6) still holds, however, the force $K_0$ must be adjusted,

$$K_0 = \frac{1}{L^2 R} \frac{C_0^2}{(C_0 + C_R + C_L)^2} \left[ ne + (C_L + C_R)V_G - C_L V \right]^2, \tag{6.20}$$

where $C_0 = L/(2\ln 2R/r)$ is the capacitance of the straight nanotube to the gate. The results of the numerical solutions for the displacement and the frequency of the fundamental mode are plotted in Fig. 6.4. For simplicity we have taken $C_L = C_R = \phi C_G$; the four curves correspond to different values of the parameter $\phi$. The curves with $\phi = 0$ are the same as the ones in Figs. 6.2, **??**.

The plots demonstrate that the qualitative picture remains the same if we include finite capacitances to the leads. The steps observed for $\phi = 0$ become skewed with the increase of $C_L$ and $C_R$ (see inset of Fig. 4). At a certain $\phi$ they disappear. For $\phi > 10$ the plots are, on the scale presented, the same.

### 6.5.2   Non-uniform charge distribution

Above, we have assumed a uniform charge distribution along the nanotube. Rather than trying to analyze the effect in general, we consider the opposite situation when the excess charge is concentrated at one point (to be more precise, in a concise region of the tube radius $r$), which may represent, for instance, a pinning center. This center is placed in the middle of the nanotube. Though we believe that the charge distribution in suspended nanotubes is closer to uniform, this situation applies to a suspended quantum dot as realized recently [27].

The gate-charge capacitance $C_G$ in this geometry is

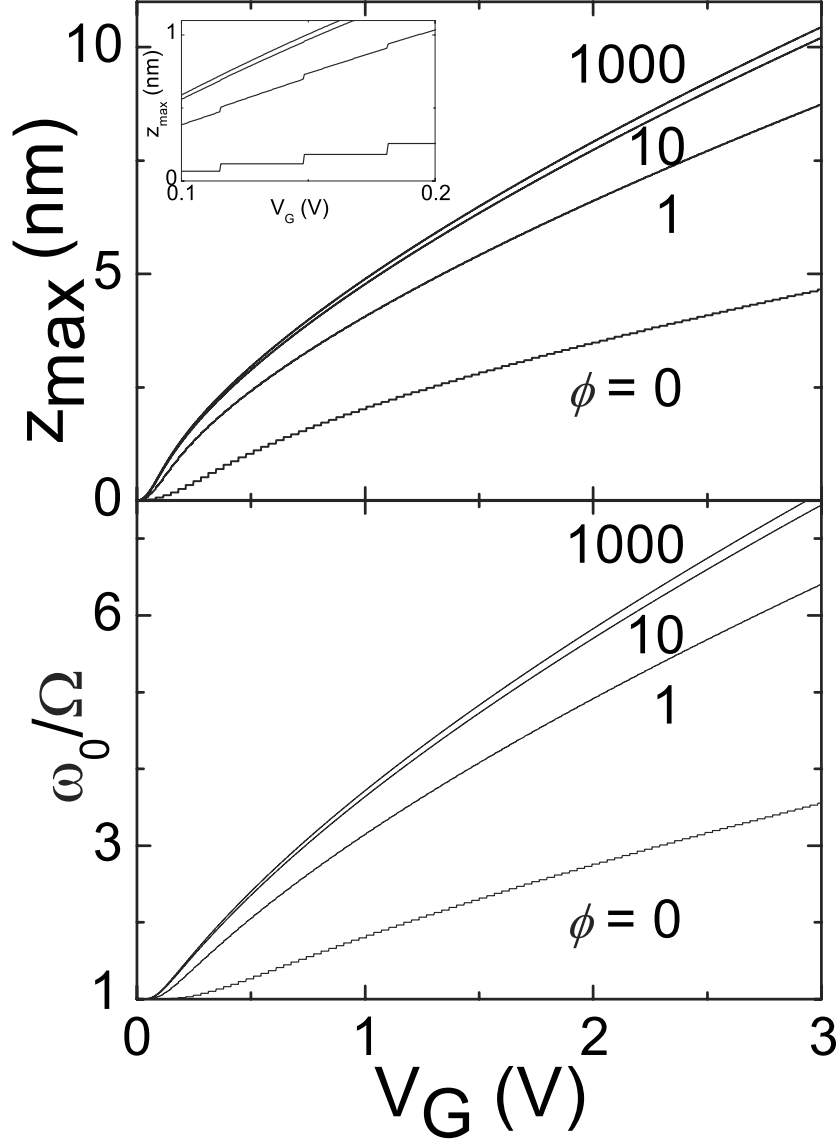$$C = \frac{1}{\frac{1}{r} - \frac{1}{2R}}, \tag{6.21}$$

**Figure 6.4:** Above: Displacement as a function of gate voltage for the E-nanotube with finite capacitances to the leads. The four curves correspond to different values of the parameter $\phi$, defined as $C_L = C_R = \phi C_G$. The inset is an enlargement of the main figure. Below: The frequency of the fundamental mode normalized to the fundamental frequency of an unstressed tube $\Omega = (22.38L^{-2}(EI/\rho S)^{1/2} = 141$ MHz for the same parameters as above.

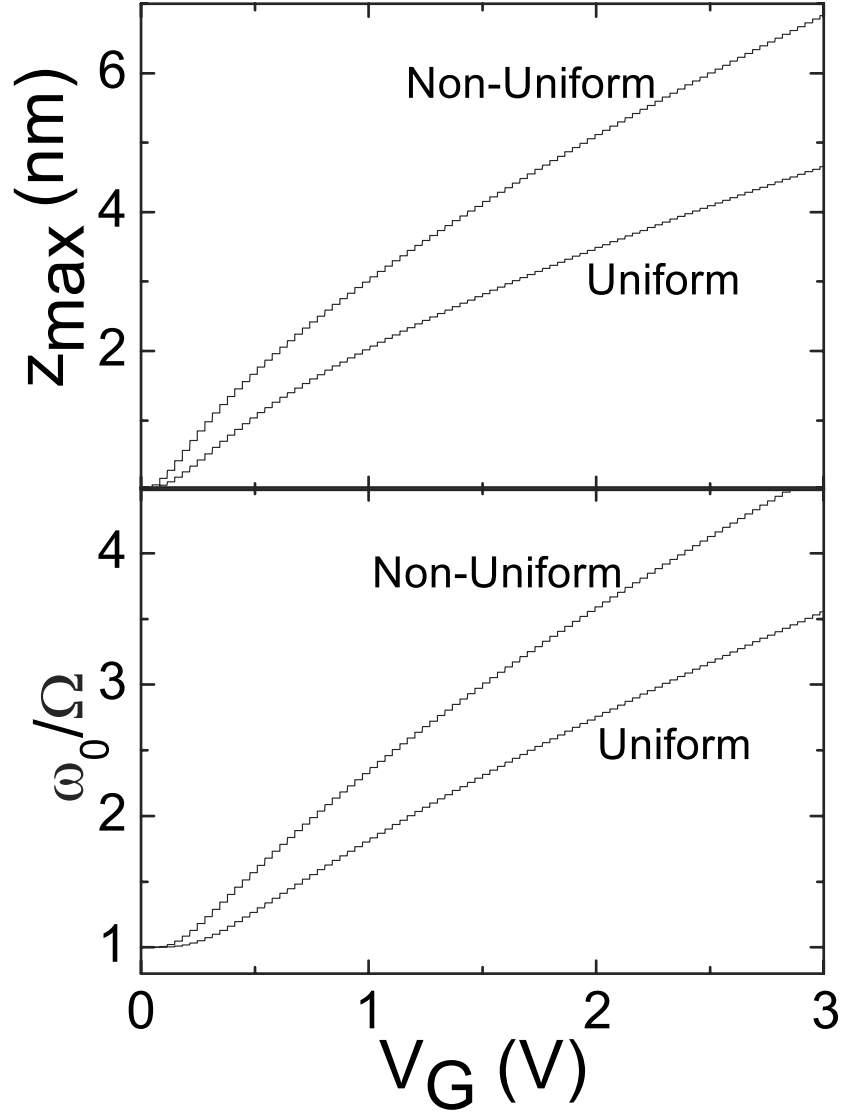**Figure 6.5:** Displacement of the center of the E-nanotube (above) and the frequency of the fundamental eigenmode (below) for uniform charge distribution and for the case that the charge is concentrated at one point. $\Omega$ is the fundamental frequency of an unstressed tube.

and we proceed to obtain the equations of motion,

$$ IEz'''' - Tz'' = F\delta\left(x - \frac{L}{2}\right), \quad F \equiv \frac{(ne)^2}{4R^2}, \tag{6.22} $$

where we again set $C_L = C_R = 0$.

The solution with the same boundary conditions as previously, $z(0) = z(L) = z'(0) = z'(L) = 0$, and with $z$, $z'$, and $z''$ all continuous at $x = L/2$, is

$$z(x) = \frac{F}{2EI\xi^3}\left\{\tanh\frac{\xi L}{2}[\cosh\xi x - 1] - \sinh\xi x + \xi x\right\} \tag{6.23}$$

for $0 < x < L/2$. For $L/2 < x < L$ the coordinate $x$ should be replaced by $(L - x)$ because $z(x) = z(L - x)$. As before, $\xi = (T/EI)^{1/2}$ and Eq. (6.2) is used to obtain the stress self-consistently,

$$T = \begin{cases} F^2 L^4 S/(30720 EI^2), & T \ll EI/L^2, \\ (1/2)(ESF^2)^{1/3}, & T \gg EI/L^2. \end{cases} \tag{6.24}$$

Consider now the strong-bending regime and compare the results for the stress $T_u$ for the uniform (lower line of Eq. (6.8) and $T_n$ for the concentrated (lower line of Eq. (6.24) charge distributions,

$$T_n = T_u\left(\frac{\sqrt{3}L}{4R}\right)^{2/3}. \tag{6.25}$$

For $L \gg R$ we formally have $T_n \gg T_u$. This means that for the same gate voltage more stress is induced at the nanotube if the charge is concentrated at one point. Also, the displacement of the tube is greater in the concentrated case,

$$z_{max}^n = 0.87\left(\frac{L}{R}\right)^{1/3} z_{max}^u.$$

Thus, if the charge distribution is concentrated, NEMS are "more effective" than for the uniform charge. For the E-nanotube the ratio between non-uniform and uniform maximal displacement is 1.49. The difference between uniform and non-uniform charge distributions is illustrated in Fig. 6.5.

## 6.6 Discussion

The presented model is simplified in many respects. Mechanical degrees of freedom are introduced via classical theory of elasticity: The nanotube (modeled by a rod) is considered as incompressible and without internal structure. This is justified, since so far the theory of elasticity has described all existing experiments on carbon nanotubes well. For SWNTs it has been also supported by simulations (Ref. [15]). Creation of defects in SWNT starts at deformations of order of ten percents. For larger deformations (see *e.g.* Ref. [28]) we expect strong deviations

from the behavior we describe, but this typically lies outside our applicability range $z \ll R$. We have neglected damping, which is also expected to originate from the creation of the defects and to be irrelevant in this range. We also disregarded quantum effects (cotunneling and finite spacing of quantum levels of electrons in the tube). These issues need to be clarified for a detailed comparison with the experimental data, and will be a subject for future research.

Our main result is that the nanotube can be manipulated by the gate voltage, which determines its deformation and stress, and modifies the eigenmodes. Though the eigenmodes of nanotube ropes have been measured in Ref. [22] three years ago, the *strain dependence* of the eigenmodes was only recently reported in Ref. [29] which was published after this manuscript had been submitted for publication. Ref. [29] demonstrates this effect for singly-clamped multi-wall carbon nanotubes. We expect that our predictions will soon be tested in experiments on doubly-clamped SWNTs.

# References

[1] M. L. Roukes, *Nanoelectromechanical systems face the future.* Phys. World **14**, 25 (2001).

[2] T. D. Stowe *et al.*, *Attonewton force detection using ultrathin silicon cantilevers.* Appl. Phys. Lett. **71**, 288 (1997).

[3] A. N. Cleland and M. L. Roukes, *A nanometre-scale mechanical electrometer.* Nature (London) **392**, 160 (1998).

[4] K. Schwab, E. A. Henriksen, J. M. Worlock, and M. L. Roukes, *Measurement of the quantum of thermal conductance.* Nature (London) **404**, 974 (2000).

[5] H. B. Chan, V. A. Aksyuk, R. N. Kleiman, D. J. Bishop, and F. Capasso, *Quantum mechanical actuation of microelectromechanical systems by the Casimir force.* Science **291**, 1941 (2001).

[6] N. F. Schwabe, A. N. Cleland, M. C. Cross, and M. L. Roukes, *Perturbation of Tunneling Processes by Mechanical Degrees of Freedom in Mesoscopic Junctions.* Phys. Rev. B **52**, 12911 (1995).

[7] A. V. Shytov, L. S. Levitov, and C. W. J. Beenakker, *Electromechanical noise in a diffusive conductor.* Phys. Rev. Lett. **88**, 228303 (2002).

[8] L. Y. Gorelik *et al.*, *Shuttle mechanism for charge transfer in Coulomb blockade nanostructures.* Phys. Rev. Lett. **80**, 4526 (1998).; C. Weiss and W. Zwerger, *Accuracy of a mechanical single-electron shuttle.* Europhys. Lett. **47**, 97 (1999).; T. Nord, L. Y. Gorelik, R. I. Shekhter, and M. Jonson, *Electromechanics of charge shuttling in dissipative nanostructures.* Phys. Rev. B **65**, 165312 (2002).

[9] M. T. Tuominen, R. V. Krotkov, and M. L. Breuer, *Stepwise and hysteretic transport behavior of an electromechanical charge shuttle.* Phys. Rev. Lett. **83**, 3025 (1999).; A. Erbe, C. Weiss, W. Zwerger, and R. H. Blick, *Nanomechanical resonator shuttling single electrons at radio frequencies.* Phys. Rev. Lett. **87**, 096106 (2001).

[10] H. Park *et al.*, *Nanomechanical oscillations in a single-C-60 transistor.* Nature (London) **407**, 57 (2000).

[11] P. Kim and C. M. Lieber, *Nanotube nanotweezers.* Science **286**, 2148 (1999).

[12] S. Akita *et al.*, *Nanotweezers consisting of carbon nanotubes operating in an atomic force microscope.* Appl. Phys. Lett. **79**, 1691 (2001).

[13] T. Rueckes *et al.*, *Carbon nanotube-based nonvolatile random access memory for molecular computing.* Science **289**, 94 (2000).

[14] See *e.g.* R. H. Baughman *et al.*, *Carbon nanotube actuators.* Science **284**, 1340 (1999).

[15] M. Dequesnes, S. V. Rotkin, and N. R. Aluru, *Calculation of pull-in voltages for carbon-nanotube-based nanoelectromechanical switches.* Nanotechnology **13**, 120 (2002).

[16] J. M. Kinaret, T. Nord, and S. Viefers, *A carbon-nanotube-based nanorelay.* Appl. Phys. Lett. **82**, 1287 (2003).

[17] Q. S. Zheng and Q. Jiang, *Multiwalled carbon nanotubes as gigahertz oscillators.* Phys. Rev. Lett. **88**, 045503 (2002).; S. B. Legoas *et al.*, *Molecular-dynamics simulations of carbon nanotubes as gigahertz oscillators.* Phys. Rev. Lett. **90**, 055504 (2003). 055504 (2003).

[18] T. W. Tombler *et al.*, *Reversible electromechanical characteristics of carbon nanotubes under local-probe manipulation.* Nature (London) **405**, 769 (2000).

[19] J. Nygård and D. H. Cobden, *Quantum dots in suspended single-wall carbon nanotubes.* Appl. Phys. Lett. **79**, 4216 (2001).

[20] P. A. Williams *et al.*, *Controlled placement of an individual carbon nanotube onto a microelectromechanical structure.* Appl. Phys. Lett. **80**, 2574 (2002).

[21] N. R. Franklin *et al.*, *Integration of suspended carbon nanotube arrays into electronic devices and electromechanical systems.* Appl. Phys. Lett. **81**, 913 (2002).

[22] B. Reulet *et al.*, *Acoustoelectric effects in carbon nanotubes.* Phys. Rev. Lett. **85**, 2829 (2000).

[23] P. Kim, L. Shi, A. Majumdar, and P. L. McEuen, *Thermal transport measurements of individual multiwalled nanotubes.* Phys. Rev. Lett. **87**, 215502 (2001).

[24] G. T. Kim, G. Gu, U. Waizmann, and S. Roth, *Simple method to prepare individual suspended nanofibers.* Appl. Phys. Lett. **80**, 1815 (2002).

[25] L. D. Landau and E. M. Lifshitz, *Theory of Elasticity* (Pergamon, Oxford, 1986).

[26] S. M. Carr, W. E. Lawrence, and M. N. Wybourne, *Accessibility of quantum effects in mesomechanical systems.* Phys. Rev. B **64**, 220101 (2001) discuss a bistability as a result of *externally applied* negative residual tension. We emphasize that in our case it appears for an arbitrary residual tension, in the regime when the charging effects drive the tube into the strong-bending regime.

[27] E. M. Höhberger *et al.*, *Magnetotransport in freely suspended two-dimensional electron systems for integrated nanomechanical resonators.* Physica E **12**, 487 (2002).; E. M. Höhberger *et al* (unpublished).

[28] B. I. Yakobson, C. J. Brabec, and J. Bernholc, *Nanomechanics of carbon tubes: Instabilities beyond linear response.* Phys. Rev. Lett. **76**, 2511 (1996).

[29] S. T. Purcell, P. Vincent, C. Journet, and V. T. Binh, *Tuning of nanotube mechanical resonances by electric field pulling.* Phys. Rev. Lett. **89**, 276103 (2002).

# Chapter 7

# Tunneling in suspended carbon nanotubes assisted by longitudinal phonons

S. Sapmaz, P. Jarillo-Herrero,
Ya. M. Blanter, C. Dekker, and H.S.J. van der Zant

Current-voltage characteristics of suspended single-wall carbon nanotube quantum dots show a series of steps equally spaced in voltage. The energy scale of this harmonic, low-energy excitation spectrum is consistent with that of the longitudinal low-$k$ phonon mode (stretching mode) in the nanotube. Agreement is found with a Franck-Condon-based model in which the phonon-assisted tunneling process is modeled as a coupling of electronic levels to underdamped quantum harmonic oscillators. Comparison with this model indicates a rather strong electron-phonon coupling factor of order unity.

## 7.1   Introduction

In nano-electromechanical systems (NEMS), mechanical motion affects electrical current and vice versa [1, 2, 3, 4]. Of special interest is the study of electron-phonon coupling in these devices since tunneling of a single electron may induce a displacement of the movable structure [5, 6, 7, 8, 9, 10]. The interaction strength is characterized by the dimensionless electron-phonon (e-ph) coupling constant $g$, which is proportional to the ratio of the classical and the quantum displacement. In bulk systems the e-ph coupling is generally weak and the coupling constant is orders of magnitude smaller than one. However, since the coupling dramatically increases with decreasing device mass, NEM-devices may exhibit an intermediate to strong e-ph coupling [11, 12, 13]. In this regime, current-voltage characteristics are expected to exhibit additional steps whose height can be used as an estimate of $g$. For example, $g$ is around one in the $C_{60}$ molecular devices of Ref. [11], while measurements on different $C_{140}$ samples [12] indicate a value of $g$ between 0.2 and 8.

Carbon nanotubes (NTs) are ideal systems for exploring electro-mechanical effects since they have a small diameter, a low mass, and can be defect free on a molecular level. In experiments on suspended nanotubes, different methods have already been used to probe the bending [14, 15] and radial breathing mode (RBM) [16]. The measurements show that the free-hanging tubes operate in the underdamped regime of low dissipation. For the fundamental bending mode the reported quality factor is about 100; for the RBM it is estimated as high as 10000.

Here we present electronic transport spectroscopy measurements on suspended carbon nanotubes, which show signatures of phonon-assisted tunneling, evidenced by the presence of a series of steps in the $I - V$ characteristics. Such steps form a harmonic low-energy spectrum, whose energy scale and length dependence are consistent with that of the longitudinal stretching mode. Comparison with the Franck-Condon theory shows that the e-ph coupling constant is of order one.

Devices are fabricated by locating individual nanotubes (laser ablation and CVD) on a $Si/SiO_2$ substrate using an atomic force microscope (AFM) with respect to predefined markers. Subsequently, the electrodes are made using conventional e-beam lithography techniques and thermal evaporation of Cr (5 nm) and Au (50 nm). The nanotubes are suspended by removing the underlying $SiO_2$ in a wet etch step using buffered HF [17]. A schematic sample geometry and SEM micrograph are shown in Fig. 7.1. In the experiment the source and gate voltage are defined with respect to the drain, which is connected to ground.
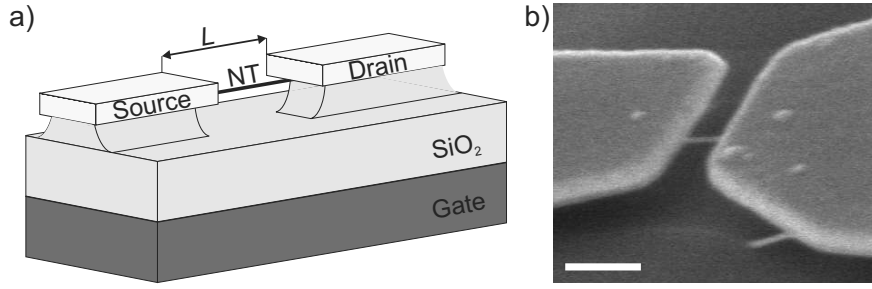
**Figure 7.1: (a)** Schematic drawing of a suspended nanotube clamped between two Cr/Au electrodes on top of silicon oxide. The underlying oxide is partially removed by a wet etch step leaving the nanotube suspended. The highly doped silicon plane is used as a global gate to tune the electrostatic potential of the nanotube. **(b)** Scanning-electron microscope micrograph of a suspended nanotube. The scale-bar represents 200 nm.

## 7.2 Stability diagrams and low-energy spectra

In Fig. 7.2 we show stability diagrams for three nanotubes measured at 10 mK (a) and 300 mK (b,c) where the differential conductance, $dI/dV$, is plotted versus bias and gate voltage. The three metallic nanotubes have a length between source and drain contacts, $L$, ranging from 0.14 to 1.2 $\mu$m. Their diameter $d$ is between 1 and 1.4 nm as determined from AFM imaging. In the diamond shaped regions (Coulomb diamonds) the current is zero due to Coulomb blockade, and the charge number in the dot is fixed. Regular and closing Coulomb diamonds indicate single dot behavior [18, 19] in all three samples for the gate range shown. Notice that the diamonds in Fig. 7.2a do close, as shown in the inset, which was taken at a higher temperature (300 mK) in a different cooldown. The low-bias current, however, is suppressed which could be a signature of strong electron-phonon coupling [5, 9, 10].

Excitations of a quantum dot appear as lines running parallel to the Coulomb diamond edges in the stability diagrams [18]. At such a line, a new electronic level becomes resonant with the leads and an additional transport channel opens up. The energy of an excitation can be determined by reading off the intersection point between the excitation line and the Coulomb diamond edge on the bias axis [19]. Furthermore, the excitations correspond to the charge state of the Coulomb diamond they end up in. Electronic excitations in nanotubes typically differ between adjacent charge states [20]. In Fig. 7.2a, a dense set of equally spaced excitation lines (starting from the first electronic excitation) is clearly visible near $V_G = 210$ mV and 230 mV, i.e., adjacent charge states exhibit a similar set of excitations with approximately the same energy spacing. The fact
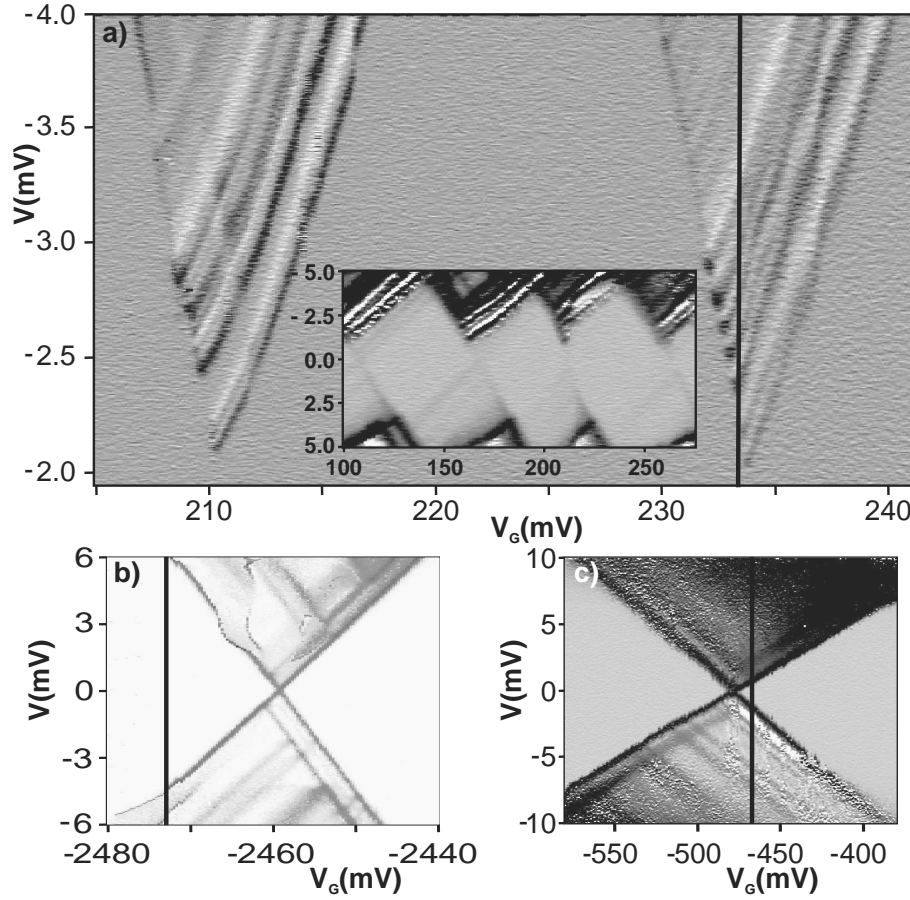
**Figure 7.2:** Stability diagrams for three different suspended nanotubes with a length in between contacts of 1.2 $\mu$m, 420 nm, and 140 nm for **(a)**,**(b)** and **(c)** respectively. The conductance $(dI/dV)$ is plotted as a function of source-drain voltage, $V$, and gate voltage, $V_G$. White corresponds to low and Dark to high conductance. Measurements have been performed at $T$=300 mK except in **(a)**, where the base temperature was 10 mK. **(a)** Small region of a stability diagram showing closely spaced sets of lines running parallel to the Coulomb diamond edges for two charge states. At low bias, a strong suppression of the conductance is present. Consecutive dark and white lines indicate positive differential conductance. Inset: regular diamonds that close are observed in a different cool down at $T$= 300 mK. **(b)** and **(c)** Diamond crossings for two other samples, again showing lines parallel to the diamond edges with energy separations smaller than expected for electronic excitations.

that excitations occur primarily in one direction is due to asymmetric tunnel barriers [19].

The energy differences between the excitation lines of Fig. 7.2 are shown in the insets of Fig. 7.3. In all three cases, the excitation energy is an integer multiple

of the first (fundamental) excitation. Thus, they form a harmonic spectrum with up to 5 levels. A linear fit yields an excitation energy of 140, 690, and 530 $\mu$eV for the tubes with length 1.2 $\mu$m (a), 420 nm (b), and 140 nm (c), respectively. These values are an order of magnitude smaller than the expected mean electronic level spacing given by $\Delta = h v_F / 2L$ with $h$ the Planck constant and $v_F = 8.1 \cdot 10^5$ m/s [21] the Fermi velocity.
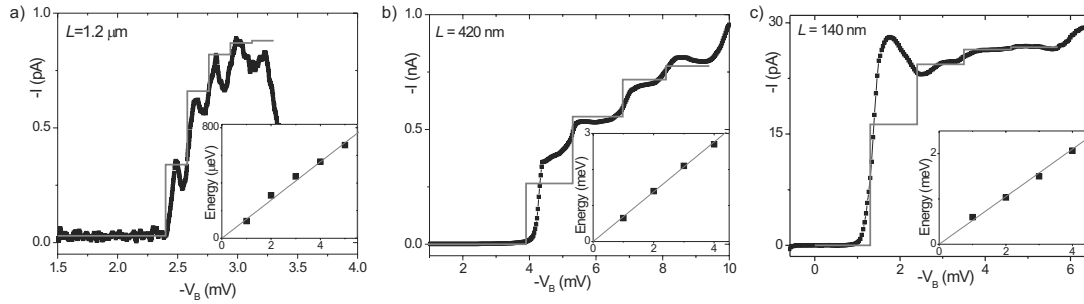


**Figure 7.3:** Current as a function of source-drain voltage at a gate voltage indicated by the black lines in Fig. 7.2. The lines represent the step heights calculated in the Franck-Condon model (see text) for an electron-phonon coupling parameter of 0.95, 1.1, and 0.5 for **(a)**, **(b)**, and **(c)** respectively. In the insets, the energy separation between the peaks or steps (lines in Fig. 2) is plotted, showing equally spaced, harmonic spectrum. The slope of the drawn line is 140, 690, and 530 $\mu$eV for the insets of **(a)**, **(b)**, and **(c)** respectively.

## 7.3 Vibrational states and Franck-Condon model

A more natural explanation for the observed harmonic spectra is a vibrational mode coupled to an electron tunneling [11]. Multiple steps with identical spacing would then arise from the excitation of an integer number of vibrational quanta. Indeed, the observed equidistant energy separation is consistent with that expected from the longitudinal stretching mode in the nanotubes. In Fig. 7.4, we plot the energy of important low-energy vibrational modes of single-wall nanotubes [22, 23]. For comparison, we plot the mean electronic energy level separation, $\Delta$, in black. Squares correspond to the fundamental excitation energy extracted from the linear fits in the insets of Fig. 7.3. The energy of the radial breathing mode does not depend on the nanotube length and equals 28 meV/$d$(nm). The bending mode has a $L^{-2}$ dependence [25], and an energy much smaller than the measured excitation energy. The stretching mode vibra-

tion energy is inversely proportional to the length [24], $E = (nh/L)\sqrt{Y/\rho_m}$, where $Y$ is Young's modulus, $\rho_m$ is the density and $n$ is the vibrational quantum number. For nanotubes with $\rho_m = 1.3$ g/cm$^3$, $Y = 1$ TPa the vibrational energy corresponding to the fundamental mode is $\sim 110$ $\mu$eV$/L(\mu$m) [23]. As Fig. 7.4 shows, the data are in good agreement with these predicted values.
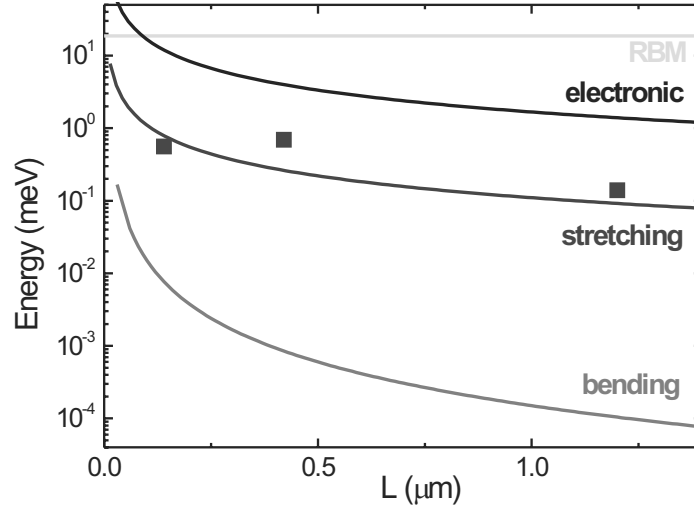


**Figure 7.4:** Energy scales of different vibrations and electronic excitations plotted on a log scale for a nanotube with a 1.4 nm diameter. The radial breathing mode does not depend on the length $L$. The bending mode vibrations have a $L^{-2}$ dependence. The mean electronic level spacing and the stretching mode (blue) vibrations depend inversely on the length.

The coupling of electronic levels with vibrational modes (quantum harmonic oscillators) can be described in terms of the Franck-Condon model [26]. According to the Franck-Condon principle, an electron in an electronic transition moves so fast that the nuclear positions are virtually the same immediately before and after the transition. As a consequence, the transition rate is proportional to the Franck-Condon factors defined as the square of the overlap integral between the vibrational wavefunctions of the two states involved. An important parameter is the electron-phonon coupling factor, $g = \frac{1}{2}(\frac{x}{x_0})^2$. This is the ratio of the classical displacement length, $x$, to the quantum mechanical oscillator length, $x_0 = \sqrt{\hbar/m\omega}$. Alternatively, $g = \frac{F^2}{2\hbar m\omega^3}$, where $F$ is the force on, $m$ the mass of, and $\omega$ the frequency of the oscillator.

For low damping, the vibrational levels remain sharp and the Franck-Condon

model predicts steps in the current-voltage characteristics, that are equally spaced in energy (bias voltage). In the presence of strong relaxation, the normalized step heights are given by [5]: $P_n = e^{-g}g^n/n!$. In the strong coupling ($g \gg 1$) limit, the height of the first steps is exponentially suppressed (phonon blockade) [5, 9, 10]. Multiple steps only arise if $g$ is of the order of one or larger and the observation of a spectrum of equally spaced excitation lines therefore indicates that the e-ph coupling in our suspended nanotubes must be rather strong.

In Fig. 7.3, the red curves represent the step heights ($P_n$) given by the Franck-Condon model with strong relaxation discussed above. The symbols are the experimental curves taken at the green lines in Fig. 7.2. Considering the simplicity of the model, reasonable agreement is obtained in all three cases. The comparison yields an estimate of $g$ of 0.95, 1.1, and 0.5 in Fig. 7.3a, b, and c respectively, indicating that it is approximately length independent. We have also performed a similar analysis at other gate voltages yielding the same $g$-values.

The theoretical curves in Fig. 7.3 do not exactly follow the measured ones. Better fits may be obtained if the influence of a gate voltage and asymmetric coupling is considered [5], or if coupling to excited electronic states [27] is considered, or if the influence of damping or non-equilibrium phonons (weak relaxation) is taken into account. In the latter case the peak heights are expected to display a non-systematic dependence on $g$ and peak number [9]. Consideration of these effects is, however, beyond the scope of this chapter.

## 7.4 Electron-phonon coupling

Let us now make some estimates for the electron-phonon coupling parameter $g$. First, we note that the coupling between electrons and longitudinal phonons is expected to be weak. Indeed, in the leading approximation the nanotube is parallel to the plane of the gate, and thus the force from the gate is perpendicular to the displacement produced by the longitudinal phonons — there is no coupling associated with the gate. The electron-phonon interactions come in this case from the same mechanism as in the bulk graphite — coupling to the polarization charge — and the corresponding coupling constant is small.

This is not entirely correct, since the gate bends the nanotube, and the displacement along the tube is actually skewed with respect to the gate plane. The coupling corresponding to this mechanism can be estimated as follows: Let the tube of length $L$ be deformed in such a way that the displacement of its center is $\Delta z \ll L$. Then the elongation of the tube, which plays the role of the

displacement $\Delta x$ produced by the longitudinal phonons, is

$$\Delta x = \sqrt{L^2 + (\Delta z)^2} - L \approx (\Delta z)^2/2L \ .$$

For a 500 nm long nanotube at a distance of 100 nm from the gate, the shift of the center $\Delta z$ is about 0.1 nm [25]. Calculating the coupling constant for $\omega_0 \sim 10^{12}$ Hz and $M \sim 10^{-22}$ kg, one obtains $g \sim 10^{-2}$, in contrast with the experimental observations.

A larger e-ph coupling is obtained if the electron density is inhomogeneous. The interaction energy of electrons with the polarization charge is characterized by the energy [28]

$$W = - \int dx dx' \rho(x) K(x - x') \frac{\partial P}{\partial x'}. \tag{7.1}$$

Here, $\rho(x)$ is the density of excess charge produced by one electron, $K(x-x')$ is an interaction kernel, which we approximate by $\delta(x - x')$ for the case when interactions are effectively screened by the gate, and $P(x) \approx e\rho_0 z(x)$ is the polarization vector. The quantity $\rho_0 \sim k_F$ is the total electron density and $z(x)$ is the displacement, which in the single-mode approximation becomes $z(x) = A_n \sin(\pi n x/L)$. Calculating the force $F = -\partial W/\partial A_n$, we obtain

$$F = \frac{e\rho_0 \pi n}{L} \int_0^L dx \ \rho(x) \cos \frac{\pi n x}{L}. \tag{7.2}$$

If the excess charge density is uniform, $\rho(x) = e/L$, $F = 0$ for all modes. Incorporation of interactions that are screened at distances longer than the distance to the gate, yields a force that scales as $L^{-2}$. In this case, the coupling parameter $g$ also scales as $L^{-2}$ and typical values are in the order of $10^{-2}$, as we have already discussed.

Assuming that the charge is localized in the center of the tube, $\rho(x) = e\delta(x - L/2)$, the force is zero for odd harmonics, but for even harmonics, $n = 2l$, it reads $F_l = (-1)^l e^2 \rho_0 2\pi l/L$ and $g = 4\pi^2 e^4 \rho_0^2 l^2/2L^2\hbar m\omega_0^3$. Since $m$ scales with $L$ and $\omega_0$ inversely with $L$, $g$ is length independent as observed in the experiment. Also, $g$ scales as $l^{-1}$ because $\omega_0$ scales with $l$ indicating that higher modes are coupled weaker to electrons. Numerical estimates show that $g \sim 1$. Localization of an electron in a point away from the middle produces coupling to both odd and even modes. Note that the electron does not have to be strongly localized: For any non-uniform density this mechanism will produce $g \sim 1$. A non-uniform density can be created by impurities located in the substrate, or induced by a redistribution of electrons in a suspended tube bent by a underlying gate electrode [29]. Note, that recent theoretical work has also considered e-ph coupling

in suspended nanotubes [30, 31]. They find $g$-values that are smaller than the experimental ones.

An interesting feature of the data is the appearance of negative differential conductance (NDC) in the current-voltage characteristics. NDC is very pronounced in Fig. 7.3a, but also present in Fig. 7.3b,c. Although several explanations for NDC have been put forward, its origin remains unclear. Koch and von Oppen [10] showed that for low relaxation and strong e-ph coupling, NDC features appear, although they do not follow regions with strong positive differential conductance (PDC) as in our data. McCarthy *et al.* [6] have shown that NDC features can be due to an e-ph coupling that is voltage dependent. Their calculations also reproduce the catastrophic current decrease of Fig. 7.3a for bias voltages higher than 3 mV. However, at the moment we do not know how such a voltage dependence would arise in suspended tubes. Finally, Nowack and Wegewijs [27] have considered a Franck-Condon model with a coupling to an electronic and its excited state. They show that the competition between the two states generates strong NDC effects. NDC and PDC lines may have the same gate voltage dependence preceded by a region of suppressed current. This scenario may especially be relevant for the data in Fig. 7.3a.

In summary, transport measurements on suspended SWNTs show signatures of phonon-assisted tunneling, mediated by longitudinal vibrational (stretching) modes. The current-voltage characteristics show multiple steps whose heights are in reasonable agreement with the Franck-Condon predictions if the e-ph coupling constant is of order unity. Suspended nanotube quantum dots form an interesting model system for future studies on the interaction between single electrons and quantized phonons in the intermediate to strong electron-phonon coupling limit.

# References

[1] M. L. Roukes, *Nanoelectromechanical systems face the future.* Phys. World **14**, 25 (2001).

[2] A.N. Cleland, *Foundations of Nanomechanics* (Springer, Berlin, 2002).

[3] L. Y. Gorelik *et al.*, *Shuttle mechanism for charge transfer in Coulomb blockade nanostructures.* Phys. Rev. Lett. **80**, 4526 (1998).

[4] A. Erbe, C. Weiss, W. Zwerger, and R. H. Blick, *Nanomechanical resonator shuttling single electrons at radio frequencies.* Phys. Rev. Lett. **87**, 096106 (2001).

[5] S. Braig and K. Flensberg, *Vibrational sidebands and dissipative tunneling in molecular transistors.* Phys. Rev. B **68**, 205324 (2003).

[6] K. D. McCarthy, N. Prokof'ev, and M. T. Tuominen, *Incoherent dynamics of vibrating single-molecule transistors.* Phys. Rev. B **67**, 245415 (2003).

[7] Y. M. Blanter, O. Usmani, and Y. V. Nazarov, *Single-electron tunneling with strong mechanical feedback.* Phys. Rev. Lett. **93**, 136802 (2004).; **94**, 049904(E) (2005).

[8] N. M. Chtchelkatchev, W. Belzig, and C. Bruder, *Charge transport through a single-electron transistor with a mechanically oscillating island.* Phys. Rev. B **70**, 193305 (2004).

[9] A. Mitra, I. Aleiner, and A. J. Millis, *Phonon effects in molecular transistors: Quantal and classical treatment.* Phys. Rev. B **69**, 245302 (2004).

[10] J. Koch and F. von Oppen, *Franck-Condon blockade and giant Fano factors in transport through single molecules.* Phys. Rev. Lett. **94**, 206804 (2005).

[11] H. Park *et al.*, *Nanomechanical oscillations in a single-C-60 transistor.* Nature (London) **407**, 57 (2000).

[12] A. N. Pasupathy *et al.*, *Vibration-assisted electron tunneling in C140 transistors.* Nano Lett. **5**, 203 (2005).

[13] E. M. Weig *et al.*, *Single-electron-phonon interaction in a suspended quantum dot phonon cavity.* Phys. Rev. Lett. **92**, 046804 (2004).

[14] B. Reulet *et al.*, *Acoustoelectric effects in carbon nanotubes.* Phys. Rev. Lett. **85**, 2829 (2000).

[15] V. Sazonova *et al.*, *A tunable carbon nanotube electromechanical oscillator.* Nature (London) **431**, 284 (2004).

[16] B. J. LeRoy, S. G. Lemay, J. Kong, and C. Dekker, *Electrical generation and absorption of phonons in carbon nanotubes.* Nature (London) **432**, 371 (2004).

[17] J. Nygård and D. H. Cobden, *Quantum dots in suspended single-wall carbon nanotubes.* Appl. Phys. Lett. **79**, 4216 (2001).

[18] H. Grabert and M.H. Devoret, Eds. *Single Charge Tunneling* (Plenum, New York, 1992).

[19] L. P. Kouwenhoven, D. G. Austing, and S. Tarucha, *Few-electron quantum dots.* Rep. Prog. Phys. **64**, 701 (2001).

[20] D. H. Cobden, M. Bockrath, P. L. McEuen, A. G. Rinzler, and R. E. Smalley, *Spin splitting and even-odd effects in carbon nanotubes.* Phys. Rev. Lett. **81**, 681 (1998).

[21] S. G. Lemay *et al.*, *Two-dimensional imaging of electronic wavefunctions in carbon nanotubes.* Nature (London) **412**, 617 (2001).

[22] M. S. Dresselhaus and P. C. Eklund, *Phonons in carbon nanotubes.* Adv. Phys. **49**, 705 (2000). H. Suzuura and T. Ando, *Phonons and electron-phonon scattering in carbon nanotubes.* Phys. Rev. B **65**, 235412 (2002). A. De Martino and R. Egger, *Acoustic phonon exchange, attractive interactions, and the Wentzel-Bardeen singularity in single-wall nanotubes.* Phys. Rev. B **67**, 235418 (2003).

[23] The twisting mode vibration of the nanotube has a comparable energy with the stretching mode. However, the twisting mode does not couple [22].

[24] L. D. Landau and E. M. Lifshitz, *Theory of Elasticity* (Pergamon, Oxford, 1986).

[25] S. Sapmaz, Y. M. Blanter, L. Gurevich, and H. S. J. van der Zant, *Carbon nanotubes as nanoelectromechanical systems.* Phys. Rev. B **67**, 235414 (2003).

[26] G.C. Schatz, and M.A. Ratner, *Quantum Mechanics in Chemistry* (Prentice-Hall, Englewood Cliffs, 1993).

[27] K.C. Nowack and M. Wegewijs, *Vibration-assisted tunneling through competing molecular states.* Cond-mat/0506552 (2005).

[28] A. A. Abrikosov, *Fundamentals of the Theory of Metals* (North-Holland, New York, 1988).

[29] D. Fedorets (unpublished).

[30] K. Flensberg, *Electron-vibron coupling in suspended nanotubes.* New J. Phys. **8**, 5 (2006).

[31] W. Izumida and M. Grifoni, *Phonon-assisted tunnelling in interacting suspended single-wall carbon nanotubes.* New J. Phys. **7**, 244 (2005).

# Chapter 8

# Excited state spectroscopy in carbon nanotube double quantum dots

S. Sapmaz, C. Meyer
P. Beliczynski, P. Jarillo-Herrero, and L. P. Kouwenhoven

We report on low temperature measurements in a fully tunable carbon nanotube double quantum dot. A new fabrication technique has been used for the top-gates in order to avoid covering the whole nanotube with an oxide layer as in previous experiments. The top-gates allow us to form single dots, control the coupling between them and we observe four-fold shell filling. We perform inelastic transport spectroscopy via the excited states in the double quantum dot, a necessary step towards the implementation of new microwave-based experiments.

## 8.1  Introduction

Electron spins in double quantum dots (DQDs) are one of the leading systems for fundamental studies of elementary solid-state qubits [1]. Recent progress has been based on DQDs in 2-dimensional electron gases in GaAs semiconductor heterostructures [2, 3]. However, the presence of non-zero nuclear spins limits the decoherence time in such structures [3, 4]. This drawback has stimulated the quest for novel materials that allow to fabricate DQDs with longer spin decoherence times. Among these, carbon nanotubes (CNTs) have properties that seem to make them an ideal material. Most of the natural carbon (98.93%) is $^{12}$C without nuclear spin. Thus, the nuclear field that leads to spin relaxation [5, 6] will be small compared to III/V semiconductors or even zero, if pure $^{12}$C is used in the growth of the carbon nanotubes. Also the spin-orbit interaction, which limits the spin relaxation time in semiconductor heterostructures [6, 7, 8], is expected to be very small in CNTs because of the low atomic number of carbon.

In order to realize CNT-DQDs (Figure 1), it is highly desirable to be able to create tunable tunnel barriers at arbitrary locations in a CNT, and some elementary devices have already been demonstrated [9, 10]. In order to make use of a CNT-DQD in quantum information processing, e.g. by determining spin and orbital relaxation times and by performing quantum operations, access to (spin) excited states is crucial. These excited states have not been observed previously in CNT-DQDs. Here we demonstrate an improved fabrication scheme compared to earlier approaches. Thin top-gates are evaporated such that only a small portion of the CNT is covered with oxide. We show electronic transport through the ground and excited energy states of CNT-DQDs.

The single walled carbon nanotubes (SWCNTs) are grown using chemical vapor deposition [11] (CVD) at lithographically predefined positions on a degenerately p-doped Si substrate with a 250 nm thick thermal oxide using a Fe/Mo based catalyst. The nanotubes are located by atomic force microscopy with respect to predefined markers, such that contacts and gates can be designed for each tube individually. First, we fabricate the contacts by means of electron beam lithography on a double layer PMMA-based resist, followed by metal (Pd) evaporation and lift-off in acetone. We use Pd as contact material because it introduces little or no barrier at the nanotube-metal contact [12, 13]. In a subsequent electron beam lithography step we 'write' the gate structures. For the top-gates we evaporate a 2 nm thin layer of Al and use the natural formation of thin insulating native oxide in an oxygen environment. We oxidized for ten minutes at 1 bar pure oxygen pressure to ensure a 2 nm thick oxide. These steps are then repeated once more, so that we end up with an oxide thickness of 4 nm.
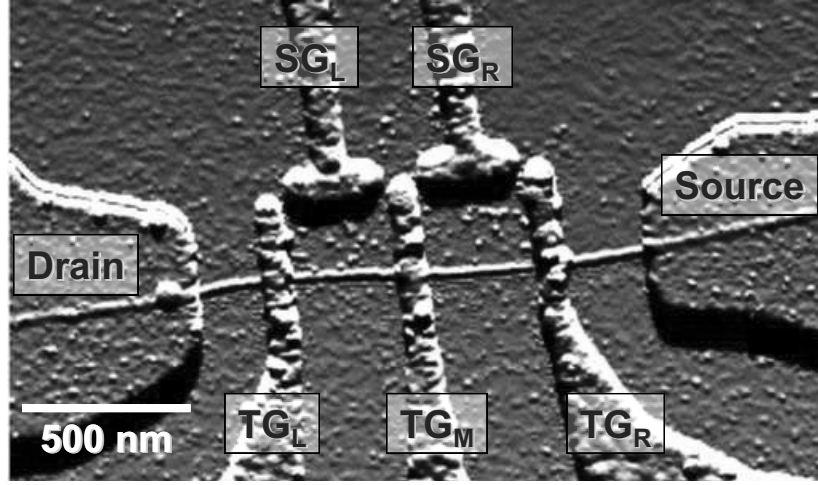
**Figure 8.1:** AFM picture of a CNT-DQD device similar to the one used for the actual measurements. The actual device (not shown here) has a tube diameter of about 3 nm and a total length of 1.9 $\mu$m between the Pd contacts, the left and right dots are both 550 nm, source-$TG_R$ segment is 560 nm long and the remaining $TG_L$-drain distance is 220 nm. Room-temperature measurements show a source-drain resistance of 30 k$\Omega$ and a small variation of the resistance with changing back-gate voltage. For the three top- and the two side-gates, a layer structure of $Al_2O_3$/Al (4 nm/35 nm) has been used. All structures in the image appear wider due to AFM tip convolution.

The evaporation is continued with a 35 nm thick Al layer and finalized by 15 nm of AuPd on top. The top-gates are about 30 nm wide, which is the lower limit for our fabrication process. The advantage of a narrow top-gate is that it controls the tunneling barrier on a local scale and only a small portion of the tube is covered with oxide. We think that this is an advantage for future devices, since an oxide always has charge traps and therefore provides a source of charge fluctuations that interfere with transport measurements.

Figure 1 shows an AFM image of a representative sample. The nanotube is divided into four segments by the three top-gates ($TG_L$, $TG_M$ and $TG_R$). The SWCNT segments between source-$TG_R$ and $TG_L$-drain are not forming a quantum dot due to the low source and drain contact resistances [12, 13]. By applying voltages to the top-gates we can tune the barriers and create quantum dots. Each quantum dot is addressed individually by the side-gates $SG_L$ and $SG_R$. Room-temperature measurements show a source-drain resistance of 30 k$\Omega$ and a small variation of the resistance with changing back-gate voltage indicating a small band gap tube. The conductance versus the left side-gate voltage for different values of the central top-gate is shown in the appendix.

## 8.2   Carbon nanotube quantum dots with tunable barriers

We can operate the sample in both the p-doped and n-doped regions. At low temperatures (300 mK) we observe the highest conductance when applying negative voltages to the top-gates and operate the device in the hole-transport regime. Figure 2 shows a differential conductance plot as a function of source-drain and back-gate voltage. The highly-doped silicon substrate is used as the back-gate with the intention to change the electrochemical potential of the nanotube uniformly. Note that the average conductance is between 2 and 3 times $e^2/h$ (the measured maximum is 3.14 $e^2/h$). The pattern in Figure 2 is due to quantum interference in the nanotube which acts as an electron waveguide in analogy with the optical Fabry-Perot cavity, as previously studied in nanotubes [13, 14]. The bias voltage at the crossing point $V_C$ between adjacent left- and right-sloped dark lines (see white arrows) is found to depend on the length of the waveguide $L$, as $V_C = hv_F/2eL$ (Fermi velocity $v_F = 8.1 \cdot 10^5$ m/s [15]). The pattern in figure 2 is less regular than reported in previous studies [14]. A possible reason for this is the presence of narrow top-gates on the tube which can act as weak scatterers. We mainly find a value of $V_C = V_{SD} \sim 0.5 - 0.6$ meV, corresponding to a length of about 3 $\mu$m. This suggests that the electron scattering occurs primarily at the nanotube-Pd interfaces since the extracted length is much larger than the top-gate spacing. The overestimation of the length could be due to band bending. Close to the band gap, the dispersion $dE/dk$ is smaller than in the linear dispersion relation of a metal tube and therefore the velocity decreases as well, and thus results in a smaller value for the crossing point $V_C$.

By applying positive voltages to the top-gates we form barriers in this p-type region. Figure 3a shows the typical characteristics of a clean nanotube single quantum dot. We form the dot by setting the voltages on $TG_L$, $TG_M$ to 4 V, and $TG_R$ to -4 V to keep this part open. The four-fold shell filling pattern in the Coulomb blockade diamonds expected for carbon nanotubes [16, 17, 18, 19] is clearly visible (see inset for addition energies) together with the excitation lines (lines parallel to the diamond slope). Only 5 parameters are needed to characterize the nanotube low-energy electronic shell structure [20]. These are the charging energy $E_C$, the orbital level spacing $\Delta$, the sub-band mismatch $\delta$, the exchange energy $J$, and the excess Coulomb energy $dU$. The fact that the three smaller diamonds in Figure 3a are about the same size (see also inset) and quite smaller than the large diamond suggests that the values for $\delta$, $J$, and $dU$ are small compared to $\Delta$. We extract for $E_C \sim 4$ meV, and for $\Delta \sim 2$ meV. This

is also consistent with the observed excitation lines. A clear excitation line is present at around 2 meV and additionally we see inelastic co-tunneling lines [21] at energies less than 200 $\mu$eV, which are most likely due to the small values of the parameters $\delta$, $J$, $dU$. We obtain the length of the nanotube quantum dot $L = hv_F/2 = 740$ nm from the value of the level spacing ($\sim 2$ meV). This is in reasonable agreement with the fabricated nanotube quantum dot size of 550 nm. The overestimation of its length may again be due to the smaller velocity close to the gap (see discussion above).

The characterization of the right dot is shown in Figure 3b. No clear shell-filling pattern is observed in this case. But closed diamonds and constant slopes of the diamond edges indicate that we measure a single dot. Excited states are also clearly visible. Assuming that $\delta$, $J$, and $dU$ are as small as in the left dot, we obtain a larger charging energy in the order of $E_C \sim 10$ meV [22]. From the excited states, we find for the level spacing $\sim 3$ meV. This corresponds to a quantum dot length of 570 nm, again in good agreement with the designed size. We also observe negative differential conductance (NDC) which is seen as black lines parallel to the diamond slope. NDC has been observed in many types of quantum dots and can have different origins [23, 24, 25]. A possible explanation in our structure could be that a poorly coupled excited state becomes occupied, which then blocks the current through the ground state. This leads to a smaller current at larger bias and therefore to NDC.
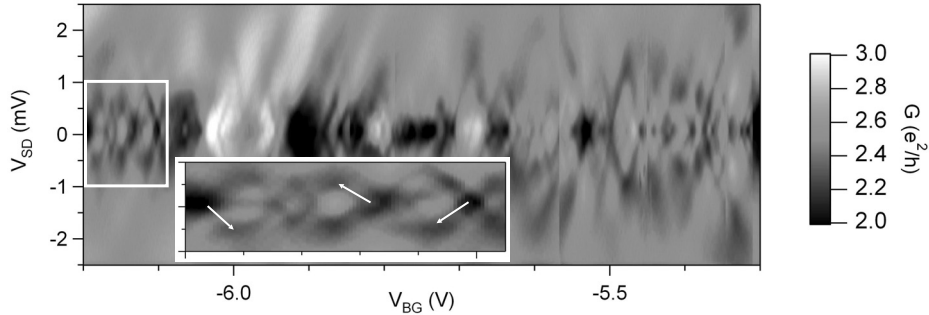


**Figure 8.2:** Differential conductance measured with a lock-in amplifier. All top-gates are set to -4 V. This opens the barriers completely, because the measurement is done in the p-type region of the small bandgap SWNT. Fabry-Perot interference is observed over a wide gate range. The inset shows a zoom-in of the region in the white rectangle. One can clearly identify destructive interference at $\sim$0.6 meV (see arrows). The high conductance (up to $G = 3.1e^2/h$) shows that the Pd contacts have a transmission close to $T = 1$.

## 8.3    Carbon nanotube double quantum dot

Figure 4 shows the characteristic "honeycomb" structure of the current through a double quantum dot [26] in the strongly coupled regime. Here, the two dots are not completely separated but interact via tunnel coupling, thus forming the analogue of a molecule with covalent bonding. The co-tunneling lines of the hexagonal pattern are visible and exhibit the four-fold shell filling for the left dot, just as the diamonds did in the previous single dot measurement: a large hexagon is followed by three small ones in the vertical direction of the left side-gate. This pattern repeats for every electron number in the right dot with the same top-gate settings.

In Figure 5 we show the double dot in the weakly coupled regime, i.e. the inter-dot tunnel resistance is high and the capacitive coupling between the dots dominates the transport behavior. The measurements are done in a different gate-region than the previous measurements. A small voltage is applied at the center top-gate (200 mV) and the left and right top-gates are set to zero Volts in order to reach the weakly coupled regime. The values for the side-gates are adjusted because the top-gates do not only change the tunnel barriers but shift the chemical potential of the dot as well. The triple points of the expected hexagonal pattern are very well visible and, due to the large bias, develop into
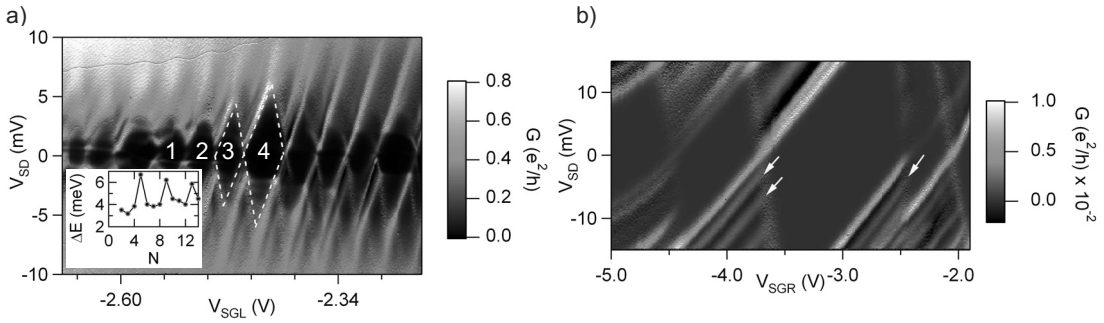


**Figure 8.3:** Stability diagrams of the left and right quantum dot: **(a)** The left dot is formed with top-gate values $TG_L = TG_M = 4$ V, $TG_R = -4$ V. Four fold shell filling and excited states are clearly visible in the numeric $dI/dV$. In the inset, the addition energy of the $N$-th electron is plotted for three shells. The yellow dotted lines are a guide to the eye indicating the shape of one small and one large diamond and the electron number in a particular shell is indicated. **(b)** The right dot is formed with top-gate values $TG_L = -4$ V, $TG_M = 2$ V, and $TG_R = 4$ V. No obvious shell-filling is observed in this case. However, excited states are clearly visible. Those that belong to the level splitting are indicated by arrows. Regions of negative differential conductance are also observed (black lines).
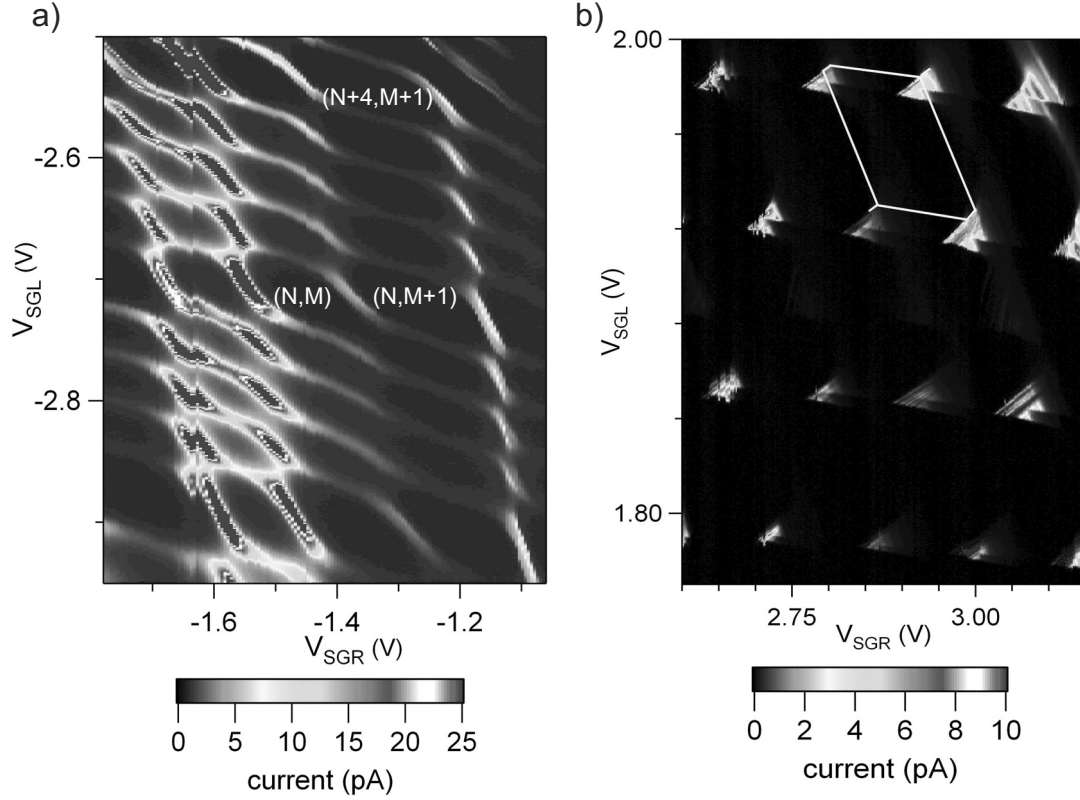
**Figure 8.4: (a)** A double dot in the strongly coupled regime is formed with $\text{TG}_\text{L} = \text{TG}_\text{M} = 4$ V, and $\text{TG}_\text{R} = 1.5$ V ($V_{SD} = 1$ mV). The absolute values for $(N, M)$ of the (left, right) quantum dot are unknown. However, the four-fold shell filling of the left dot is clearly visible in this honeycomb pattern, from which we can identify filled shells when $(N, N+4$, etc.$)$. **(b)** Characteristic "honeycomb" structure of the current for the double dot in the weakly coupled regime ($\text{TG}_\text{L} = \text{TG}_\text{R} = 0$ V, $\text{TG}_\text{M} = 200$ mV). The triple points with excited states are visible at the applied high bias of $V_{SD} = 5$ mV. From the size of the triangles and the hexagons, all capacitances that characterize the double dot can be calculated.

overlapping triangles [26]. Excited states are observed in every triple point. In the appendix we show measurements on a different nanotube double dot in figure 3 to demonstrate reproducibility.

All capacitances [26] that characterize the double quantum dot are calculated from the size of the hexagons and triple points in Figure 5: The capacitive coupling between the dots is $C_\text{TGM} = 1$ aF, the total capacitances of the left and right dot are $C_\text{L} = 7.2$ aF and $C_\text{R} = 12.5$ aF, respectively, and the relative capacitances between each side-gate and its neighboring dot are $C_\text{SGL} = 3$ aF and $C_\text{SGR} = 1.5$ aF.

We obtain tunnel barriers even for zero or small top-gate voltages for certain gate regions. This indicates that the fabrication of the local top-gates alone induces a small barrier. A small co-tunneling current is visible in the upper right area of Figure 5 which shows up as lines linking the triple points. The fact that there is no co-tunneling current in the rest of the figure shows that the tunnel barriers change while changing the side-gate voltages and that there are cross capacitances between the gates.

A high resolution measurement of a pair of triple points (electron- and hole-cycle) is shown in Figure 6 for $V_{SD} = 4$ mV. At the baseline of the triangle the ground states of the two dots are aligned and shifted together from the Fermi-level of the drain (point a in Figure 6) to the Fermi-level of the source (point b). At the center of the baseline they lie exactly in the middle between source and drain. On a line from this point to the tip of the triangle (point c), the states of the right dot are shifted downwards to the Fermi-level of the source, while the states of the left dot shift upwards to the drain (a positive bias is applied at the source contact, while the drain contact is put to ground). Along this line, we see sharp excitations at 0.33, 1.24, 1.55, and 1.8 mV (see inset of Figure 6). These lines belong to different excited states of the left dot which are probed by states of the right dot. An area of non-resonant current spreads between 2 and 2.8 mV. In figure 2 of the appendix we show data for an adjacent pair of triple points. The excited states for both pairs are consistent.

In the following we give a possible scenario for the resonant transport. Afterwards, we discuss the non-resonant current. On the right side of the triangles of both triple points there appears to be a region of strongly suppressed current. This feature could be explained by bad coupling of the ground state of the right dot to the source. As the levels of the dots move upwards with lowering the side-gate voltages, at point (*) the first hole-excited state [27] of the right dot enters the bias window at $\sim 650 \mu$eV. The coupling of this level to the source contact is stronger, thus enhancing the current.

The lines parallel to the baseline of the triangle belong to resonant transport through hole-excited states of the left dot. Only the first of these excited states at $\sim 330 \mu$eV is probed by the ground state of the right dot (point e). At the other lines, the excited state of the right dot at $\sim 650 \mu$eV is aligned with the excited states of the left dot (see point f as an example). This could also explain the larger current through these lines, as the excited states are probably better coupled to the contacts. Taking this into account, the energy splitting of the second excited state (**) of the left dot to its ground state is 1.9 meV. This fits well with the value for the level splitting we obtained from the single dot measurement. The next two lines split by 310 and 560 $\mu$eV with respect to the
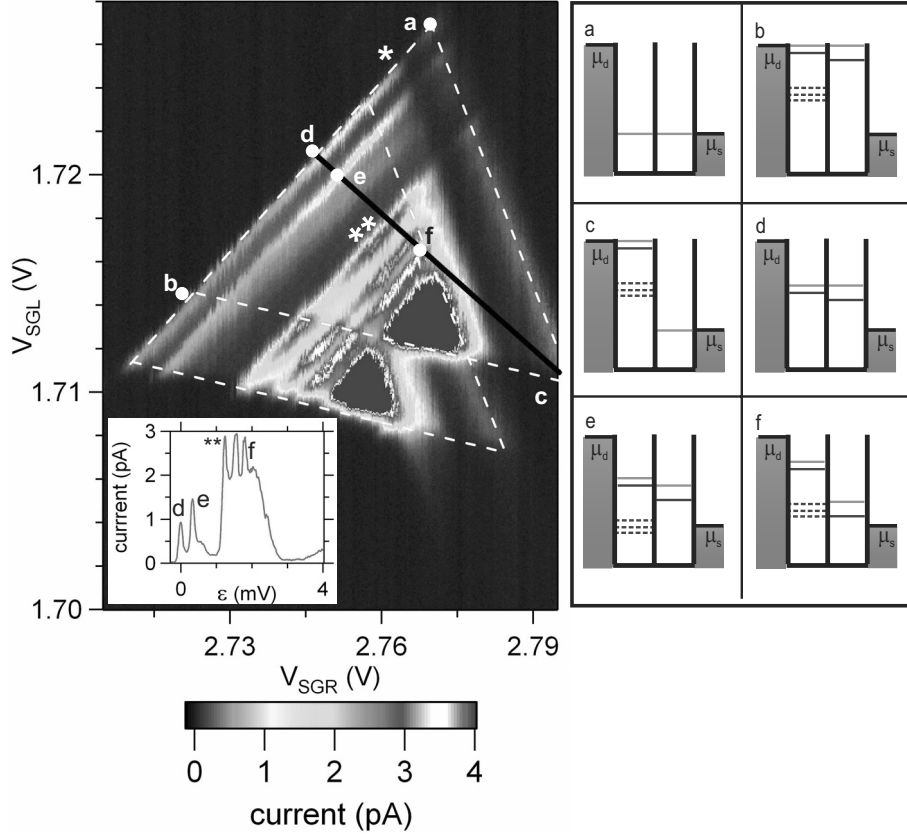
**Figure 8.5:** Current versus side gate voltages for a typical example for a triple point at high bias ($V_{SD} = 4$ mV) in the p-doped region (hole transport). The ground state tunneling is weaker then tunneling through excited states. Lines parallel to the base (point a to point b) of a triangle belong to tunneling through excited states of the left dot, while the right dot excited states show up parallel to the upper-right side of the triangle (the first one enters the bias window at point (*)). The inset shows a line cut from the center of the base of the upper triangle to the triangle tip (black line from point d to point c), i.e., current as a function of the detuning between levels. The level schemes of the double dot corresponding to the points a to f depicted in the triangle are shown on the right side of the figure. Grey lines represent the ground states, black lines hole-excited states (the measurement is done in the p-doped region). The dashed lines belong to the next excited states corresponding to (**).

level (**) at $\Delta$. Like the first one at $\sim 330 \mu$eV (point e) they are comparable in size with the low energy splitting found in the single dot measurement of the left QD.

Non-resonant transport can occur if an electron looses energy due to spontaneous emission of an acoustic phonon [28]. However, we do not observe the

expected decay of the current for one-dimensional acoustic phonons with detuning of the DQD states. The non-resonant current between 2 mV and 2.8 mV seems to have its origin rather in level broadening of excited states at higher energy.

Electron-phonon coupling in a molecule such as a CNT can show up as sharp resonance lines. These would be equidistant with an energy difference that depends on the diameter and length of the tube [29]. For a length of 2 $\mu$m, an energy difference of $E_{phonon} \sim 55\mu$eV is expected. If the size of the single QDs of  500 nm would determine the energy of the phonons, one would expect $E_{phonon} \sim 440\mu$eV. None of these energy scales show up in the lines inside the triangle. Thus we conclude that the lines inside the triangle are due to resonant transport through electronic excitations.

In this letter we have demonstrated the full tunability of a carbon nanotube double quantum dot. We avoid covering the whole tube with an oxide layer by fabricating narrow $AlO_x$/Al top gates, and by that disturbing the structure of the carbon nanotube as little as possible. In this way, we are able to show Fabry-Perot interference between the source/drain contacts in a SWCNT structure with top-gates. The typical four-fold shell filling of a small band gap tube and excited states are visible in the stability diagram of the left dot. This shows that we are able to fabricate tunable barriers for carbon nanotube quantum dots, which is essential for spin relaxation time measurements [30, 31]. The shell filling of the single dot is also visible in the hexagon pattern of the double quantum dot. The excited states of both dots show up as resonant tunneling lines in the triple points. This paves the way for new microwave-based quantum information processing experiments with carbon nanotubes.

# References

[1] D. Loss and D. P. DiVincenzo, *Quantum computation with quantum dots.* Phys. Rev. A **57**, 120 (1998).

[2] J. M. Elzerman *et al.*, *Single-shot read-out of an individual electron spin in a quantum dot.* Nature (London) **430**, 431 (2004).

[3] J. R. Petta *et al.*, *Coherent manipulation of coupled electron spins in semiconductor quantum dots.* Science **309**, 2180 (2005).

[4] F. H. L. Koppens *et al.*, *Control and detection of singlet-triplet mixing in a random nuclear field.* Science **309**, 1346 (2005).

[5] S. I. Erlingsson and Y. V. Nazarov, *Hyperfine-mediated transitions between a Zeeman split doublet in GaAs quantum dots: The role of the internal field.* Phys. Rev. B **66** (2002).

[6] A. V. Khaetskii and Y. V. Nazarov, *Spin relaxation in semiconductor quantum dots.* Phys. Rev. B **61**, 12639 (2000).

[7] L. M. Woods, T. L. Reinecke, and Y. Lyanda-Geller, *Spin relaxation in quantum dots.* Phys. Rev. B **66**, 161318 (2002).

[8] V. N. Golovach, A. Khaetskii, and D. Loss, *Phonon-induced decay of the electron spin in quantum dots.* Phys. Rev. Lett. **93**, 016601 (2004).

[9] N. Mason, M. J. Biercuk, and C. M. Marcus, *Local gate control of a carbon nanotube double quantum dot.* Science **303**, 655 (2004).

[10] M. J. Biercuk, S. Garaj, N. Mason, J. M. Chow, and C. M. Marcus, *Gate-defined quantum dots on carbon nanotubes.* Nano Lett. **5**, 1267 (2005).

[11] J. Kong, H. T. Soh, A. M. Cassell, C. F. Quate, and H. J. Dai, *Synthesis of individual single-walled carbon nanotubes on patterned silicon wafers.* Nature (London) **395**, 878 (1998).

[12] A. Javey, J. Guo, Q. Wang, M. Lundstrom, and H. Dai, *Ballistic carbon nanotube field-effect transistors.* Nature (London) **424**, 654 (2003).

[13] D. Mann, A. Javey, J. Kong, Q. Wang, and H. J. Dai, *Ballistic transport in metallic nanotubes with reliable Pd ohmic contacts.* Nano Lett. **3**, 1541 (2003).

[14] W. Liang *et al.*, *Fabry-Perot interference in a nanotube electron waveguide.* Nature (London) **411**, 665 (2001).

[15] S. G. Lemay *et al.*, *Two-dimensional imaging of electronic wavefunctions in carbon nanotubes.* Nature (London) **412**, 617 (2001).

[16] W. Liang, M. Bockrath, and H. Park, *Shell filling and exchange coupling in metallic single-walled carbon nanotubes.* Phys. Rev. Lett. **88**, 126801 (2002).

[17] S. Sapmaz *et al.*, *Electronic excitation spectrum of metallic carbon nanotubes.* Phys. Rev. B **71**, 153402 (2005).

[18] S. Moriyama, T. Fuse, M. Suzuki, Y. Aoyagi, and K. Ishibashi, *Four-electron shell structures and an interacting two-electron system in carbon-nanotube quantum dots.* Phys. Rev. Lett. **94** (2005).

[19] B. Babic and C. Schonenberger, *Observation of Fano resonances in single-wall carbon nanotubes.* Phys. Rev. B **70**, 195408 (2004).

[20] Y. Oreg, K. Byczuk, and B. I. Halperin, *Spin configurations of a carbon nanotube in a nonuniform external potential.* Phys. Rev. Lett. **85**, 365 (2000).

[21] S. De Franceschi *et al.*, *Electron cotunneling in a semiconductor quantum dot.* Phys. Rev. Lett. **86**, 878 (2001).

[22] The asymmetric placement of the top-gates on the nanotube with respect to the source and drain electrodes (see fig. 1 caption) may explain the different charging energy for the left and right dot.

[23] A. T. Johnson *et al.*, *Zero-Dimensional States and Single Electron Charging in Quantum Dots.* Phys. Rev. Lett. **69**, 1592 (1992).

[24] J. Weis, R. J. Haug, K. Vonklitzing, and K. Ploog, *Competing Channels in Single-Electron Tunneling through a Quantum-Dot.* Phys. Rev. Lett. **71**, 4019 (1993).

[25] H. Nakashima and K. Uozumi, *Negative differential resistance on electron transport through ultrasmall particles.* Jpn. J. Appl. Phys. **34**, L1659 (1995).

[26] W. G. van der Wiel *et al.*, *Electron transport through double quantum dots.* Rev. Mod. Phys. **75**, 1 (2003).

[27] We know that the measurements are taken in the p-type region of the CNT, because the barriers become more open with smaller voltage applied (not shown here).

[28] T. Fujisawa *et al.*, *Spontaneous emission spectrum in double quantum dot devices.* Science **282**, 932 (1998).

[29] S. Sapmaz, P. Jarillo-Herrero, Y. M. Blanter, C. Dekker, and H. S. J. van der Zant, *Tunneling in suspended carbon nanotubes assisted by longitudinal phonons.* Phys. Rev. Lett. **96**, 026801 (2006).

[30] T. Fujisawa, Y. Tokura, and Y. Hirayama, *Transient current spectroscopy of a quantum dot in the Coulomb blockade regime.* Phys. Rev. B **63**, 081304 (2001).

[31] R. Hanson *et al.*, *Single-shot readout of electron spin states in a quantum dot using spin-dependent tunnel rates.* Phys. Rev. Lett. **94**, 196802 (2005).
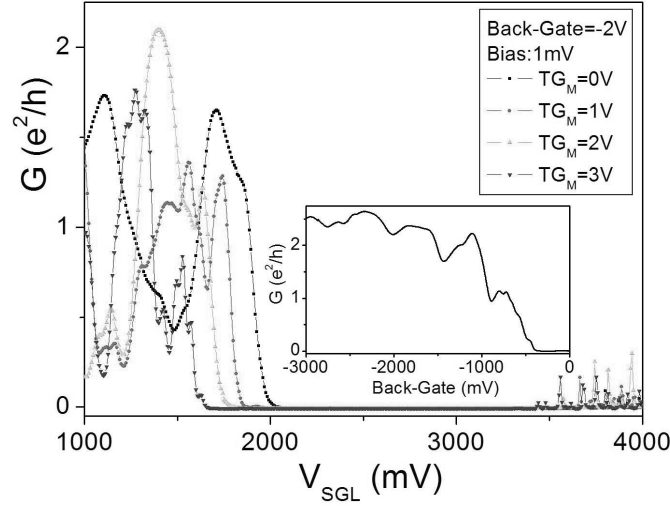
## 8.4   Appendix



**Figure 8.6:** Conductance as a function of the left side-gate voltage ($SG_L$) at 4K is shown for different central top-gate values and with a fixed voltage of -2V on the back-gate showing $p$- and $n$-type behaviour. In the inset we show the conductance as a function of the back-gate voltage, while all other gates are grounded, in the p-region.

We provide additional measurements in the supplementary information. First we show in Fig. 8.6 a measurement of the conductance as a function of the left side-gate for different central top-gate values. The peak position moves to lower gate voltage values, as expected, and also the first peak height decreases, which indicates that we influence the tunnel barrier. In figure 8.7, we focus on a pair of triple points adjacent to the pair of Fig. 8.5. The total charge in this case $N$-1 holes in the left and $M$ holes in right dot (the situation in the paper is $N$ and $M$ number of holes in the dots). In the subfigures different alignment of levels are shown for the situations indicated in the main figure. We find that the excited state of the right dot is practically the same as obtained from Fig. 8.5. This is as expected. For the excited states of the left we find different values for the different cases. Since the number of charges in the left dot is different for the two situations (Fig. 8.5 and Fig. 8.7) it is expected to have a different excited state spectrum for both cases. Finally, in Fig.8.8 we show measurements on a different nanotube double dot sample to demonstrate reproducibility. In the different figures we show that we can operate the sample in different double dot regimes: weak- and strong-tunnel coupled regimes. Furthermore we present a zoom-in of a pair of triple points where the excited states are resolved.
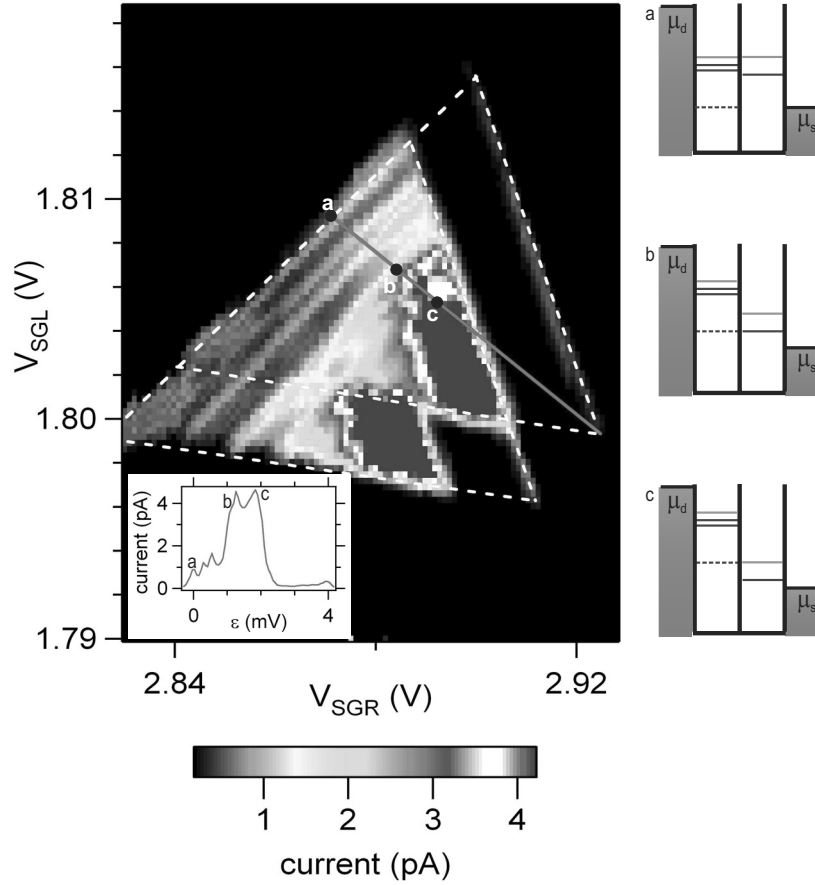
**Figure 8.7:** Triple point with (*n*-1) holes in left dot and same number of holes in right dot compared to the triple point in Fig. 8.5. A bias voltage of 4 mV is applied and the top-gates are grounded for this measurement. The inset shows the current as a function of the detuning between ground state levels (solid line in triple point). Level schemes corresponding to three of the current peaks are shown on the right. We obtain a level splitting of $700 \pm 60$ $\mu$eV for the right dot from these data. There is one more excited state visible in the first orbital of the left dot. The first state is found at $320$ $\mu$eV, the second at $\sim 580$ $\mu$eV. The next peak corresponds to situation b: The next orbital excited state of the left dot is aligned with the excited state of the right dot. This leads again to an orbital splitting of $\sim 1.9$ meV. The low energy excited states for the next orbital are not resolved due to the higher non-resonant current. The last peak corresponds more likely to situation c, as the splitting to b is $\sim 650$ $\mu$eV.
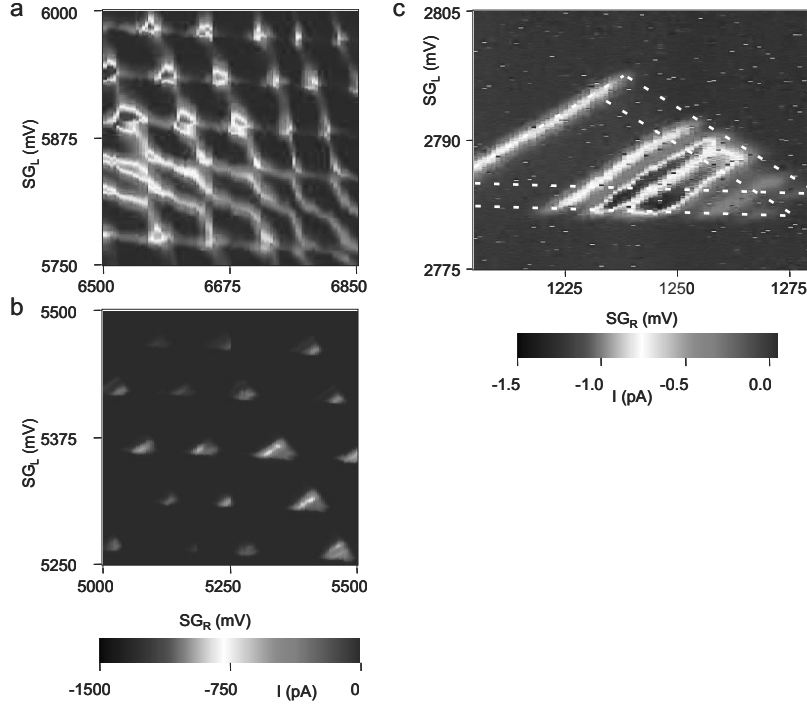
**Figure 8.8:** We show measurements on a different nanotube double quantum dot with a length of 500 nm for both the left and right dot. We apply a source drain bias voltage of -1 mV for (**a**), (**b**) and a bias of -3 mV for (**c**). The central top-gate is set to -1.5 V. The current is plotted in color scale. In (**a**) the double dot is in the strong tunnel-coupling regime and a clear honeycomb pattern is visible. In (**b**) the triple points are clearly visible and the double dot is in the weak tunnel-coupling regime. In contrast to conventional GaAs quantum dots we do not have to retune the barriers to observe the double dot behaviour over a large side-gate voltage range. In (**c**) we show a zoom-in of a pair of triple points where excited states are clearly resolved. Note that the current only flows when discrete levels are aligned.

# Summary

## Carbon nanotube quantum dots

Low temperature electron transport measurements on individual single wall carbon nanotubes are described in this thesis. Carbon nanotubes are small hollow cylinders made entirely out of carbon atoms. At low temperatures (below $\sim 10$ K) finite length nanotubes form quantum dots. Because of its small size a quantum dot has a discrete set of energy levels where electrons can be placed. Therefore, it resembles an atom in many aspects. The research presented here focuses on understanding the behavior of nanotube quantum dots.

Until recently, we have fabricated nanotube quantum dots by just evaporating metal contacts on top of the nanotube segments. This way tunnelbarriers develop naturally at the nanotube-metal interfaces.

The addition of a single electron requires a considerable energy due to the small size of the nanotube. At low temperatures this energy is absent, and the nanotube quantum dot is then in the 'Coulomb blockade' regime. Applying a bias voltage between the electrodes or changing the electrostatic potential of the quantum dot by a voltage on a nearby gate can lift the Coulomb blockade and hence allow single electron tunneling processes through the barriers. By measuring the current going through the nanotube we study the electron transport behavior of the nanotube quantum dot.

We are primarily focussed on nanotube quantum dots in the 'closed' quantum dot regime. In this regime the tunnelbarriers are very opaque and the electrons are strongly confined in the quantum dot. Also, the energy width are sharply defined allowing for accurate spectroscopy measurements.

In chapter 4 we report the first observation of the discrete energy spectrum of semiconducting nanotubes. Furthermore, the semiconducting nanotube quantum dot can be completely depleted from free charge carriers. Electrons or holes could be added one by one. This permits us to compare the excitation spectra for electrons and holes. We find that they are symmetric, as expected from the symmetry in the bandstructure.

The energy spectra of metallic nanotubes in the closed quantum dot regime

are explained in chapter 5. Using a model, which extends the 'constant inter-action model' with exchange interaction effects and the orbital degeneracy of the nanotube bandstructure, the full measured energy spectrum of the nanotube quantum dot is identified and accounted for.

Of recent interest in the field of nanoscience is the interplay between electrical and mechanical properties. In a theoretical study we predict that the tunneling of a single electron onto a suspended nanotube drastically modifies the quantized vibrational eigenmodes due to the electrostatic forces which bend and tension the nanotube.

Measurements performed on quantum dots in freely suspended nanotube at low temperatures shows a small, harmonic excitation spectrum, which can not be identified with purely electronic excitations. We propose phonon assisted tunnel-ing to be responsible for these excitations. Using a Franck-Condon based model, in which the phonon assisted tunneling processes are modeled as a coupling of electronic levels to underdamped quantum harmonic oscillators, we find good agreement with the measurements.

Lately, the emphasis of carbon nanotube quantum dot research is shifting towards defining nanotube quantum dots with tunable barriers. In the last chap-ter we present a fabrication procedure for defining nanotube quantum dots with controllable barriers. This way it was possible to extend the system to form a double quantum dot. This last step was highly motivated by the possibility that double quantum dot systems could act as a solid state quantum bit. We perform transport measurements on the nanotube double quantum dot and observe the excited states of the systems. This opens up new possibilities for fundamental and applied studies on nanotube quantum dots.

Sami Sapmaz
May 2006

# Samenvatting

## Koolstof nanobuis kwantum dots

Lage temperatuur elektron transport metingen aan enkel wandige koolstof nanobuisjes zijn beschreven in dit proefschrift. Deze buisjes zijn kleine holle cilinders die uitsluitend uit koolstof atomen bestaan. Eindig lange nanobuizen vormen bij lage temperaturen (onder $\sim 10K$) vormen kwantum dots. Vanwege zijn kleine afmetingen heeft een kwantum dot een discrete set van energie niveaus waarin elektronen geplaatst kunnen worden. Derhalve vertoont het in vele aspecten een gelijkenis met atomen. Het onderzoek dat hierin beschreven is richt zich op het begrijpen van kwantum dots in koolstof nanobuis.

Tot voor kort, hebben we de koolstof nanobuis kwantum dots gefabriceerd door metalen contacten bovenop nanobuis segementen te dampen. Op deze wijze vormen tunnelbarrières zich op een natuurlijke manier aan het nanobuis-metaal raakvlak.

De additie van een enkel elektron vergt een aanzienlijke energie vanwege de kleine afmetingen van de nanobuis. Bij lage temperaturen is deze energie afwezig en de nanobuis kwantum dot is dan in het 'Coulomb blokkade' regime. Door een 'bias' voltage tussen de elektroden of door het veranderen van de elektrostatische potentiaal van de kwantum dot kunnen we de Coulomb blokkade opheffen en derhalve enkel elektron tunnel processen door de barrières toestaan. Door het meten van de stroom door de nanobuis bestuderen wij het elektron transport gedrag van de nanobuis kwantum dot.

Wij zijn hoofdzakelijk geïnteresseerd in nanobuis kwantum dots in het 'gesloten' kwantum dot regime. In dit regime zijn de tunnelbarrières erg hoog en de elekronen zijn goed opgesloten in de kwantum dot. Ook is de breedte van energie niveaus scherp gedefinieerd en is het mogelijk om nauwkeurig spectroscopische metingen te verrichten.

In hoofdstuk 4 rapporteren we de eerste observatie van diskrete energie spectra van halfgeleidende nanobuizen. Bovendien kunnen de vrije ladingsdragers uit de kwantum dot in de halfgeleidende nanobuis worden geduwd. Elektronen en gaten kunnen één voor één bijgeplaatst worden. Dit geeft ons de mogelijkheid om de

excitatiespectra voor elektronen en gaten te vergelijken. We constateren dat ze symmetrisch zijn, zoals verwacht van de symmetrie in de bandstructuur.

De energiespectra van metallische nanobuizen in het gesloten kwantum dot regime worden uitgelegd in hoofdstuk 5. Met een model, dat het 'constante interactie model' uitbreidt met wisselwerkingseffecten en de orbitale ontaarding van de nanobuis bandstructuur, kon het gehele gemeten energiespectrum van de nanobuis kwantum dot geïdentificeerd en verklaard worden.

Van actuele interesse in het vakgebied van nanoscience is het samenspel tussen elektrische en mechanische eigenschappen. In een theoretische studie voorspellen we dat het tunnelen van een enkel elektron op een vrij opgehangen nanobuis de gekwantiseerde eigentoestanden drastisch verandert via de elektrostatische krachten die de nanobuis buigen en spannen.

Metingen verricht aan kwantum dots in vrij opgehangen nanobuizen bij lage temperaturen tonen een laag, harmonisch excitatiespectrum dat niet met electronische excitaties worden geïdentificeerd. We stellen phonon geassisteerd tunnelen voor als verantwoordelijk voor deze excitaties. Gebruik makend van een Franck-Condon gebaseerd model, waarin de phonon geassisteerde tunnel processen gemodelleerd zijn als een koppeling van elektronische niveaus met ondergedempte kwantum harmonische oscillatoren, vinden we goed overeenstemming met de metingen.

Recentelijk verschuift de nadruk van koolstof nanobuis kwantum dot onderzoek naar het definiëren van koolstof nanobuis kwantum dots met afstembare tunnelbarriéres. In het laatste hoofstuk presenteren we een fabricage procedure for het definiëren van nanobuis kwantum dots met controleerbare barriéres. Zo was het mogelijk om het systeem uit te breiden tot een dubbele kwantum dot. Deze stap was gemotiveerd door de mogelijkheid dat dubbele kwantum dots systemen als een vaste stof kwantum bit kunnen worden gebruikt. We voeren transport metingen uit aan deze dubbele dots en nemen geëxciteerde toestanden waar. Dit opent nieuwe mogelijkheden voor fundamenteel en toegepast onderzoek aan kwantum dots.

<div align="right">

Sami Sapmaz

mei 2006

</div>

# Curriculum Vitae

Sami Sapmaz

26-08-1979    Born in Dordrecht, the Netherlands.

1991-1997     V.W.O. at the 'Scholengemeenschap Dordtwyck' in Dordrecht.

1997-2002     M.Sc. Applied Physics,
Delft University of Technology.
Graduate research in the Quantum Transport group of
prof.dr.ir. J.E. Mooij.
Subject: Single electron induced mechanical motion of nanotubes

2002-2006     Ph.D research at Delft University of Technology
under supervision of prof.dr.ir. L.P. Kouwenhoven
Subject: Carbon nanotube quantum dots

# List of publications

1. *Quantum dots in carbon nanotubes*
   S. Sapmaz, P. Jarillo-Herrero, L.P. Kouwenhoven, and H. S. J. van der Zant.
   To appear in Semiconductor science and technology (2006), special issue on Charge transport in carbon nanotubes.

2. *Excited State Spectroscopy in Carbon Nanotube Double Quantum Dots*
   S. Sapmaz, C. Meyer, P. Beliczynski, P. Jarillo-Herrero, and L.P. Kouwenhoven.
   To appear in Nano Letters (2006).
   See also http://pubs3.acs.org/acs/journals/doilookup?in_doi=10.1021/nl052498e

3. *Tunneling in suspended carbon nanotubes assisted by longitudinal phonons*
   S. Sapmaz, P. Jarillo-Herrero, Ya. M. Blanter, C. Dekker, and H.S.J. van der Zant.
   Physical Review Letters **96** 026801 (2006).

4. *Coupling between electronic transport and longitudinal phonons in suspended nanotubes*
   S. Sapmaz, P. Jarillo-Herrero, Ya. M. Blanter, and H. S. J. van der Zant.
   New Journal of Physics **7** 243 (2005), special issue on Nano-electromechanical systems.

5. *Electronic excitation spectrum of metallic carbon nanotubes*
   S. Sapmaz, P. Jarillo-Herrero, J. Kong, C. Dekker, L. P. Kouwenhoven, and H. S. J. van der Zant.
   Physical Review B **71**, 153402 (2005).

6. *A few electron-hole semiconducting carbon nanotube quantum dot*
   P. Jarillo-Herrero, S. Sapmaz, C. Dekker, L. P. Kouwenhoven, and H. S. J. van der Zant.
   Proceedings of the International Winterschool on Electronic Properties of Novel Materials 583 (2004).

7. *Electron-hole symmetry in a semiconducting carbon nanotube quantum dot*
   P. Jarillo-Herrero, S. Sapmaz, C. Dekker, L. P. Kouwenhoven, and H. S. J. van der Zant.
   Nature **429**, 389 (2004).

8. *Carbon nanotubes as nanoelectromechanical systems*
   S. Sapmaz, Ya. M. Blanter, L. Gurevich, and H. S. J. van der Zant.
   Physical Review B **67** 235414 (2003).